IDEALIZED MODELING OF SEASONAL VARIATION

IN THE

ALASKA COASTAL CURRENT

By

William James Williams

RECOMMENDED:

Advisory Committee Chair

Head, Program in Marine Sciences and Limnology

APPROVED:

Dean, School of Fisheries and Ocean Sciences

Dean of the Graduate School

November 10, 2003

Date

IDEALIZED MODELING OF SEASONAL VARIATION IN THE ALASKA COASTAL CURRENT

A

THESIS

Presented to the Faculty

of the University of Alaska Fairbanks

in Partial Fulfillment of the Requirements

for the Degree of

DOCTOR OF PHILOSOPHY

By

William James Williams, B.A., M.S.

Fairbanks, Alaska

May 2003

Abstract

Analytical and idealized-numerical models were used to understand the physical processes that govern the seasonal variation and fate of the freshwater in the Alaska Coastal Current (ACC). The ACC is forced by freshwater inflow and by mean easterly winds that cause downwelling over the shelf.

Two-dimensional modeling using a *line-source* buoyant inflow gives the coastal current depth $H = \frac{3^{2/3}}{2}\left(\frac{f^2Q^2}{g'}\right)t^{2/3}$ and coastal current width $Y_{2D} = 3^{1/3}\left(\frac{g'Q}{f^2}\right)^{1/3} t^{1/3}$, where f is the Coriolis frequency, g' is reduced gravity, Q is inflow rate and t is time since inflow began. Addition of downwelling wind-stress causes a steep coastal current front that intersects the bottom and is either convecting, stable and steady, or stable and oscillatory depending on $\frac{D}{\delta_*}$ and $\frac{b_y}{f^2}$, where D is bottom depth, δ_* is an Ekman depth and b_y is the cross-shelf buoyancy gradient.

Three-dimensional modeling of a *half-line* source initially develops two-dimensionally but becomes three-dimensional from a balance between coastal influx of buoyancy and its downstream transport. This balance results in a coastal current depth limit $H_{\max} = \left(\frac{2Qf}{g'}\right)^{1/2} x^{1/2}$, where x is along-shelf distance. This limit is unchanged under downwelling wind-stress and is reached on time scales of less than 1 month for the ACC. The half-line source coastal current width develops as Y_{2D} away from the beginning of

the line source. Imposition of a downwelling wind-stress τ results in an approximate balance among wind-stress and along- and cross-shelf momentum advection so that the current width is reduced to $Y_{wind} \approx L_D \left(\frac{Qf}{\tau / \rho_0} \right)^{1/2}$, where L_D is the Rossby radius of deformation.

Waves and eddying motions eventually grow in the half-line source coastal current with wavelengths proportional to the coastal current width and with a downstream phase speed slower than the maximum current speed. These features cause an offshore flux of buoyant water, a broader coastal current and accumulation of buoyancy on the shelf. Increasing downwelling wind stress reduces the effects of the instabilities. Although buoyancy accumulates on the shelf during most model runs, there is little accumulation under maximum winter downwelling wind-stress. This suggests that freshwater accumulates on the shelf from spring through fall, but is then transported downstream during winter.

Table of Contents

List of Figures

Acknowledgments

I would like to thank my advisor Tom Weingartner for many interesting discussions on the regional physical oceanography of Alaska and his continuous enthusiasm towards my work. He has also attentively and lucidly edited this thesis and provided helpful perspective to many previous conference presentations. I would also like to extend my appreciation to my thesis committee Al Hermann, Dave Musgrave, Igor Polyakov and Ken Coyle for their allowing me to jump through the firey hoops so necessary to a venture of this kind and for their speedy evaluation of this work.

During my studies, I had the good fortune to spend some time working with Al Hermann at the Pacific Marine Environmental Laboratory in Seattle. This thesis has benefited from continuing discussions with Al. It has also been a pleasure to work amongst the people here at the Institute of Marine Science. In particular, I have enjoyed many scientific discussions received much help from Seth Danielson and received excellent suggestions on numerical modeling from Kate Hedstrom during her lunchtime visits from the Arctic Region Supercomputing Center.

I would also like to thank all friends, here in Alaska and elsewhere, and family for their fundamental support and generosity. They provide a background of security and peacefulness that enables intellectual pursuits.

This research was funded through the North Pacific Marine Research program (NPMR) (http://www.sfos.uaf.edu/npmr), the GLOBEC Northeast Pacific Program (http://globec.oce.orst.edu/groups/nep/index.html), and a UAF Thesis Completion Fellowship. The numerical modeling was performed at the Artic Region Supercomputing Center (ARSC) (http://www.arsc.edu).

1. Introduction

The wind- and buoyancy-forced Alaska Coastal Current (ACC) is a year-round, swift ($20-180\ cm\ s^{-1}$), narrow ($\sim 35\ km$), coastally-trapped current with an average transport of $\sim 0.8\ Sv$ [*Johnson et al.*, 1988; *Stabeno et al.*, 1995]. The ACC most likely originates on the British Columbian shelf [*Royer*, 1998], flows northward along the inner shelf and through the island archipelago of southeast Alaska, before continuing westward along the south coast of Alaska. It eventually enters the Bering Sea through Unimak Pass in the western Gulf of Alaska [*Schumacher et al.*, 1982] (see Figure 1.1). Thus, it is one of the longest coastal currents in the global ocean, flowing over $2000\ km$ around the coastal Gulf. Estimates of the along-shelf baroclinic geostrophic transport from GLOBEC sections conducted since 1997 in the northwest Gulf of Alaska suggest that $\sim 70\%$ of the along-shelf transport is carried within the ACC. Consequently, the ACC is the most prominent circulation feature on the continental shelf of the Gulf of Alaska [*Royer*, 1998]. Its attributes suggest that is be an important shelf pathway by which climate signals, dissolved and suspended materials, and organisms are carried around the Gulf of Alaska and possibly into the Bering Sea.

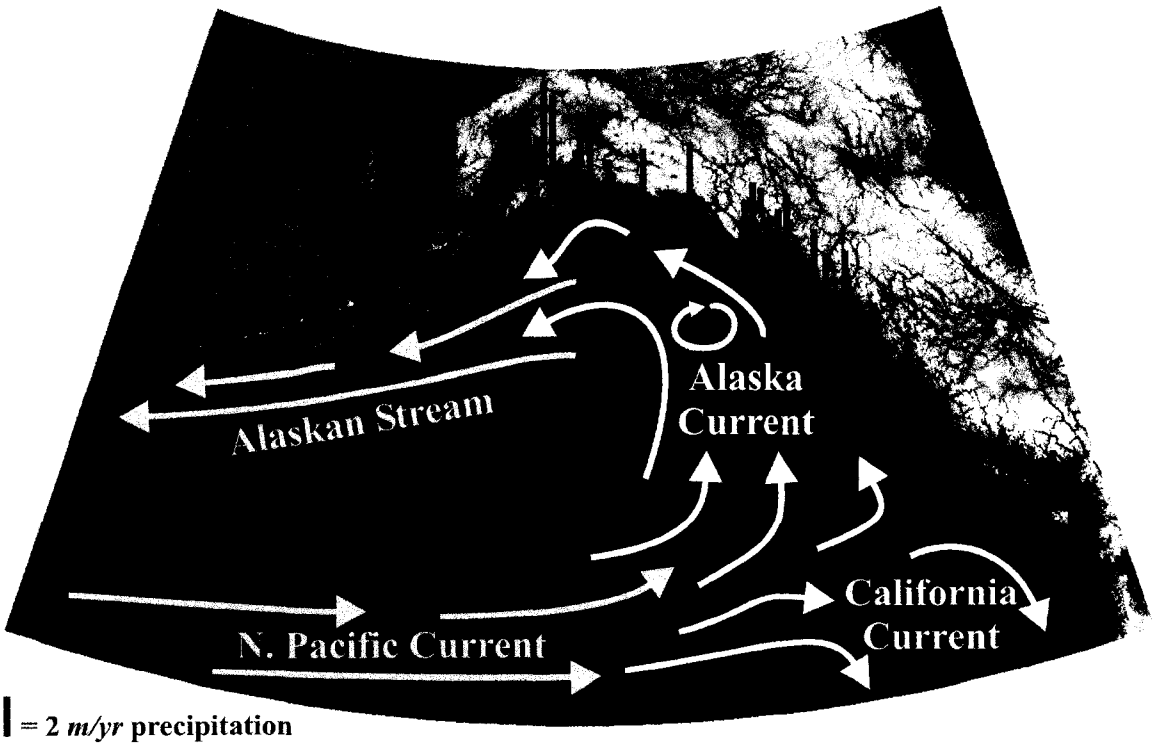

Figure 1.1: A map of the Gulf of Alaska. The general oceanic circulation around the Gulf (white, orange and pink arrows) and the buoyancy driven Alaska Coastal Current (ACC) (brown arrow) are shown. Mean annual precipitation near the coast from rain-gauges is shown by vertical black bars. (Figure courtesy of Seth Danielson.)

The ACC processes and re-distributes the enormous coastal freshwater discharge into the Gulf of Alaska, which *Royer* [1982] estimates to be $24,000\ m^3\ s^{-1}$. This discharge affects the shelf salinity, which primarily controls density differences and so is dynamically important. Apart from its size, the ACC is unusual for its distributed (rather than point source) buoyancy forcing and the mean downwelling wind-stress that prevails on the Gulf of Alaska shelf. This is the first theoretical study dedicated to understanding the dynamics of the ACC as a whole. It is motivated by the important role that freshwater plays in the ocean dynamics of the Gulf of Alaska shelf and slope, the importance of the coastal discharge to the freshwater budget of the northeast Pacific, and our rudimentary understanding of shelf dynamics in the Gulf of Alaska. It will aid in interpreting the recent observations of the ACC as part of the GLOBEC LTOP project and serves as a necessary step to understanding the more realistic but more complicated numerical simulations of the Gulf of Alaska currently being conducted by K. Hedstrom and A. J. Hermann, among others.

The goal of the study is to understand and describe the physical processes that govern the seasonal variation of the ACC by considering its unique buoyancy forcing and downwelling wind forcing. Of fundamental importance is the fate of the freshwater discharge onto this shelf and the processes responsible for its redistribution. Whether the freshwater remains on the shelf, is transported offshore into the central Gulf or alongshore into the Bering Sea is of considerable importance for understanding the oceanography of the northern North Pacific Ocean.

Previous studies of wind-forced downwelling in the coastal ocean consider 2-dimensional cross-shelf slices off the coast of Oregon [*Allen and Newberger*, 1996] and the near-shore environment at Duck, North Carolina [*Austin and Lentz*, 2002] but these do not involve buoyant inflow at the coast or a prescribed coastal current structure. Two-dimensional modeling of line-source inflow, again using a cross-shelf slice, has been considered extensively in *Kao* [1980], *Kao* [1981b], *Kao et al.* [1978] and *Kao et al.* [1977] and is revisited here for the special case pertinent to the realistic vertical mixing schemes now available. The combination of line source inflow and wind-forced downwelling is illustrated in *Chao* [1987] but is not considered in detail there. We therefore continue this line of investigation by considering the effect of persistent downwelling wind-stress, firstly on a coastal current density structure and then by including line source inflow.

Previous 3-dimensional models of buoyancy driven coastal currents can be split into two types. The first includes along-shelf extensions of the 2-dimensional line-source inflow, so that a periodic model is produced, such as *Griffiths and Linden* [1981] and *Griffiths and Linden* [1982], in which the instabilities of the coastal current are sought and described. The second comprises the numerous studies of the more common point source riverine input into the coastal ocean, such as *Fong and Geyer* [2001], *Fong and Geyer* [2002], *Muenchow and Garvine* [1993a], *Muenchow and Garvine* [1993b] and *Weingartner et al.* [1999], in which wind forcing of the coastal current is considered but the dynamics under wind-forced downwelling is again not considered in detail.

Both analytical methods and idealized-numerical models are used in this study. Chapter 2 models the ACC from a 2-dimensional perspective using a cross-shelf slice through the coastal current as a model domain and Chapter 3 provides more realism by modeling the ACC in a fully 3-dimensional fashion. Chapter 4 provides a summary and suggests future research directions.

Chapter 2 begins by introducing the ACC and providing further background to the physical setting and meteorological forcing of the northern Gulf of Alaska shelf. An analytical 2-dimensional model is then developed of a surface to bottom density front subjected to downwelling wind-stress, which is then extended through the use of a numerical model. An overview of the numerical model used is given followed by results showing the steepening of a front due to downwelling wind-stress and a comparison with the analytical model. Expressions are developed for the direction and size of the cross-shelf transport within the front, the angle of the front in the steady state, and the conditions under which the front is either convecting, stable and steady, or stable and oscillatory. The relaxation of the front on cessation of the wind-stress, and role of symmetric instability and sloping bottom topography are also considered. The latter part of the chapter concerns the introduction of freshwater at the coast, also into a 2-dimensional cross-shelf slice. A 1½-layer, zero-potential-vorticity analytical model is used with these and compared again to a numerical model of freshwater inflow. The

numerical model is then extended to include both downwelling wind-stress and freshwater inflow.

Chapter 3 begins by considering a 3-dimensional, half-line-source buoyancy driven coastal current as a more accurate but still simplified model of the ACC. This is first considered using a no wind-stress 1½-layer analytical model in which depth and time scales for the coastal current are developed. As in Chapter 2, the analytical model is then compared to a numerical model. An overview of the numerical model is given followed by results using no wind-stress and constant downwelling wind-stress. Width scales for the coastal current under no wind-stress and downwelling wind-stress conditions are provided and the instabilities and eddying motions present in the coastal current are described. The offshore versus alongshore fate of the inflowing water in the numerical model is considered and the implications of this for the Gulf of Alaska are discussed.

2. Idealized 2-dimensional modeling of the Alaska Coastal Current

2.1 Introduction

The Alaska Coastal Current (ACC) is a $\sim 35\ km$ wide, continuous flow of buoyant water that circumscribes the entire Gulf of Alaska shelf for over $2000\ km$ from its origins in the southeastern Gulf to Unimak Pass in the Aleutian Island chain where it enters the Bering Sea (see Figure 1.1). It is due to the enormous distributed freshwater runoff from the surrounding coast (which forms $\sim 40\%$ of the total freshwater input to the North Pacific [*Reed and Schumacher*, 1986; *Royer*, 1982]) and the prevailing downwelling wind-stress. These features and the large depth near the coastline (about 150 to $200\ m$) make the ACC a unique coastal current. Freshwater runoff within the ACC can either be mixed across the shelf towards the shelf-break or transported alongshore to ultimately flow into the Bering Sea. The physical processes that occur within the ACC in response to the distributed buoyancy forcing and downwelling wind-stress govern the fate of the

fresh water. These processes are therefore important both to the freshwater distribution within the North Pacific and to the ecosystems within the ACC and over the Gulf of Alaska shelf.

Recent observations of the ACC as part of the Global Ocean Ecosystems Dynamics Experiment (GLOBEC) Gulf of Alaska Program indicate that the ACC is a biologically important feature. The ACC has a distinct phyto- and zooplankton community [*S. L. Strom, K. O. Coyle,* pers. comm.] and it appears to be an important migratory corridor for young-of-the-year salmon advected within it [*Boldt,* 2001]. The physical structure of the ACC is likely important to the ecosystem there, as has been suggested for other ocean fronts [*Franks*, 1992a; *Franks*, 1992b; *Gallager et al.*, 1996]. For example, regions of horizontal convergence may concentrate plankton [*Epstein and Beardsley*, 2001], cross-shelf mixing may cause young-of-the-year salmon to be lost offshore [*Boldt*, 2001] and vertical mixing can bring nutrient-rich deep water to the surface fostering new production [*Eppley and Peterson*, 1979].

The wind-stress over the Gulf of Alaska shelf is not well known due to a scarcity of appropriate wind measurements, limited to a few NOAA coastal weather stations and buoys, and the anticipated strong orographic effects of the coastal mountain ranges. Because of the lack of data, geostrophic winds derived from the pressure fields of meteorological now-casts are often chosen to represent the wind field over the shelf, despite the omission of local orographic effects in such as barrier jets [*Overland and*

Bond, 1995] and intense winds though gaps in the Alaska Range that are suggested by SAR imagery [*Macklin et al.*, 1988]. Estimates of the seasonal variation of the monthly mean upwelling index (from the Pacific Fisheries Environmental Laboratory, that uses large-scale now-cast wind fields) and discharge [*Royer*, 1982] for the Gulf of Alaska are shown in Figure 2.1. The downwelling wind-stress is large during fall/winter (a consequence of storms associated with the Aleutian Low) and then relaxes during spring and summer to near-zero or slightly-upwelling values. The buoyancy-influx, however, is minimal in winter, when precipitation is stored as snow and ice, and then increases during the spring and summer due to snow melt (which peaks in July) and precipitation (which is maximal in fall). The structure of the ACC varies in response to the seasonally varying runoff and wind-stress. Figure 2.3 shows the cross shelf salinity structure of the ACC from the Cape Fairfield Line and Seward Line in the Northern Gulf (see Figure 2.2 for locations) during April, August, and December 1999. The structure of the ACC is best captured in the Cape Fairfield Line. At the end of the winter, in April, the isohalines are relatively steep and the ACC is narrow ($< 10\ km$ wide). This appears to be a response to the large winter downwelling wind-stress and low freshwater discharge. By August the ACC is much wider ($30 - 50\ km$ wide), shallower ($50 m$ deep), fresher and the isohalines across the entire shelf have relaxed to a more horizontal position. In December, after the maximum influx of freshwater and during strong downwelling wind-stress, the ACC is both wide ($\sim 30\ km$) and deep ($\sim 100\ m$).

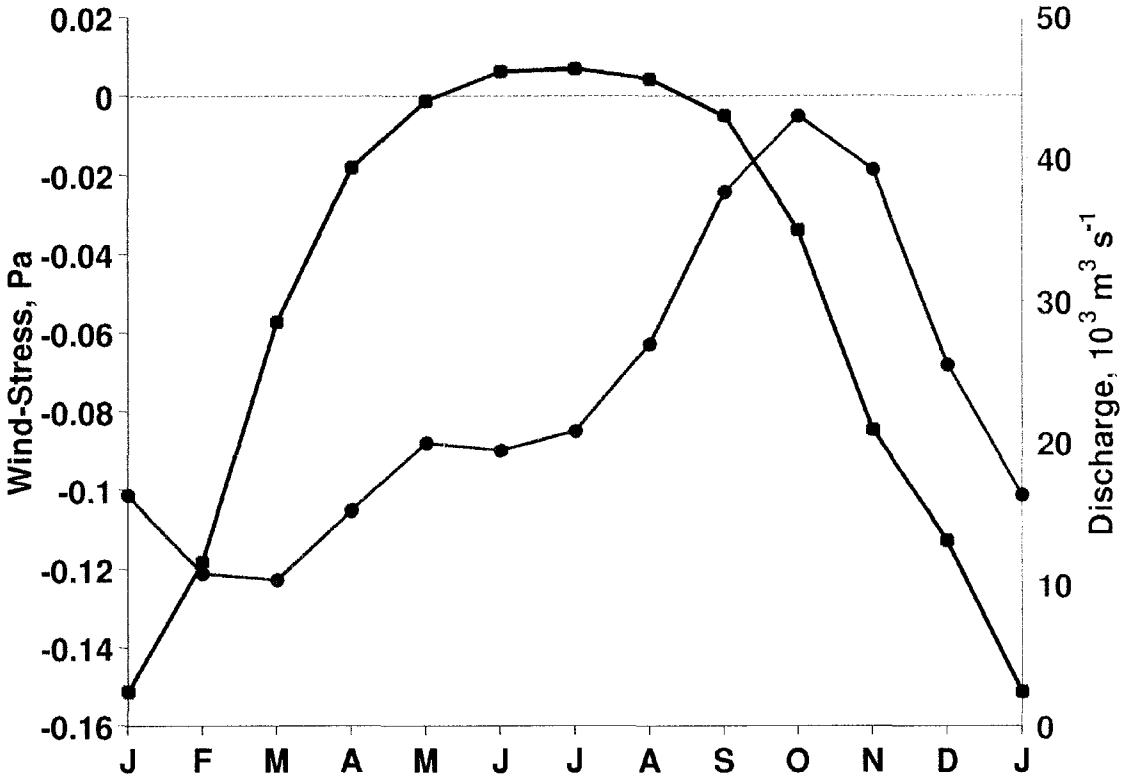

Figure 2.1: The seasonal variation of upwelling wind-stress and coastal freshwater discharge in the Gulf of Alaska. The mean monthly upwelling wind-stress (blue) is from the northern Gulf at 60°N 149°W and is calculated from the upwelling index for that location provided by the Pacific Fisheries Environmental Laboratory (PFEL). The mean monthly coastal freshwater discharge into the Gulf of Alaska (red) is an estimate from T. Royer [*Royer*, 1982].

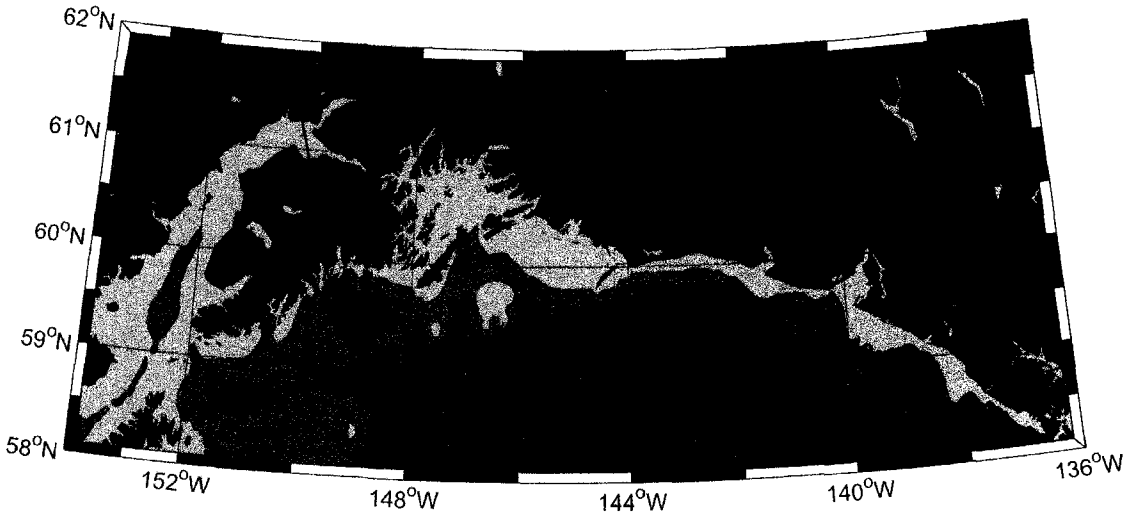

Figure 2.2: A map of the northern Gulf of Alaska. The location is shown of the Cape Fairfield Line and the Seward Line CTD sections (see Figure 2.3), and Middleton Island. Note also the complicated coastline and bottom topography of the Gulf of Alaska Shelf.

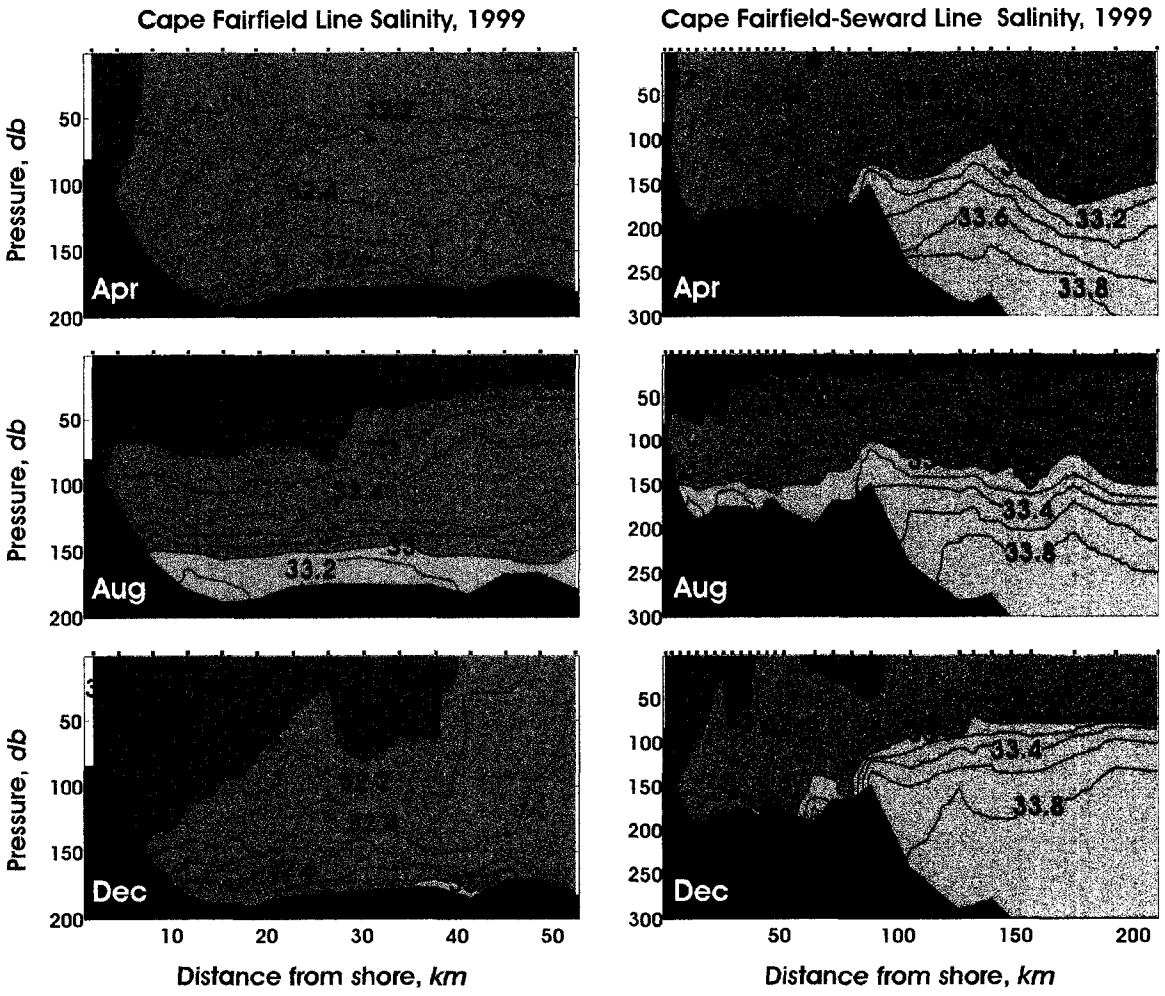

Figure 2.3: Salinity CTD sections of the Cape Fairfield Line and of the Cape Fairfield Line continued offshore along the Seward Line for April, August and December of 1999.

The Gulf of Alaska shelf has large variations in width. For example, the southeastern part of Figure 2.2 near Cape Fairweather has a shelf width of about 100 *km* (the distance from shore to the 200 *m* isobath) that narrows towards the west to about 30 *km* near Kayak Island and then widens rapidly to $150-200$ *km* offshore of Prince William Sound and the Kenai Peninsula. The shelf width near the Seward Line is approximately 200 *km* (see Figure 2.3), much wider than the ACC in all seasons. There is therefore little possibility of direct interaction between the ACC and the frontal flows associated with the shelf break in this region. The fresher water that is contained within the ACC must therefore be transported across a 'mid-shelf' region, presumably by wind events or mixing by eddies, in order to reach the shelf break. Cross-shelf transport of this kind is possibly occurring between April and August 1999 on the Seward Line (Figure 2.3), buoyant water of salinity < 32 being found at the shelf break in August but not in April. Further to the east in the Gulf of Alaska the narrower shelf allows the possibility of direct interaction between the ACC and the shelf break, particularly at Kayak Island where the shelf in the northern Gulf is at its narrowest.

To address the question of the fate of the freshwater contained within the ACC, whether it is transported offshore into the deep Gulf of Alaska, or whether it flows with the ACC into the Bering Sea through Unimak Pass in the Aleutian Island chain, we present analytical and numerical modeling of the ACC. The models attempt to reproduce the seasonal variation of the ACC's cross-shelf structure from a 2-dimensional perspective, in which no alongshore variation is allowed. Freshwater runoff into the Gulf of Alaska is

therefore modeled as an infinite line-source and, since the estimated mean wind-stress is strongly downwelling favorable for much of the year, the effect of downwelling wind-stress on such a coastal current is also explored. This modeling does not attempt to provide a realistic simulation of the ACC, but rather aims to develop understanding of the physical processes that occur when such a coastal current is subjected to downwelling wind-stress, and to consider the possible implications of these processes to the nutrient and plankton distributions near the ACC. It is also a useful precursor to the more realistic 3-dimensional modeling presented in the next chapter.

The chapter is structured as follows. We begin with a model of a near-vertical surface-to-bottom density front subjected to a constant downwelling wind-stress and no inflow at the coast. This both very roughly approximates the ACC in winter and is perhaps the simplest way to initiate our investigation. It is also interesting from a dynamical standpoint and builds upon detailed studies of downwelling by *Allen and Newberger* [1996], motivated by downwelling winds off the coast of Oregon, and by *Austin and Lentz* [2002] for the near-shore environment off of Duck, North Carolina. Following this, freshwater inflow at the coast is introduced into a constant density ocean, first with no wind-stress (similar to *Kao* [1980] and *Kao* [1981b] but with variable vertical diffusivity provided by a turbulent closure scheme and minimal horizontal diffusivity) and then with downwelling wind-stress.

The effect of downwelling wind-stress on a buoyancy-driven coastal current has been illustrated by previous numerical modeling studies. *Fong* [2001] applied downwelling wind-stress for 24 hours to a plume of buoyant inflow water representative of the Kennebec River in the Gulf of Maine, and *Chao* [1987] applied constant downwelling wind-stress to a 2-dimensional model with a line source of buoyant water. In both cases, a general narrowing and deepening of the coastal current due to the onshore downwelling Ekman transport occurred but the downwelling case is not considered in detail. These studies were also not concerned with the seasonal evolution of the coastal currents they modeled.

2.2 No coastal inflow of buoyant water, downwelling wind-stress

2.2.1 Analytical model

The result of frontal steepening due to downwelling wind-stress can be simply modeled by considering the steady state produced by an imposed cross-shelf density gradient forced by a constant downwelling wind-stress. The model geometry used here is shown in Figure 2.4 and is initially kept as simple as possible by using a flat bottom ocean and a distant coastal wall. In this 2-dimensional steady state model, there is no along-shelf

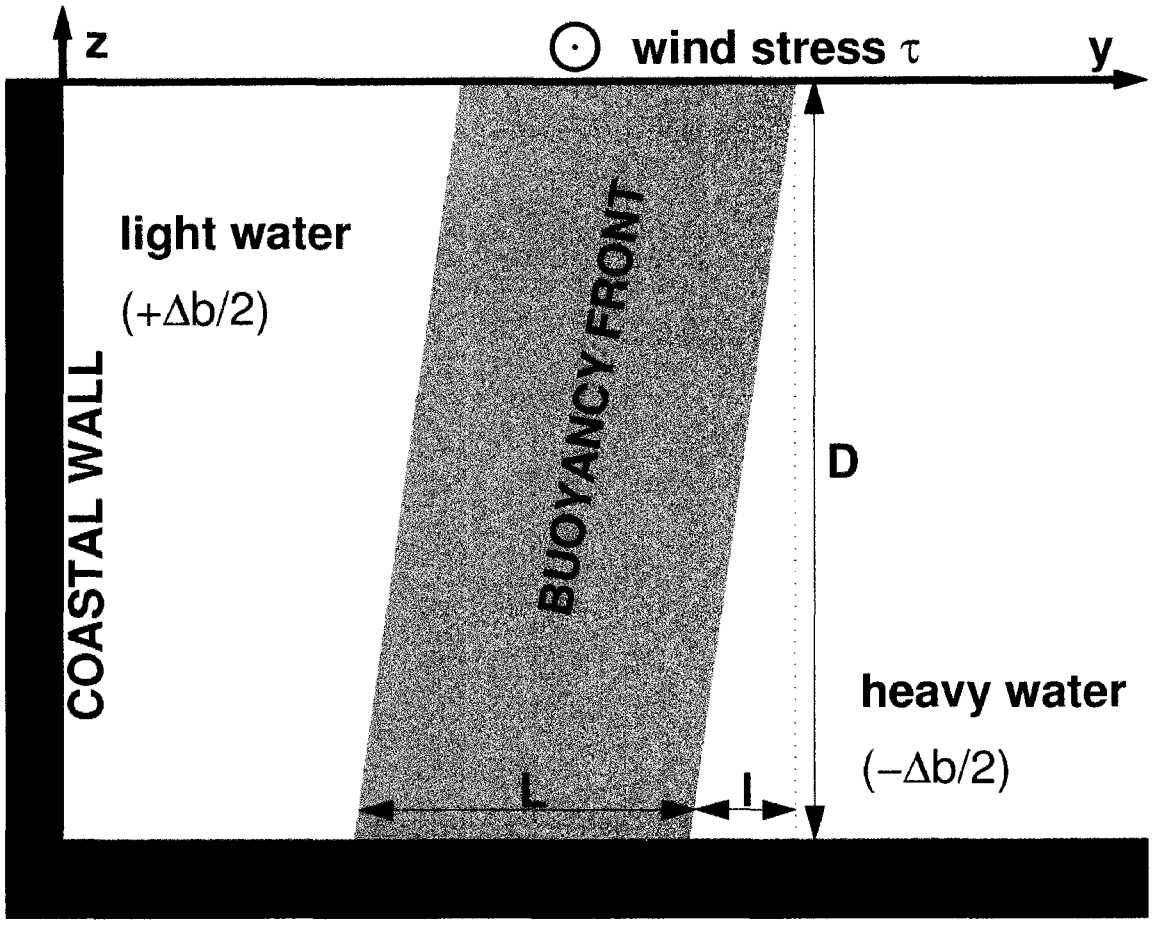

Figure 2.4: A schematic of the model used to study the effect of downwelling wind-stress on a surface-to-bottom density front. A cross-shelf slice through a steep density front is depicted with light water against the coast and dense water offshore. The width of the front is L, the horizontal span of an isopycnal within the front is l and the depth of the ocean is D. An along-shelf wind-stress τ can be applied in the downwelling direction (towards the reader). The coordinates are z positive upward, y positive offshore, and x increasing along-shore towards the reader.

variation in any variable and no variation with time. This allows us to simplify the momentum equations to

$$\begin{aligned} vu_y + wu_z - fv &= (A_V u_z)_z, && \text{along-shelf momentum} \\ vv_y + wv_z + fu &= -\phi_y + (A_V v_z)_z, && \text{cross-shelf momentum} \\ \phi_z &= b, && \text{hydrostatic vertical momentum} \\ v_y + w_z &= 0, && \text{continuity} \\ vb_y &= (K_V b_z)_z, && \text{buoyancy} \end{aligned} \tag{2.1}$$

where subscripts denote partial differentiation, y is the cross-shelf coordinate, z is the vertical coordinate, (u,v) are the velocities in the (x,y) directions, f is the Coriolis parameter, $\phi = P/\rho_0$ where P is pressure and ρ_0 is the background density, $b = -g\rho/\rho_0$ is the buoyancy where g is the acceleration due to gravity and ρ is the perturbation density so that the total density $\rho_T = \rho_0 + \rho$, and A_V and K_V are the vertical, kinematic, eddy-viscosity and eddy diffusivity respectively. The dynamics are Boussinesq, hydrostatic, and ignore horizontal viscosity and diffusivity.

These equations can be solved after linearizing the horizontal momentum equations by assuming small Rossby numbers. Estimates of the Rossby number for each non-linear term can be made by using the fact that the ACC is long and thin so that cross–shelf length scales are small in comparison to along-shelf length scales. This gives small Rossby numbers in the cross-shelf momentum equation but shows that the Rossby number is not necessarily small in the along-shelf momentum equation. Nevertheless, we

assume small Rossby numbers for both equations here and check the validity of the assumption in the numerical modeling section of this chapter.

In linearizing the buoyancy equation, we consider the relative magnitude of the vertical advection of buoyancy (wb_z) to the horizontal advection of buoyancy (vb_y). This is estimated

$$O\left(\frac{wb_z}{vb_y}\right) \sim \frac{WL\Delta_z b}{VD\Delta_y b}, \tag{2.2}$$

where $\Delta_z b$ is the change in buoyancy between the bottom and top of the front, $\Delta_y b$ is the change in buoyancy across the front, W is a scale for the vertical velocity, and V is a scale for the cross shelf velocity, L is the width of the front and D is the depth of the ocean. From the continuity equation $WL/VH \sim 1$ and from inspection of Figure 2.4 we see that $\frac{\Delta_z b}{\Delta_y b} \sim \frac{l}{L}$, where l is the horizontal span of an isopycnal, so that

$$O\left(\frac{wb_z}{vb_y}\right) \sim \frac{l}{L}. \tag{2.3}$$

Downwelling wind-stress is expected to cause the front to steepen, reducing the value of l/L and suggesting $l/L \ll 1$ as a possibility for a steady state. L is the width of the front and is prescribed initially whereas l is the horizontal span of an isopycnal in the buoyancy front and is a function of the solution. We therefore construct the analytical model with large enough L to ensure $l/L \ll 1$. This allows us to ignore vertical advection of buoyancy in comparison to horizontal advection.

The horizontal momentum equations for the analytical model are now

$$\begin{aligned} -fv &= (A_V\, u_z)_z, && \text{along-shelf momentum} \\ +fu &= -\phi_y + (A_V v_z)_z, && \text{cross-shelf momentum} \end{aligned} \tag{2.4}$$

Taking the vertical derivative of the cross-shelf momentum equation and using the hydrostatic equation yields

$$+fu_z = -b_y + (A_V v_z)_{zz}. \tag{2.5}$$

The buoyancy terms in these equations contain b_y which can be simplified by writing

$$b(y,z) = b_1(y) + b_2(y,z), \tag{2.6}$$

where b_1 is the vertical-mean buoyancy

$$b_1 = \frac{1}{D}\int_D^0 b(y,z)dz, \tag{2.7}$$

and b_2 is the remainder. If l/L is small $b_{1y} \gg b_{2y}$ and

$$b_y \approx b_{1y}. \tag{2.8}$$

This can be substituted into the equations, which yields

$$\begin{aligned} -fv &= (A_V u_z)_z, \\ +fu_z &= -b_{1y} + (A_V v_z)_{zz}, \\ vb_{1y} &= (K_V b_z)_z, \\ v_y + w_z &= 0. \end{aligned} \tag{2.9}$$

After specification of b_{1y}, equations (2.9) form a linear, 1-dimensional set that can simply be solved for vertical profiles of u, v, b and w at any cross-shelf location. The boundary conditions used here are:

- Surface-stress is equal to the wind-stress so $A_V u_z = \tau^{wind}/\rho_0$ and $v_z = 0$ at $z = 0$.

- There is no flow through the coastal wall, so $\int_{-D}^{0} v dz = 0$. A vertical integral of the first equation of (2.9) shows that in the steady state the along-shelf bottom-stress is equal to the along-shelf surface-stress, so $A_V u_z = \tau^{wind} / \rho_0$ at $z = -D$.
- There is no buoyancy flux through the seafloor or surface, so $K_V \rho_z = 0$ at $z = 0, -D$.

A bottom stress boundary condition is also needed that links the bottom stress to the interior flow for a turbulent boundary layer. Simple linear friction is used here so that $A_V u_z = ru$, $A_V v_z = rv$ at $z = -D$ where r is the linear bottom friction coefficient.

The full analytical solution is

$$
\begin{aligned}
u = {} & \frac{\tau}{\rho_0 r} - \frac{b_{1y}}{f}(z + D) + \frac{\delta}{2f}\left(\frac{f(\tau/\rho_0)}{A_V} + b_{1y}\right)\times \\
& [B(\cosh(z/\delta)\cos(z/\delta) - \cosh(D/\delta)\cos(D/\delta)) \\
& - A(\sinh(z/\delta)\sin(z/\delta) - \sinh(D/\delta)\sin(D/\delta)) \\
& - (\sinh(z/\delta)\cos(z/\delta) - \sinh(D/\delta)\cos(D/\delta)) \\
& - (\cosh(z/\delta)\sin(z/\delta) - \cosh(D/\delta)\sin(D/\delta))], \\
v = {} & \frac{\delta^3}{4A_V}\left(\frac{f(\tau/\rho_0)}{A_V} + b_{1y}\right)\times \\
& [A\cosh(z/\delta)\cos(z/\delta) + B\sinh(z/\delta)\sin(z/\delta) \\
& + \cosh(z/\delta)\sin(z/\delta) - \sinh(z/\delta)\cosh(z/\delta)], \\
b = {} & \frac{\delta^5 b_{1y}}{8K_V A_V}\left(\frac{f(\tau/\rho_0)}{A_V} + b_{1y}\right)\times \\
& [A\sinh(z/\delta)\sin(z/\delta) + B(1 - \cosh(z/\delta)\cos(z/\delta)) \\
& + \frac{2z}{\delta} - \sinh(z/\delta)\cos(z/\delta) + \cosh(z/\delta)\sin(z/\delta)],
\end{aligned}
\tag{2.10}
$$

where $\delta = \sqrt{\frac{2A_V}{f}}$ is the standard Ekman layer depth, b has been arbitrarily set to zero at the surface, and

$$A = \frac{[\sin(D/\delta) - \sinh(D/\delta)][2\cos(D/\delta) - 2\cosh(D/\delta) + (r\delta/A_V)(\sin(D/\delta) - \sinh(D/\delta))]}{\cos(2D/\delta) - \cosh(2D/\delta) + (r\delta/A_V)(\cos(D/\delta)\sin(D/\delta) - \cosh(D/\delta)\sinh(D/\delta))},$$

$$B = \frac{[\cos(D/\delta) - \cosh(D/\delta)][2\sin(D/\delta) + 2\sinh(D/\delta) - (r\delta/A_V)(\cos(D/\delta) - \cosh(D/\delta))]}{\cos(2D/\delta) - \cosh(2D/\delta) + (r\delta/A_V)(\cos(D/\delta)\sin(D/\delta) - \cosh(D/\delta)\sinh(D/\delta))}.$$

Figure 2.5 shows a solution to the analytical model for $D = 50\,m$, $\tau = 0.1\,Pa$, $K_V = A_V = 0.05\,m^2 s^{-1}$, $L = 10\,km$, $\Delta\rho = 1\,kg\,m^{-3}$ and $r = 4.5\times10^{-4}\,m^2 s^{-1}$. The isopycnals are nearly vertical (Figure 2.5(a)) (easily satisfying $l/L \ll 1$) and there is a surface intensified along-shelf jet within the front due to dominant cross-shelf, thermal-wind balance (Figure 2.5(b)). At the bottom there is an along shelf flow, which is necessary to create an along-shelf bottom stress equal in magnitude to the surface stress that allows a steady state. The cross-shelf stream function (Figure 2.5(d)) has three circulation cells; the cell within the front has offshore flow at the surface and the cells on either side of the front have onshore flow at the surface. Between circulation cells on either side of the front there is no cross-shelf flow. Here, the thermal-wind shear in the along-shelf flow, calculated from the prescribed cross-shelf buoyancy gradient, provides the along-shelf stress in the water column that is equal to the applied wind-stress. This occurs when

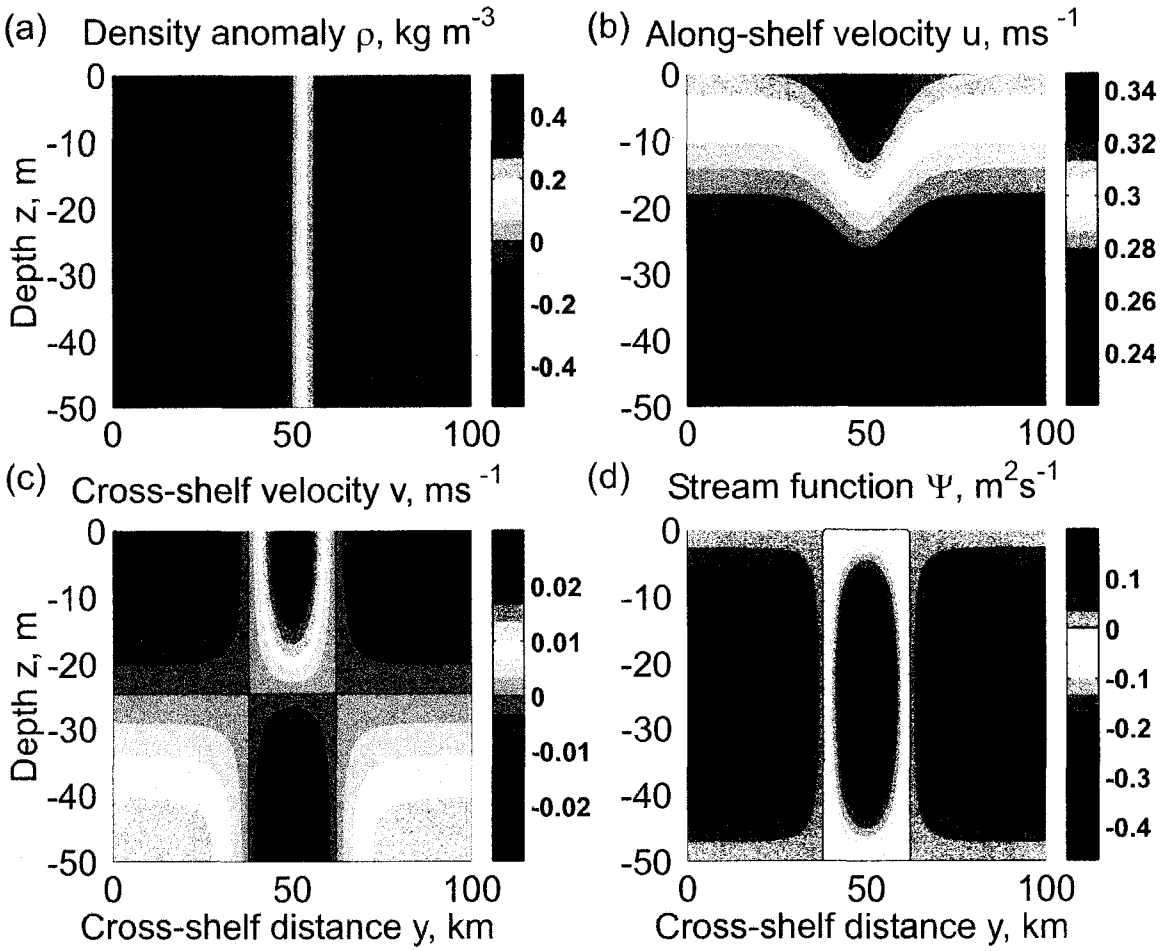

Figure 2.5: Analytical solutions of the steady state produced by a constant downwelling wind-stress acting on a surface-to-bottom density front. They are constructed from equations (2.10) and show (a) density anomaly ρ, (b) along-shelf velocity u, (c) cross-shelf velocity v and (d) cross-shelf stream-function Ψ. The vertical diffusivity K_V and eddy viscosity A_V are constant and set to 0.05 $m^2 s^{-1}$, and the downwelling wind-stress $\tau = 0.1\ Pa$.

$$-\frac{f\tau^{wind}}{\rho_0 b_{1y} K_V} = 1. \tag{2.11}$$

In this special case, the interior thermal wind balance satisfies all boundary conditions on stress and therefore boundary layers are not required. From equations (2.9), we see that the cross-shelf velocity is zero (Figure 2.5(c)), there is no variation of buoyancy with depth and the along-shelf flow is in exact geostrophic balance.

Away from the front the along-shelf stress in the water column, due to the thermal-wind shear, is less than the wind-stress ($-f\tau^{wind}\rho_0 / b_{1y}k_V > 1$) requiring onshore flow at the surface. Within the front the opposite is true ($-f\tau^{wind}\rho_0 / b_{1y}k_V < 1$), requiring offshore flow at the surface (Figure 2.5(c)). If the wind-stress is increased from 0.1 to 0.5 *Pa* then $-f\tau^{wind}\rho_0 / b_{1y}k_V > 1$ everywhere, and the cross-shelf flow does not change direction within the front but slows down there (see Figure 2.6).

In Figure 2.5, the water column is stable within the front, where the boundary layers tend to advect light water over dense water, and unstable at the margins of the front, where they tend to advect dense water over light water. In Figure 2.6 the water column is unstable everywhere. In both cases the vertical eddy diffusivity was chosen to be large enough to roughly simulate convection in the unstable regions, and this is also large enough so that the surface and bottom boundary layers intersect ($D/\delta < 2$). Obviously, a

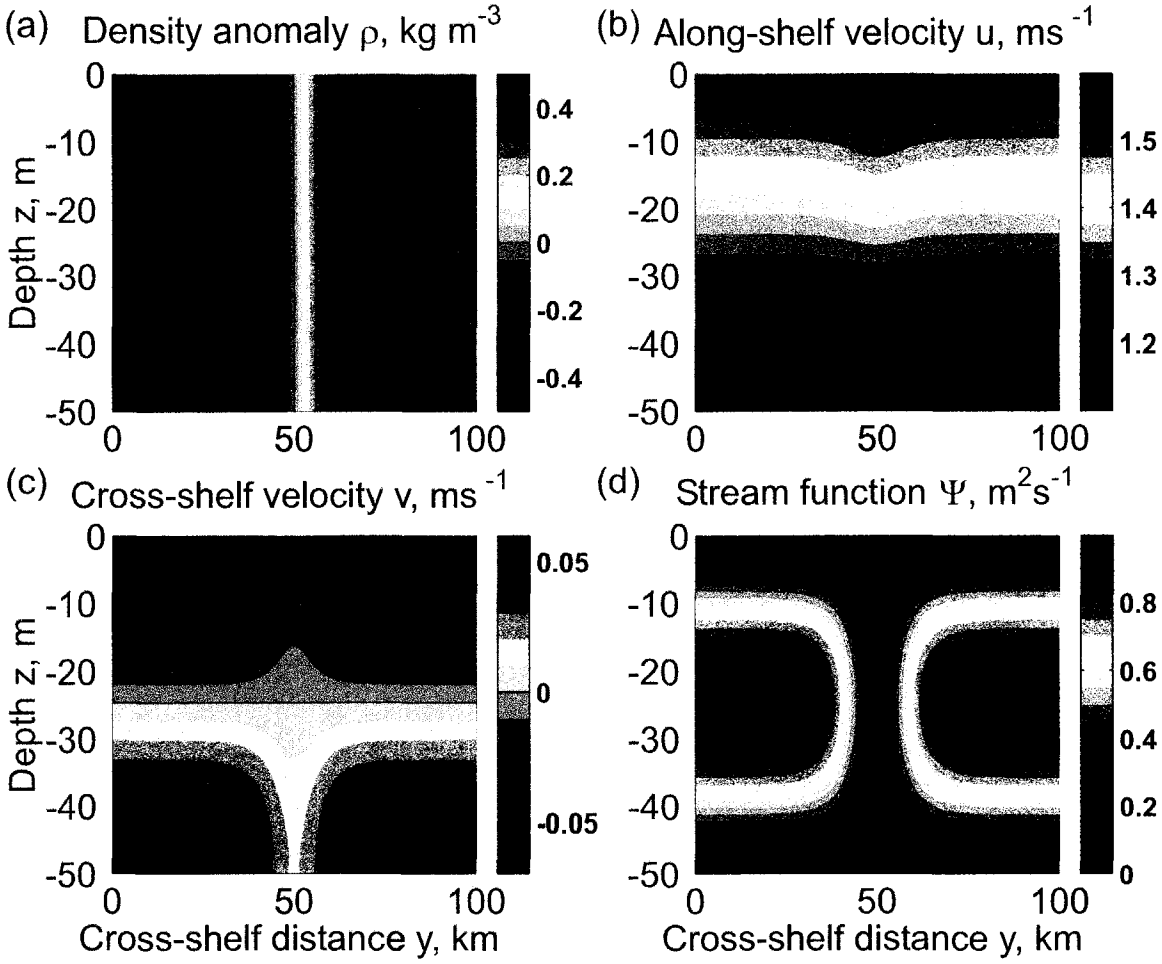

Figure 2.6: Solutions to the analytical model for parameters identical to Figure 2.5 except that the wind-stress is increased to $\tau = 0.5\,Pa$ from $\tau = 0.1\ Pa$. As for Figure 2.5, the panels are: (a) density anomaly ρ, (b) along-shelf velocity u, (c) cross-shelf velocity v and (d) cross-shelf stream-function Ψ. Note that in contrast to Figure 2.5, the surface and bottom cross-shelf flow no longer changes direction within the front.

far better model is to have a varying diffusivity that is dependent on the velocity and density fields, so that there are large values of diffusivity where convection occurs and smaller values where the water column is stable. Several turbulent closure schemes are employed to do this in the numerical model described next. Using the numerical model, we both explore cases where the surface and bottom boundary layers intersect and where they are separate.

2.2.2 Numerical model

The numerical model used to solve for the flow fields shown is the Regional Ocean Modeling System (ROMS) [*Shchepetkin and McWilliams*, 2000]. The model is a free-surface, *s*-coordinate, 3-dimensional primitive equation, finite-difference model and, while it is more complex than the present study requires, it allows for the 2-dimensional study in this chapter and for subsequent modeling of 3-dimensional effects.

The equations solved by ROMS are:

$$
\begin{aligned}
&u_t + (\mathrm{u}\bullet\nabla)u - fv = -\phi_x + A_H(u_{xx} + u_{yy}) + (A_V u_z)_z, \\
&v_t + (\mathrm{u}\bullet\nabla)v + fu = -\phi_y + A_H(v_{xx} + v_{yy}) + (A_V v_z)_z, \\
&\phi_z = -b, \\
&u_x + v_y + w_z = 0, \\
&b_t + (\mathrm{u}\bullet\nabla)b = K_H(b_{xx} + b_{yy}) + (K_V\ b_z)_z,
\end{aligned}
\tag{2.12}
$$

where subscripts denote partial differentiation. ROMS actually solves equations for temperature and salinity and then uses an equation of state to calculate density. However, this chapter uses only salinity and a linear equation of state so that ROMS solves the buoyancy equation in (2.12). A_H and K_H are the horizontal eddy viscosity and diffusivity respectively, and were typically either set to zero in the 2-dimensional modeling presented here, relying on the small hyper-diffusivity inherent in its third-order upwind advection scheme to dampen numerical noise in the model, or set to the small value of 2 $m^2 s^{-1}$.

The vertical diffusivities in these numerical experiments were typically calculated using a Mellor-Yamada level 2.5 turbulence closure scheme embedded within ROMS [*Mellor and Yamada*, 1982] which uses the limitation on the mixing length scale suggested by *Galperin et al.* [1988] and the stability function suggested by *Kantha and Clayson* [1994]. A background vertical eddy diffusivity of 2×10^{-5} $m^2 s^{-1}$ was used in keeping with *Allen and Newberger* [1996].

The equations are subject to the surface and bottom boundary conditions of no flow and no buoyancy flux through the free-surface and through the bottom, surface stress due to the wind, and bottom stress. These boundary conditions are formulated:

$$\begin{aligned} &w = \eta_t \text{ at } z = \eta, \\ &uD_x + vD_y = 0 \text{ at } z = -D, \\ &A_V u_z = \tau / \rho_0, v_z = 0 \text{ at } z = \eta, \\ &A_V u_z = C_D(u^2 + v^2)u,\ A_V v_z = C_D(u^2 + v^2)v \text{ at } z = -D. \end{aligned} \tag{2.13}$$

where η is the free-surface height and C_D is a drag coefficient calculated as

$$C_D = \kappa^2 \left(\ln \frac{\Delta z_b}{z_0} \right) \tag{2.14}$$

where $\kappa = 0.4$ is von Karman's constant, $z_0 = 0.1\ m$ is the bottom 'roughness' scale and Δz_b is the distance from the bottom to the first horizontal velocity point on the numerical grid.

A no-slip boundary condition is applied at the coastal wall

$$v = 0,\ u = 0 \text{ at y} = 0, \tag{2.15}$$

and a no-gradient open boundary condition is applied on all variables at the offshore edge of the domain

$$u_y = v_y = b_y = 0. \tag{2.16}$$

This boundary condition is dynamically consistent with the Ekman outflow and inflow that is expected for steady states obtained in this model.

The ROMS model domain was made 2 dimensional by using the minimum of 3 or 4 grid points in the x-direction and specifying no-gradient in all variables across all x grid points as a boundary condition. The typical grid spacing was $1\ km$ in each horizontal direction and $1-3\ m$ resolution in the vertical, the vertical s-coordinates being used to giver higher vertical resolution in the surface and bottom boundary layers where necessary. The time step was chosen so that advection, wave propagation, and diffusion were properly resolved. Typically, there were 720 time steps in 24 hours, properly resolving vertical diffusion representing convection constraining the time step. Each experiment was run until the initial conditions had evolved to a steady, or quasi-steady, state. A few experiments were done at twice the horizontal and vertical resolution to test the accuracy of the flow fields at the lower resolution.

2.2.3 Initial conditions and spin up

The numerical model is initialized with a cross-shelf surface-to-bottom buoyancy front in which the along-shelf velocity is geostrophically balanced and the level of no motion is chosen to be at the bottom. The initial density field is specified as:

$$\rho = \frac{\Delta\rho}{2}\tanh\left(\frac{(y - y_0) - (z - z_0)/\tan\alpha}{L}\right) \tag{2.17}$$

where L is the width of the front, y_0 and z_0 is the location of the center of the front, $\Delta\rho$ is the density difference across the front and α is the angle of isopycnals within the front to the horizontal. This initial condition, though in geostrophic balance, does not satisfy no-stress boundary conditions at the surface and the bottom and so some evolution of the front occurs without applying any wind-stress.

When wind-stress is applied, it is smoothly increased over a two-day period to its maximum value to minimize transients, particularly inertial oscillations, during spin up.

2.2.4 Results

2.2.4.1 Steepening of the front

The analytical model gives the steady state produced by constant, downwelling wind-stress acting on a density front in a coastal ocean with large, constant vertical eddy diffusivity. A numerical model allows us to begin with a density front that is more gently sloping than the analytical steady state and follow its steepening over time, due to downwelling wind-stress, to a steady or quasi-steady state.

As an example, Figure 2.7 shows a model run where D, L and $\Delta\rho$ are the same as for the analytical model shown in Figure 2.5 except that the front is initialized close to the horizontal ($\alpha = 0.05^{\circ}$), so as to accentuate and lengthen the period of steepening, and the Mellor Yamada level 2.5 turbulence closure scheme is used. The response of the front to the wind-stress proceeds as follows. The downwelling wind-stress causes surface and bottom mixed layers to form that contain the bulk of the Ekman transport. Isopycnals within these mixed layers are essentially vertical. The onshore Ekman transport of the surface mixed layer and compensating offshore transport in the bottom boundary layer directly steepen the front through advection of the buoyancy gradient that forms the front. This advection tends to put dense water over light water at the interior edge of the boundary layers, which causes them to necessarily thicken as the front steepens. This mixed-layer deepening brings the surface and bottom mixed layers closer together, eroding the stratified region between them and slightly widening the front. Finally, in this case (where $D = 50\ m$), when the front is very steep the surface and bottom boundary

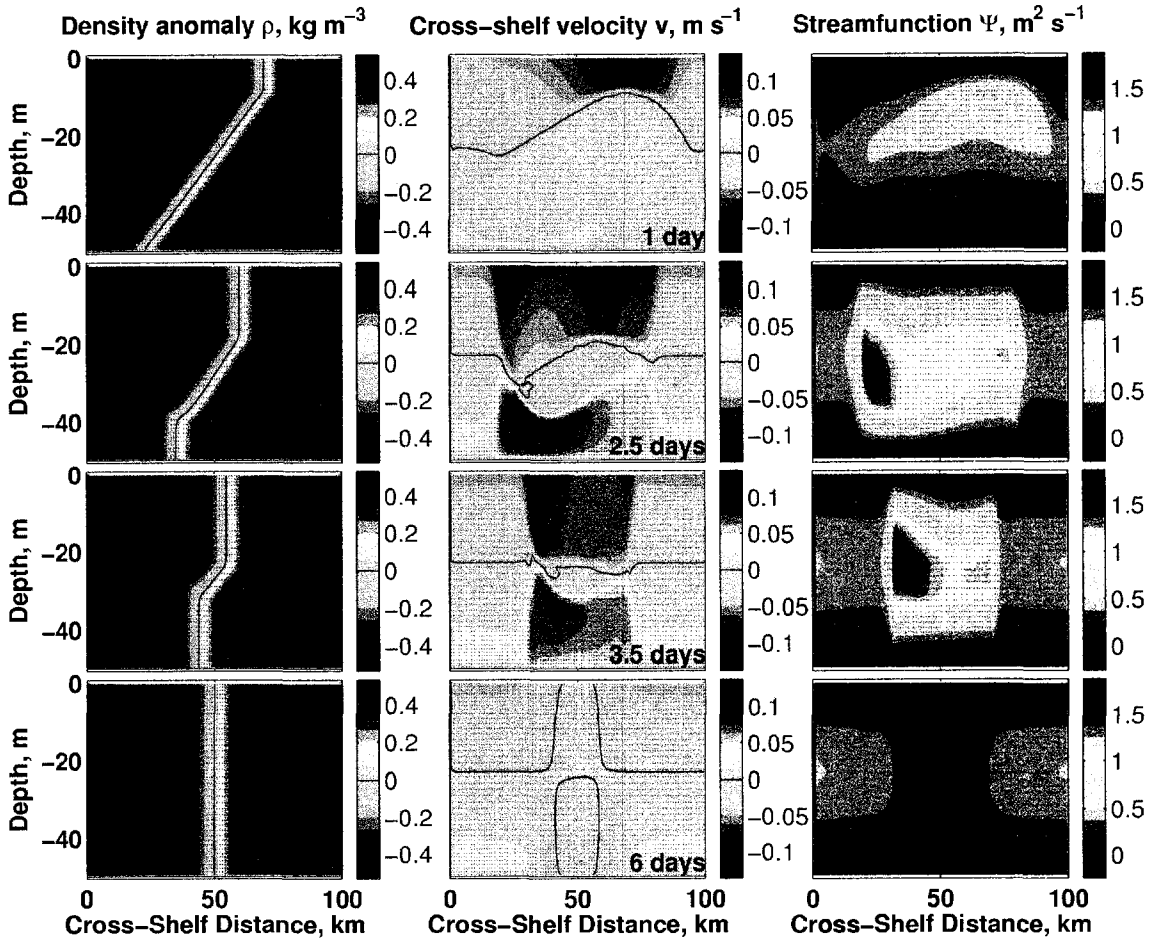

Figure 2.7: Numerical results showing the steepening of a surface-to-bottom density front due to downwelling wind-stress. The parameters are $L = 8\ km$, $\Delta\rho = 1\ kg\ m^{-3}$, $\tau = 0.1\ Pa$, the front is initialized at an angle of 0.05° to the horizontal to accentuate the steepening process, and a Mellor-Yamada level 2.5 sub-model is used to calculate vertical eddy diffusivities. The first column of plots is density anomaly, the second column cross-shelf velocity and the third cross-shelf stream-function. The rows of plots, from top to bottom, are at 1, 2.5, 3.5 and 6 days after turning on the wind-stress.

layers intersect and vertical diffusion of buoyancy can balance the horizontal advection of buoyancy as in the analytical model. The vertical eddy diffusivities are a maximum in the center of the water column at this point and a steady state has occurred that is roughly equivalent to the analytical model.

2.2.4.2 Verification of the analytical model

Figure 2.8 shows the steady state achieved using the numerical model with the same initial conditions and parameters as the analytical model shown in Figure 2.5 but with a coastal wall at y=0 and the vertical diffusivities specified by the Mellor-Yamada level 2.5 scheme. The numerical model results are qualitatively and quantitatively very similar to those of the analytical model, the major difference being the vertical eddy diffusivity field shown in Figure 2.8(d). Vertical eddy diffusivity is everywhere a maximum at mid-depth, indicating that the surface and bottom boundary layers intersect, a feature that is also clear in the momentum balance (see Figure 2.9). The mid-depth diffusivities are smallest at the center of the front, where the water column is stable, and largest at the edges of the front to represent convection where the water column is unstable.

The momentum and density balances found in the numerical modeling are essentially the same as the analytical model equations. An example is shown in Figure 2.9, in which vertical profiles of the terms in the momentum and density balances are plotted from the

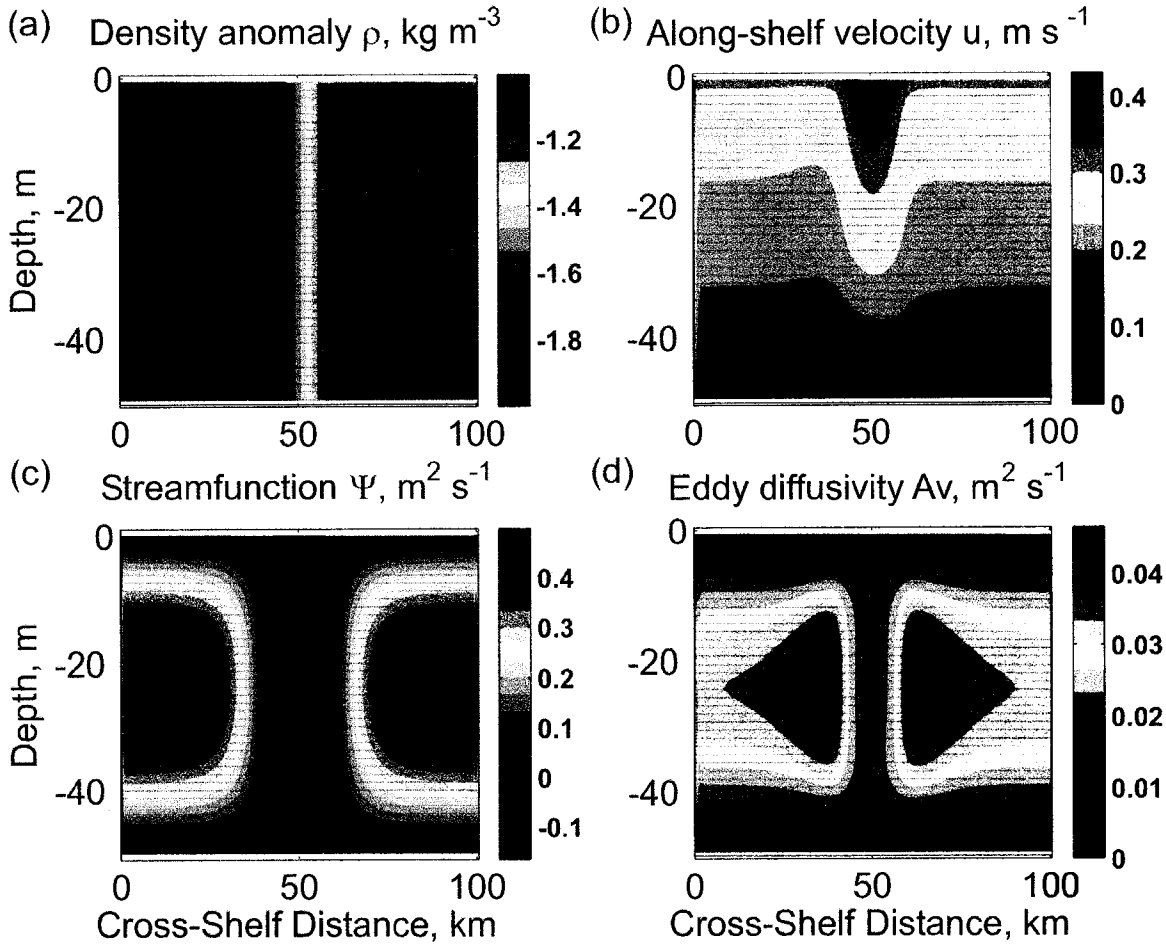

Figure 2.8: The cross-shelf velocity produced by a numerical model of a surface-to-bottom density front subjected to constant downwelling wind-stress. The parameters are identical to those used in the analytical model depicted in Figure 2.5, except for the vertical eddy diffusivities K_V and A_V which were generated by the Mellor-Yamada level 2.5 sub-model (see panel (d)). At the edges of the density front high values of the eddy diffusivity are found where the water is statically unstable and the mixing scheme is simulating convection. Within the front the water column is stable. The numerical results for the other parameters are very similar to the analytical model (compare Figures 2.5(a)-(c) with panels (a)-(c) here).

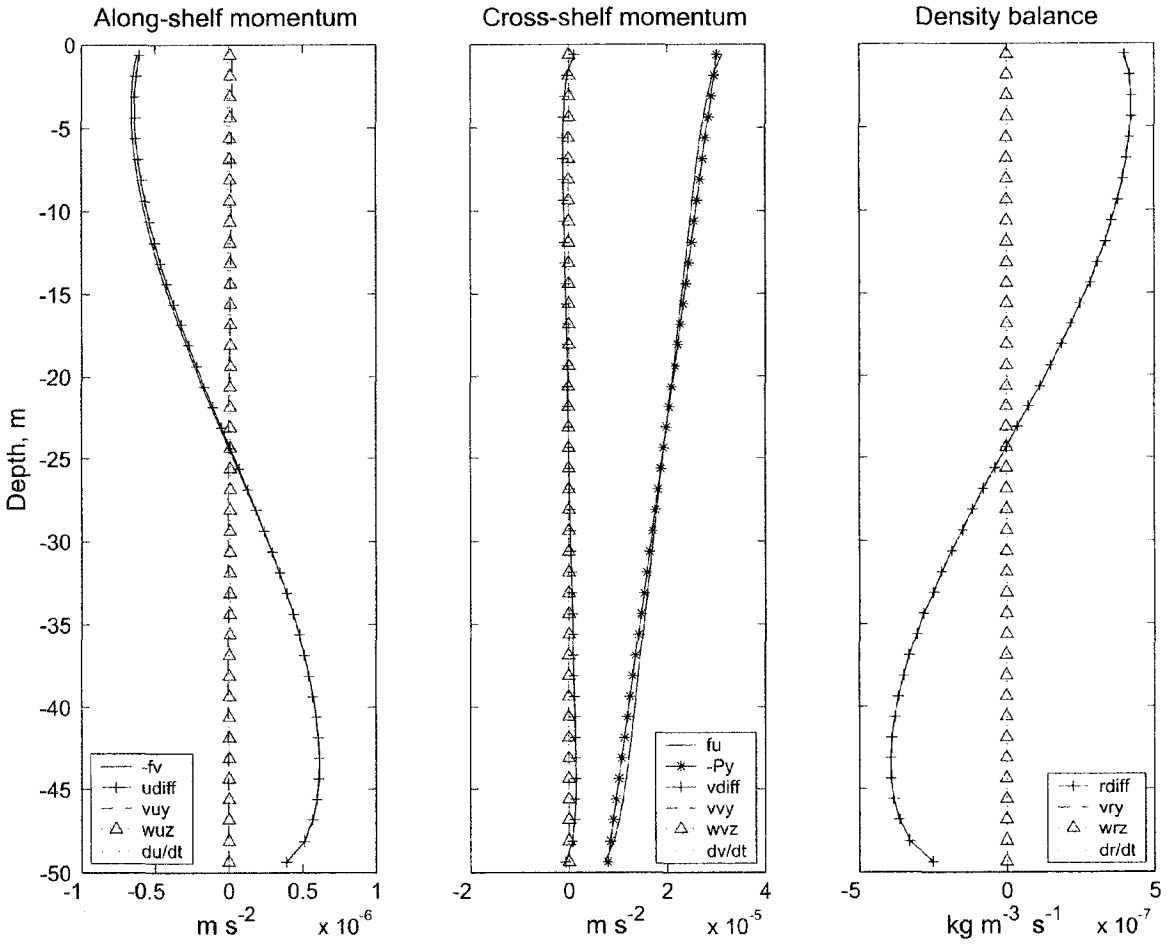

Figure 2.9: Vertical profiles of the terms in the momentum and density equations. The profiles are taken from middle of the density front ($y = 50\ km$) in the steady state numerical model run depicted in Figure 2.8. The dominant balances in the equations are the same as those used in the simpler analytical model, indicating the validity of the approximations used in the analytical model.

center of the front ($y = 50\ km$) for the model run depicted in Figure 2.8. For the range of parameters that produce a steady state in the numerical model, *Ro* and *l/L* are much less than 1, and justify the approximations used for the analytical steady-state model.

2.2.4.3 Cross-shelf transport within the surface boundary layer

The cross-shelf transport in the surface boundary layer V can be calculated by vertically integrating the along-shelf momentum equation (2.1) over the boundary layer. Contributions to this integral from u_t are ignored by assuming a steady state, and contributions from vu_y and wu_z are ignored through assuming a small Rossby number $Ro \ll 1$. This integration is the same procedure as for calculating Ekman transport and leads to:

$$V = \frac{1}{\rho_0 f}((A_V u_z)^{mid} - \tau^{wind}), \tag{2.18}$$

where $(A_V u_z)^{mid}$ is the along-shelf stress in the middle of the water column, preferably at a point just below the bottom of the surface boundary layer. In an Ekman layer calculation $(A_V u_z)^{mid}$ is taken to be zero but this cannot be done here. In the steady state illustrated in Figures 2.8 and 2.9, the surface and bottom boundary layers intersect and so a point outside the boundary layers cannot be found and A_V is a maximum at mid-depth.

Moreover, u_z^{mid} is not zero at mid depth both due to shear from the boundary layers and, within the front, due to the thermal wind balanced component of the flow. However, we find that stably stratified steady states occur within the front for model parameters that are near to those for which no boundary layers are required, so that the Ekman boundary layer flow is small in comparison to the thermal wind flow within the front. This means that $(A_V v_z)_{zz} \ll -b_y$ at mid-depth in the water column (see Figure 2.9)), whether or not the boundary layers fully intersect there, and that u_z is dominated by thermal wind shear at mid-depth. We therefore rewrite u_z in equation (2.19) using thermal wind shear to get

$$V = -\frac{A_V^{mid} b_y}{f^2} - \frac{\tau^{wind}}{\rho_0 f}. \tag{2.20}$$

This formula applies within the front. Away from the buoyancy front, where $b_y = 0$ and the shear at mid depth is dominated by the intersecting boundary layers, this formula does not apply and the reader is referred to *Lentz* [1995]. The magnitude and direction of the surface boundary layer within the front depends on the relative magnitudes of the surface wind-stress and the interior "thermal-wind" stress, which depends on both the thermal-wind shear and A_V^{mid}. Specifically, V is onshore if $A_V^{mid} < -\frac{\tau^{wind} f}{\rho_0 b_y}$, and offshore if $A_V^{mid} > -\frac{\tau^{wind} f}{\rho_0 b_y}$, which is the same result as the analytical model except that the eddy viscosity at mid-depth is used rather than a constant eddy-viscosity.

A separate estimate of A_V^{mid} can be made. In this model of downwelling wind-stress acting on a surface-to-bottom density front, the flow and density structure is determined by the parameters u_*, f, b_y, D and L, where $u_* = \sqrt{\frac{\tau}{\rho_0}}$ and b_y is the cross-shelf buoyancy gradient at the center of the front. In particular, the vertical eddy diffusivity must also be a function of these parameters and this is also true in the numerical model, where vertical eddy diffusivities are derived by the turbulence closure scheme and not independently chosen. The parameters that describe the turbulent closure scheme are ignored here by considering them to be fixed constants. In a similar way, we also exclude C_D and z_0 as variable parameters, considering them constants in the derivation of the bottom-stress from the overlying near bottom flow.

Following *Lentz* [1995] and *Austin* [1998], when the surface and bottom boundary layers intersect, the water column is neutrally stratified and the bottom stress is equal to the surface stress, the eddy diffusivity profile becomes parabolic so that

$$A_V = -\kappa u_* D \frac{z}{D}\left(1 + \frac{z}{D}\right). \tag{2.21}$$

This eddy diffusivity profile is constructed so that at the surface and bottom boundaries a log-layer is represented. Numerical results produced by ROMS using the Mellor-Yamada 2.5 mixing scheme closely match this profile at the center of the front, when the front is

vertical, despite the vertical shear in the water column being dominated by thermal wind balance rather than Ekman layer dynamics at this location.

Evaluating this expression at its maximum at mid-depth ($D/2$) gives a second estimate of A_V^{mid},

$$A_V^{mid} = \frac{\kappa u_* D}{4}. \tag{2.22}$$

Equating the two estimates gives

$$\frac{D}{\delta_*}\frac{|b_y|}{f^2} = \frac{4}{\kappa^2} \simeq 25, \tag{2.23}$$

where δ_* is the Ekman layer depth now defined as $\delta_* = \kappa u_* / f$. Note that $\frac{D}{\delta_*}$ is the ratio of the bottom depth to the Ekman layer depth and $\frac{|b_y|}{f^2}$ is the ratio of the thermal wind shear in the front to the Coriolis frequency. This equation is found to hold from the numerical modeling to within a factor of two. We find the front is vertical in the numerical model when

$$\frac{D}{\delta_*}\frac{|b_y|}{f^2} \simeq 50. \tag{2.24}$$

If $\frac{D}{\delta_*}\frac{|b_y|}{f^2} < 50$ the front is unstable everywhere and if $\frac{D}{\delta_*}\frac{|b_y|}{f^2} > 50$ the front becomes stable at its center. We emphasize that this result requires that the surface and bottom boundary layers intersect so that $\frac{D}{\delta_*} < 2$ is a necessary condition for the preceding results.

2.2.4.4 Angle of the front in steady state

The density balance that occurs in steady state is a balance between cross-shelf advection in the surface boundary layer and vertical diffusion. A vertical integral of this balance from the interior of the flow away from the boundary layer or mid depth to the surface gives

$$b_y V = K_V^{mid} b_z. \tag{2.25}$$

Using the cross shelf transport, V, given by equation (2.20), equation (2.25) can be rewritten as

$$\left.\frac{\partial y}{\partial z}\right|_b = -\frac{b_z}{b_y} = -\frac{V}{K_V} = \frac{b_y A_V^{mid}}{f^2 K_V^{mid}} + \frac{\tau^{wind}}{\rho_0 f K_V^{mid}}, \tag{2.26}$$

giving the slope of the isopycnals in the steady state at mid depth. Note that this slope is different from the estimates of the ratio of the horizontal scale to vertical scale of a front determined through diffusive arguments by *Garrett and Loder* [1981] to be $(N/f)(A_V/K_V)^{1/2}$, and also different from the scale N/f given by *Pedlosky* [1987] using vorticity arguments.

2.2.4.5 Oscillation of the front due to variable diffusivity

The steady results presented so far pertain to steep fronts where the surface and bottom boundary layers intersect and where the boundary layer flow within the front is slow in comparison to the thermal-wind balanced component of the along frontal flow. However, parameters that specify the numerical model can be chosen so that instead of a steady state, near-inertial oscillations occur within the front. These near inertial oscillations are due to a combination of the variable eddy-diffusivity produced by turbulent closure scheme, forcing by the wind-stress, and separation of the surface and bottom Ekman layers.

One such near-inertial oscillation is shown in Figure 2.10, where the parameters are identical to those in Figure 2.8 except that the depth has been increased to 100 m from 50 m to decrease the thickness of the surface and bottom Ekman layers relative to the

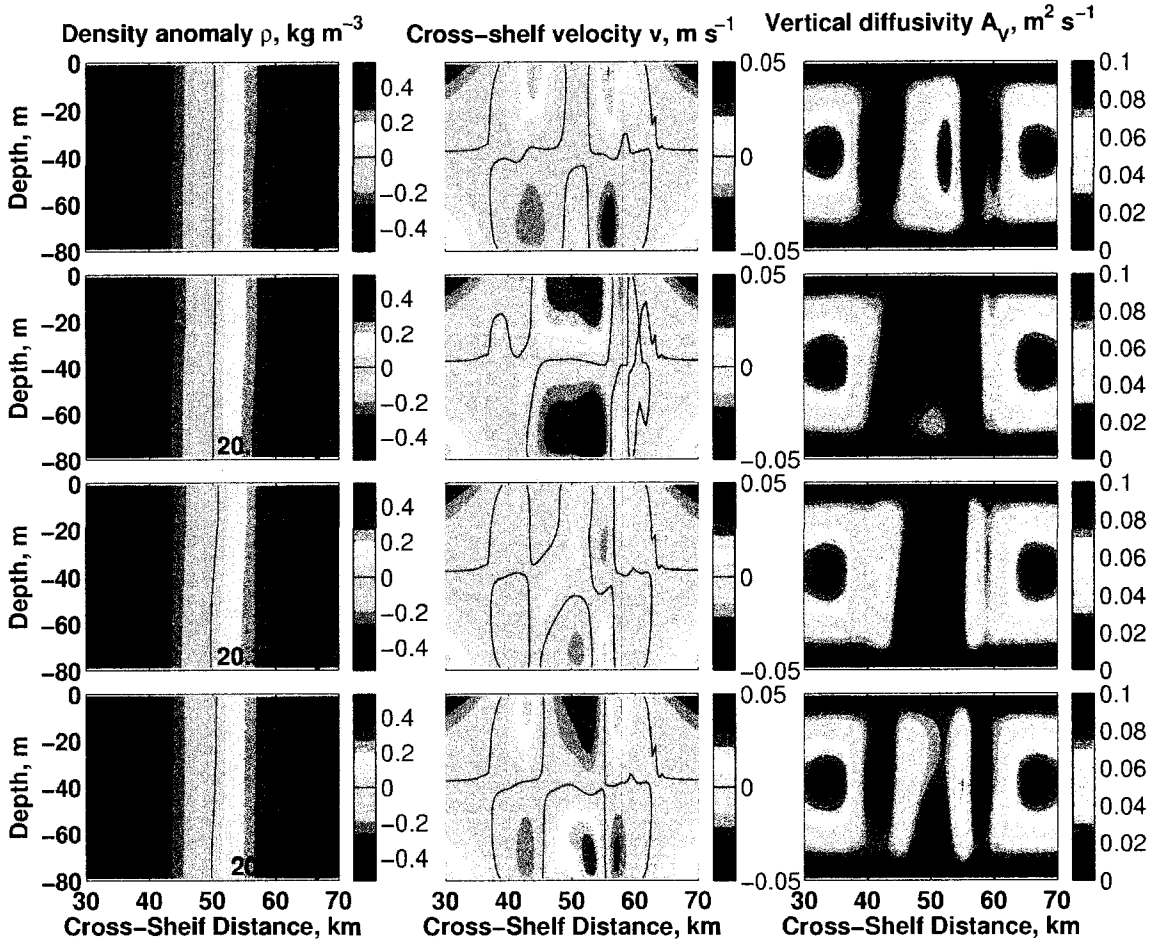

Figure 2.10: A sequence of figures showing a near inertial oscillation in the density front for a numerical model run. Parameters are identical to those for Figure 2.8 but the depth of the ocean is now 100 m rather than 50 m. The oscillation depends on inertial turning of the velocity vector combined with the strong variation of the modeled eddy diffusivity with Richardson number. The energy for the oscillation is ultimately provided by the wind-stress.

depth of the ocean. An oscillation of frequency $\sim 1.25f$ is present within the front, where a steady state similar to the $50\ m$ deep model run might be expected.

The oscillation proceeds as follows. At $t = 20\ days$ cross-shelf flow within the surface and bottom boundary layers at the center of the front is slow and the isopycnals are nearly vertical. The vertical diffusivity is high due to the low stratification and high vertical shear in the along-shelf flow. This shear creates an alongshore stress in the water column that is greater than the wind-stress implying Ekman transport offshore (see equation (2.20)). The oscillation now begins both through the inertial turning of the oscillatory velocity vector offshore and the offshore-directed Ekman transport. At $t = 20.15\ days$ there is strong offshore flow in the surface boundary layer and onshore flow in the bottom boundary layer. The isopycnals are steep but stable and the vertical diffusivity throughout the water column is small. Low-background vertical diffusivity at mid-depth gives little frictional coupling between the surface and bottom boundary layers and the boundary layers are separate. The oscillatory part of the flow within the front is now subject to inertial turning and the downwelling wind-stress. At $t = 20.35\ days$ the offshore flow in the surface boundary layer has slowed, as the velocity vector associated with the oscillation rotates anticyclonically to the downwind direction, and the density field at the surface reaches its maximum offshore position. The velocity vector then continues to rotate onshore (see $t = 20.5\ days$) and the density field at the surface is advected onshore. The vertical diffusivities within the front are increasing at this point as

the front steepens. Eventually the front returns to a state similar to that at $t = 20$ *days* and the oscillation begins again.

This type of oscillation is rather unusual due to its dependence on the vertical shear and buoyancy frequency dependent vertical diffusivity calculated by the turbulent closure scheme. In Figure 2.10, the Mellor-Yamada level 2.5 turbulent closure scheme is used, but the oscillation is not dependent on this particular scheme; qualitatively similar results are produced when using the *Pacanowski and Philander* [1981] and the *Large et al.* [1994] mixing schemes. For constant A_V and K_V a steady state is reached, the oscillations do not occur, and vertical diffusion of buoyancy within the front is balanced by the horizontal advection of buoyancy in the boundary layers. If this steady state is perturbed so that the offshore velocity in the surface boundary layer, the onshore velocity in the bottom boundary layer and $\frac{\partial \rho}{\partial z}$ are all increased, $K_V \frac{\partial \rho}{\partial z}$ also increases, which balances the increased horizontal advection in the boundary layers. In the oscillatory case, with A_V and K_V strongly depending on the gradient Richardson number, $K_V \frac{\partial \rho}{\partial z}$ sharply decreases during such a perturbation and the increased advection in the boundary layers is not balanced by increased vertical diffusion and an oscillation results.

The differing model response to 50 m and 100 m water columns is solely because the boundary layers overlap in the former but not in the latter. The first example given above is for a 50 m deep model run and a steady state results. On changing the depth to 100 m

an oscillation results. In the deeper model run the Ekman layer depth is smaller relative to the water column depth and the surface and bottom boundary layers separate as the front becomes more stable during the oscillation. The oscillation can be viewed as due to this separation of the boundary layers from each other.

The conditions under which the numerical model is unstable and convecting, stable and steady or stable and oscillatory can be organized by considering D/δ_* and b_y/f^2. From section 2.2.4.3, if $Db_y/\delta_* f^2 \approx 50$ and D/δ_* is small enough that the boundary layers intersect, then the front is vertical. Decreasing either D/δ_* or b_y/f^2 from this point causes the front to become statically unstable and convecting everywhere. Increasing either D/δ_* or b_y/f^2 from this point first causes the front to become steady and stable then, if either D/δ_* or b_y/f^2 are increased further, causes the near inertial oscillations to occur in the front due to separation of the boundary layers. Increasing D/δ_* directly causes separation of the surface and bottom boundary layers, whereas increasing b_y/f^2 does so indirectly. An increase in b_y/f^2 tends to make the front less steep, which means that b_z increases. The increase in stratification at mid depth tends to reduce the value of the vertical eddy diffusivity there and so leads to separation of the boundary layers.

For smaller values of b_y/f^2, $D/\delta_* > 2$ when $Db_y/\delta_* f^2 \approx 50$. In this case, since the boundary layers are separate, the vertical eddy diffusivity at mid depth only depends on

the thermal wind balanced component of the flow. When the front is vertical and steady it depends only on the shear due to thermal wind. This shear becomes smaller as b_y / f^2 is reduced. In this case the wind stress cannot be balanced by the stress at mid depth and the front becomes convecting.

2.2.4.6 Relaxation of the front

On cessation of the downwelling wind-stress, there is little relaxation of the steep isopycnals towards the horizontal. As the front adjusts, the high vertical eddy diffusivities, onshore/offshore transports in the boundary layers, and alongshore transport due to the wind eventually decay, leaving the front essentially in thermal wind-balance with the level of no motion at the bottom. There are still small cross front flows that satisfy the upper and lower stress boundary conditions and the stresses due to the background vertical eddy diffusivity. This adjustment is essentially the same as that described in the 2-dimensional studies of *Austin and Lentz* [2002] and *Allen and Newberger* [1996]. The thermal wind balance persists since there is no bottom friction due to no flow at the bottom (a mechanism similar to *Chapman et al.* [1988]) and only background vertical eddy diffusivity in the water column.

The adjustment of the front from the downwelling wind-stress forced flow to no-wind-stress and a level of no motion at the bottom initially tends to include the near inertial

oscillations that are described above, the decaying bottom friction acting as a surrogate to the wind-stress for the oscillation. These oscillations eventually decay, leaving a thermal wind balanced front with a level of no motion at the bottom. Note also that if the adjustment of the front to the downwelling wind-stress causes the potential vorticity (as defined in the next section) to be greater than zero, then symmetric instabilities are also present during the relaxation. These cause the front to slowly tilt towards the horizontal until the PV is less than zero, when the symmetric instabilities decay.

2.2.4.7 Symmetric instability

An Eady-type problem [*Eady*, 1949], where instabilities are sought in a thermal-wind balanced basic state with uniform horizontal and vertical buoyancy gradients, can exhibit baroclinic, Kelvin-Helmholtz and symmetric instabilities [*Stone*, 1966]. The fastest growing instability depends on the value of the potential vorticity or equivalently the gradient Richardson number [*Stone*, 1966; *Stone*, 1970]. In the 2-dimensional modeling presented here, the bulk effect of Kelvin-Helmholtz instabilities is represented by the vertical eddy diffusivities, and baroclinic instability is suppressed because it requires alongshore variation. This leaves symmetric instability as the only possibility. Symmetric instability can occur when the isopycnals are steep enough so that the potential vorticity Π, as defined by

$$\Pi = \left(f - \frac{g\rho_{yy}}{f\rho_0}(D-z) \right)\rho_z + \frac{g(\rho_y)^2}{f\rho_0}, \tag{2.27}$$

is greater than zero. Fully-developed, non-linear symmetric instabilities in an Eady-like problem are considered using a numerical model with constant vertical Eddy-diffusivity by *Walton* [1975]. The modeling presented here exhibits symmetric instability very similar to that described by *Walton* [1975] when $\Pi > 0$. For this case, the vertical eddy diffusivity is small enough that symmetric instability is not suppressed [*Walton*, 1975], and the flow does not contain the near inertial oscillations that are described above. This situation can occur for very small wind-stress and during the relaxation of the front after the wind-stress is switched off. The symmetric instability is most organized and similar to that described by *Walton* [1975] when the numerical model is run with constant eddy diffusivity.

2.2.4.8 Sloping bottom topography

Several numerical experiments were performed with a sloping bottom. This had little quantitative effect on the flow. In these experiments the value of D/δ_* had a small variation across the front that was not large enough to change the character of the flow across the front from that expected for a constant depth ocean. However, a front wide enough to have a large depth change over its width would be expected to be steady or convecting towards its shallow, inshore edge and oscillatory towards its deeper outside

edge under the right conditions. The sloping bottom case was not considered in detail since the cross-shelf flows within the front, in this modeling, are not driven by the bottom boundary layer.

2.3 Introduction of fresh water at the coast

A more realistic 2-dimensional model can be obtained by modeling the coastal inflow of buoyant water that causes the ACC rather than initializing the model with a density front that mimics the ACC. A schematic of this situation is shown in Figure 2.11. By modeling the ACC in this 2-dimensional fashion, we approximate the coastal freshwater input to the Gulf of Alaska as an infinite distributed line-source.

Little is known about the actual spatial distribution of runoff into the Gulf of Alaska [*Royer*, 1982]. Although there are several large point source inflows, which clearly do not fit into the distributed runoff scenario, there are numerous smaller streams that plunge directly into the ocean from steep-sided coastal mountains. We approximate the average effect of freshwater input into the Gulf of Alaska by the use of line-source inflows, such as have been used in previous 2-dimensional studies by *Chao* [1987], *Kao* [1980], *Kao* [1981b] and *Kao et al.* [1978].

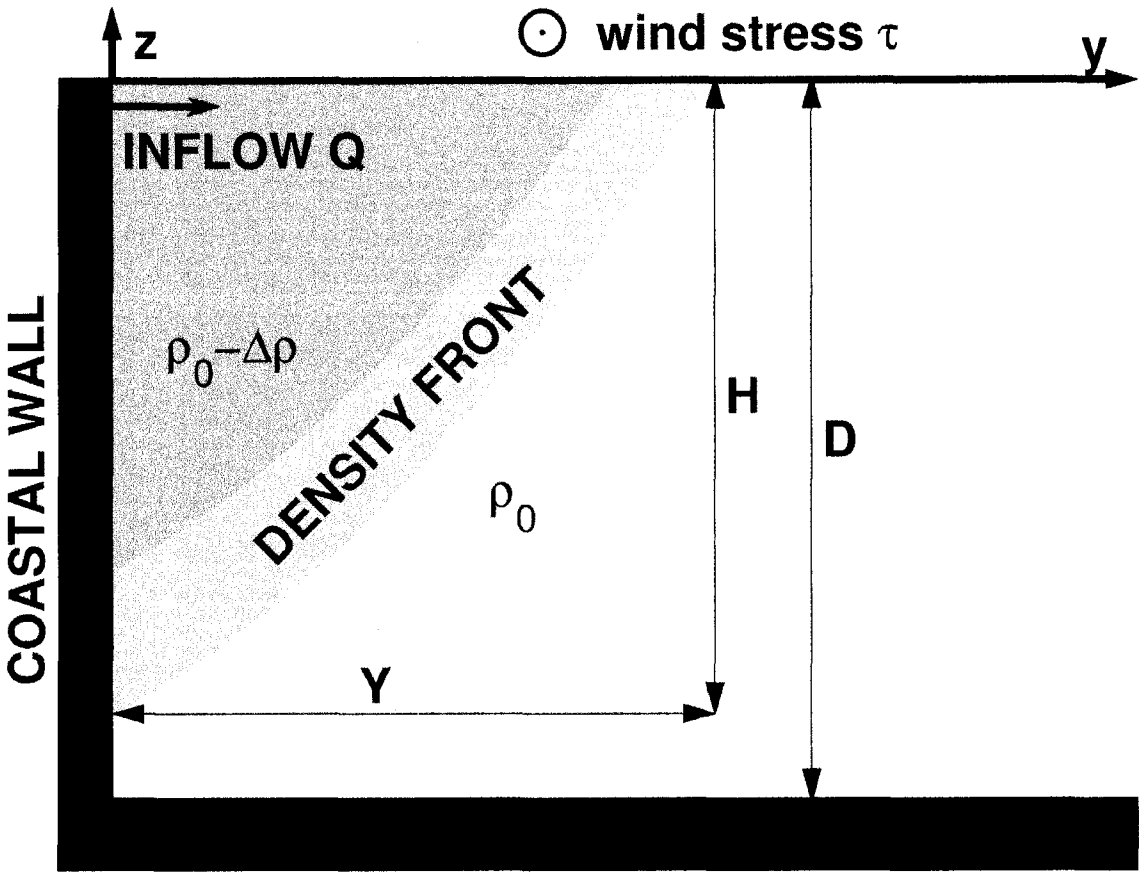

Figure 2.11: A schematic of the model used to study a line-source of buoyant inflow at the coast. A cross-shelf slice through the resulting coastal current is depicted with light water against the coast and dense water offshore. The width of the current is Y, the depth of the current at the coast is H, and the depth of the ocean is D. The coordinates are z positive upward, y positive offshore, and x increasing along-shore towards the reader.

Although there are many ways to introduce buoyant water at the coast, all are rather unrealistic in some way. In the numerical modeling presented here, buoyant water is introduced at the surface grid point. The inflow has density deficit $\Delta\rho$ and is directed offshore, so the along-shore inflow velocity $u_I = 0$ and the cross-shore inflow velocity $v_I = Q/\Delta z$, where Q is the volume inflow rate and Δz is the thickness associated with the surface grid point. The inflow density is not that of freshwater but is assumed to have undergone some mixing with seawater prior to reaching the coast and is modeled to have the maximum density deficit observed within the ACC for the season being studied. The inflow rate Q is then artificially increased so that the freshwater input Q_f into the modeled Gulf of Alaska is correct following the estimates by *Royer* [1982] shown in Figure 2.1. This gives

$$Q = \left(\frac{\rho_s - \rho_f}{\rho_s - \rho_I}\right) Q_f \tag{2.28}$$

where ρ_f, ρ_I and ρ_s are the densities of freshwater, the inflowing water and ambient seawater respectively. The only way to model both inflow volume and buoyancy input correctly is to input the correct volume of freshwater. This produces a huge density difference at the coast unless the inflowing freshwater is allowed to mix with the ambient water by wind mixing or in an estuary or fjord in the numerical model. Modeling an estuary is possible for a line-source but not presented here for simplicity.

For the method of inflow used, the correct velocity v_I and depth H_I of the inflow water is that of a surface gravity current

$$v_I = (2g'Q)^{1/3},$$
$$H_I = \left(\frac{Q^2}{2g'}\right)^{1/3}, \tag{2.29}$$

so that $v_I = \sqrt{2g'H_I}$ [*Benjamin*, 1968]. If the depth of the inflow is specified to be greater than the gravity-current depth the inflow quickly thins until the gravity current depth is reached. This produces strong upward vertical velocities at the coast that cause an artificial, cross-shelf, vertical circulation cell within the resulting coastal current. Alternatively, the depth of the inflow can be specified to be less than the gravity-current depth. In this case, the inflow quickly thickens until the gravity-current depth is reached and no erroneous large-scale circulation occurs. The coastal current essentially develops as if the depth of the inflowing buoyant water was correct. In the numerical model, the inflow depth is the thickness of the surface grid point, so it cannot become thinner and is also always less than the gravity current depth H_I.

2.3.1 Coastal boundary condition

Sigma coordinate models have a constant number of grid points in the vertical producing higher vertical resolution in shallow coastal areas. As the depth tends towards zero at the coast the vertical resolution tends to infinity, causing the time step required for model

stability to tend to zero. It is therefore necessary to limit the minimum depth at the coast with an artificial coastal wall. Water depth generally increases rapidly seaward of the coast in the Gulf of Alaska often being $\sim 50m$ deep within $1km$ offshore (see bottom topography of the Cape Fairfield section in Figure 2.3). The horizontal resolution of the numerical model is typically $0.5-1km$ and so a coastal wall of $\geq 50m$ depth is used and the steep shoaling to the coast is not resolved.

The boundary condition on the coastal wall can be specified to be either free-slip, semi-slip or no-slip. Free-slip implies no sidewall friction and is written $u_y = 0$ at $y = 0$, no-slip implies no flow at the coast and is written $u = 0$ at $y = 0$, and semi-slip is half-way between the two. Results using the free-slip condition are qualitatively different from those using the no-slip or a semi-slip boundary condition (see Figure 2.12). The free-slip condition tends to produce a narrow deep coastal current with the maximum along-shelf velocity at the coast whereas the no-slip and semi-slip boundary conditions lead to a shallower wider current with maximum along-shelf velocity at the current's offshore edge. In both cases, the offshore directed inflow turns inertially causing acceleration of the along-shore flow over a distance of one inertial radius from the coast. The free-slip boundary condition puts the along-shore flow at the coast equal that just offshore and this causes the maximum alongshore flow at the coast. The no-slip boundary condition has zero alongshore flow at the coast producing strong cross-shelf shear in the alongshore velocity. This shear is then advected offshore causing the highest alongshore velocities at

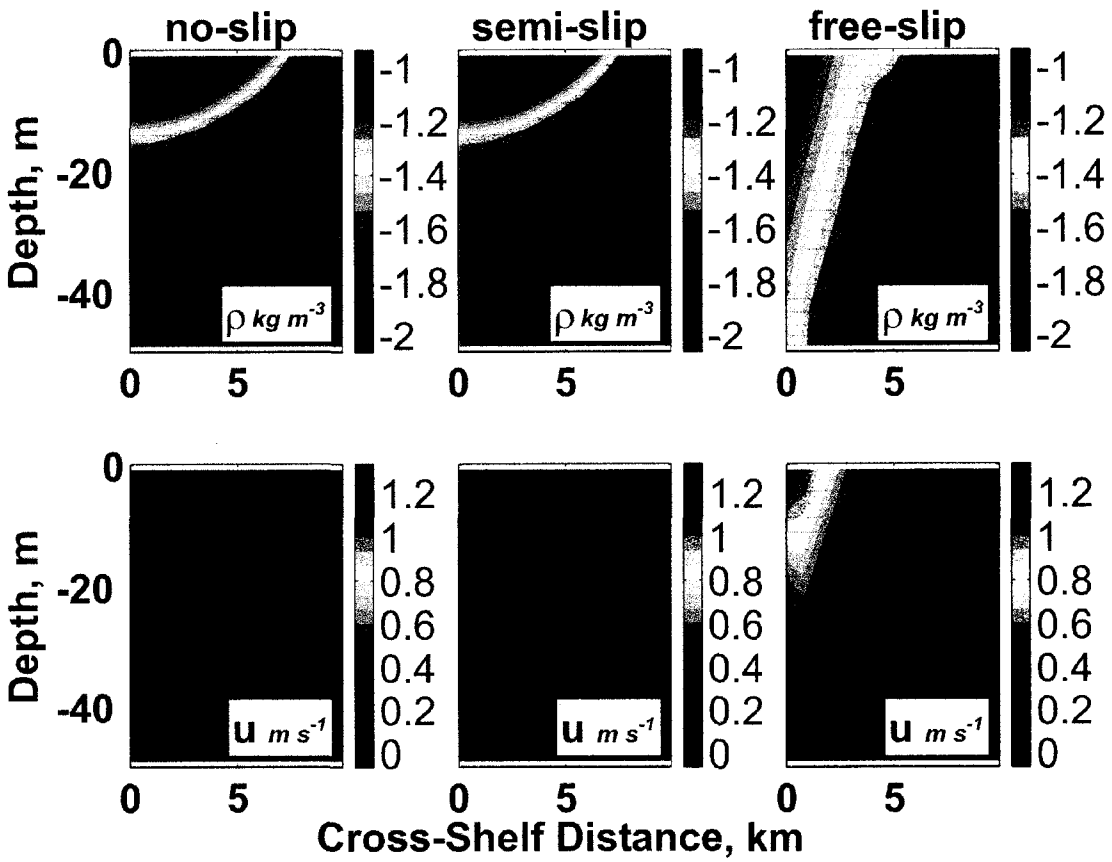

Figure 2.12: Results from numerical models of line source inflow using different side-wall slip conditions for the along-shelf velocity *u*. The no-slip, and semi-slip conditions are functionally identical, both producing no flow at the coast, maximum along-shore velocity at the outer edge of the current and near zero absolute vorticity in the buoyant layer. The free-slip boundary condition produces a narrow-deep current with maximum along-shore velocity at the coast.

the edge of the current. Assuming the inflow turns in an inertial circle, the relative vorticity ζ of the flow at the coast can be estimated by

$$\zeta = - \frac{v_{inflow}}{inertial\ radius} = - \frac{v_{inflow}}{v_{inflow} / f} = -f \qquad (2.30)$$

which leads to zero absolute vorticity ($= f + \zeta$) and so zero potential vorticity also.

The no-slip boundary condition is used in this study over the free-slip condition since it produces an offshore maximum in the along-shelf velocity which is more typical of the ACC [*Johnson et al.*, 1988] and other coastal currents such as the Delaware coastal current [*Muenchow and Garvine*, 1993a]. It is also the coastal boundary condition used in *Kao* [1980], *Kao* [1981b] and *Kao et al.* [1978]. The semi-slip condition could have been used since it also leads to no flow at the coast in this case.

2.3.2 Zero potential vorticity 1½-layer model

Before presenting the results of the line-source inflow in the numerical model it is instructive to consider the development of the line-source analytically using a zero potential vorticity 1½-layer model. The active layer in this 1½-layer model is the buoyant

inflow water and the motionless, infinitely-deep layer is ambient shelf water. Since there is no vertical shear in the upper layer flow the inflowing buoyant water is now introduced uniformly over the depth of the buoyant layer at the coast. The 2-dimensional model studied here implies along-shelf scales large relative to cross-shelf scales (a long-wave approximation) so that the cross-shelf momentum has geostrophic balance. The momentum and continuity equations with no variation in the along-shelf direction are

$$\begin{aligned} u &= -\frac{g'}{f}h_y && \text{(cross-shelf momentum)}, \\ u_t + vu_y - fv &= 0 && \text{(along-shelf momentum)}, \\ h_t + (vh)_y &= 0 && \text{(continuity)}, \end{aligned} \tag{2.31}$$

where subscripts denote partial differentiation and h is the depth of the buoyant layer. Using the cross-shelf geostrophic balance, the along-shelf momentum equation can be rewritten so that the governing equations are

$$\begin{aligned} h_{yt} + (h_{yy} + f^2/g')v &= 0 && \text{(along-shelf momentum)}, \\ h_t + (vh)_y &= 0 && \text{(continuity)}, \end{aligned} \tag{2.32}$$

from which the statement of conservation of potential vorticity can be formed

$$\frac{d}{dt}\left(\frac{h_{yy} + f^2/g'}{h}\right) = 0. \tag{2.33}$$

Applying a boundary condition at the coast of $u = c$ at $y = 0$ for all t where c is a constant, the along-shelf momentum equation, evaluated at $y = 0$ becomes

$$h_{yy} + f^2 / g' = 0, \tag{2.34}$$

and the inflowing water has zero potential vorticity. All buoyant water in the upper layer flows through the coast and so boundary conditions of this type imply that all water in the buoyant layer has zero potential vorticity. Equation (2.34) applies everywhere, so that the along-shelf momentum balance is between the Coriolis term $(-fv)$ and cross-shelf advection (vu_y) as found in *Kao* [1981a].

Solving equation (2.34) using boundary conditions of $h_y = 0$ at $y = 0$ (no along-shelf flow at the coast i.e. no-slip) and $h = 0$ at $y = Y$ (zero depth to the coastal current at the current's offshore edge) we get the self-similar solution

$$\frac{h}{H(t)} = 1 - \left(\frac{y}{Y(t)} \right)^2, \tag{2.35}$$

where $Y(t)$ is the width of the coastal current and $H(t) = \frac{f^2}{2g'}Y(t)^2$ is the depth of the coastal current at the coast. As buoyant water flows into the model domain the coastal current both widens and deepens. Integrating the continuity equation from the coast to the edge of the current gives

$$\frac{\partial Y^3}{\partial t} = \frac{3g'Q}{f^2}. \tag{2.36}$$

Integrating this in time and using $Y = 0$ at $t = 0$ gives

$$\begin{aligned} Y &= 3^{1/3}\left(\frac{g'Q}{f^2}\right)^{1/3} t^{1/3}, \\ H &= \frac{3^{2/3}}{2}\left(\frac{f^2Q^2}{g'}\right)^{1/3} t^{2/3}, \end{aligned} \tag{2.37}$$

which differs from the scales for Y and H asserted in *Griffiths and Linden* [1981] that give $(Y,H) \propto t^{1/2}$ but are essentially the same scales as found by *Kao* [1980]. Several interesting features follow from the 1½ layer solution. First, as the coastal current widens it becomes proportionally deeper,

$$\frac{H}{Y} = \frac{3^{1/3}}{2}\left(\frac{f^4Q}{g'^2}\right)^{1/3} t^{1/3}. \tag{2.38}$$

Second, the bulk Froude number of the coastal current remains constant,

$$Fr = \frac{\sqrt{g'H}}{fY} = \frac{1}{\sqrt{2}}, \tag{2.39}$$

so that the width of the coastal current is always $\sqrt{2}$ times the Rossby radius of deformation and the maximum along-shelf velocity is $\sqrt{2}$ times the internal gravity wave speed. Third, the bulk Richardson number Ri_B is

$$\mathrm{Ri_B} = \frac{1}{2}\left(\frac{Y^2}{y^2} - 1\right). \tag{2.40}$$

The last statement indicates that $Ri_B < 0.65$ for $y > 0.66Y$ or about the outer $1/3$ of the current, so vertical mixing would be expected between the layers of the 1½-layer model if the model admitted mixing processes [*Price et al.*, 1986].

2.3.3 Numerical model

Using ROMS, a suite of line-source, numerical model runs were performed covering the range of inflow parameters relevant to the ACC. The inflow was implemented as described above, a no-slip boundary condition was used at the coastal wall, there was no

explicit horizontal mixing, and the Mellor-Yamada level 2.5 sub-model was used for vertical mixing. These numerical models are similar to those performed in *Kao* [1981b] which used constant vertical diffusivity rather than a turbulent closure scheme and did not consider zero potential vorticity. The results of one such model run are shown in Figure 2.13 after 7.5 *days* of inflow. The numerical model agrees exceedingly well with the 1½-layer model, which is shown in the figure by a thick black line. A least squares fit of the middle of the density front in the numerical model runs to a quadratic gives, when averaging over all line source model runs performed,

$$
\begin{aligned}
Y &\simeq 1.45\left(\frac{g'Q}{f^2}\right)^{1/3}(t-t_Y)^{1/3}, \\
H &\simeq 1.02\left(\frac{Q^2f^2}{g'}\right)^{1/3}(t-t_H)^{2/3}, \\
\frac{h}{H} &\simeq 1.00+0.08\frac{y}{Y}-1.08\left(\frac{y}{Y}\right)^2,
\end{aligned}
\tag{2.41}
$$

where t_Y and t_H are offsets in time of magnitude less than 2 inertial days. They are presumably due to vigorous mixing of the buoyant source water with the ambient water when the source is switched on. This good agreement of the numerical model with the 1½-layer analytical model is expected, because the vertically integrated 1½-layer equations can be obtained from the full momentum equations used in the numerical model by vertically integrating over the buoyant water layer and excluding the effects of mixing.

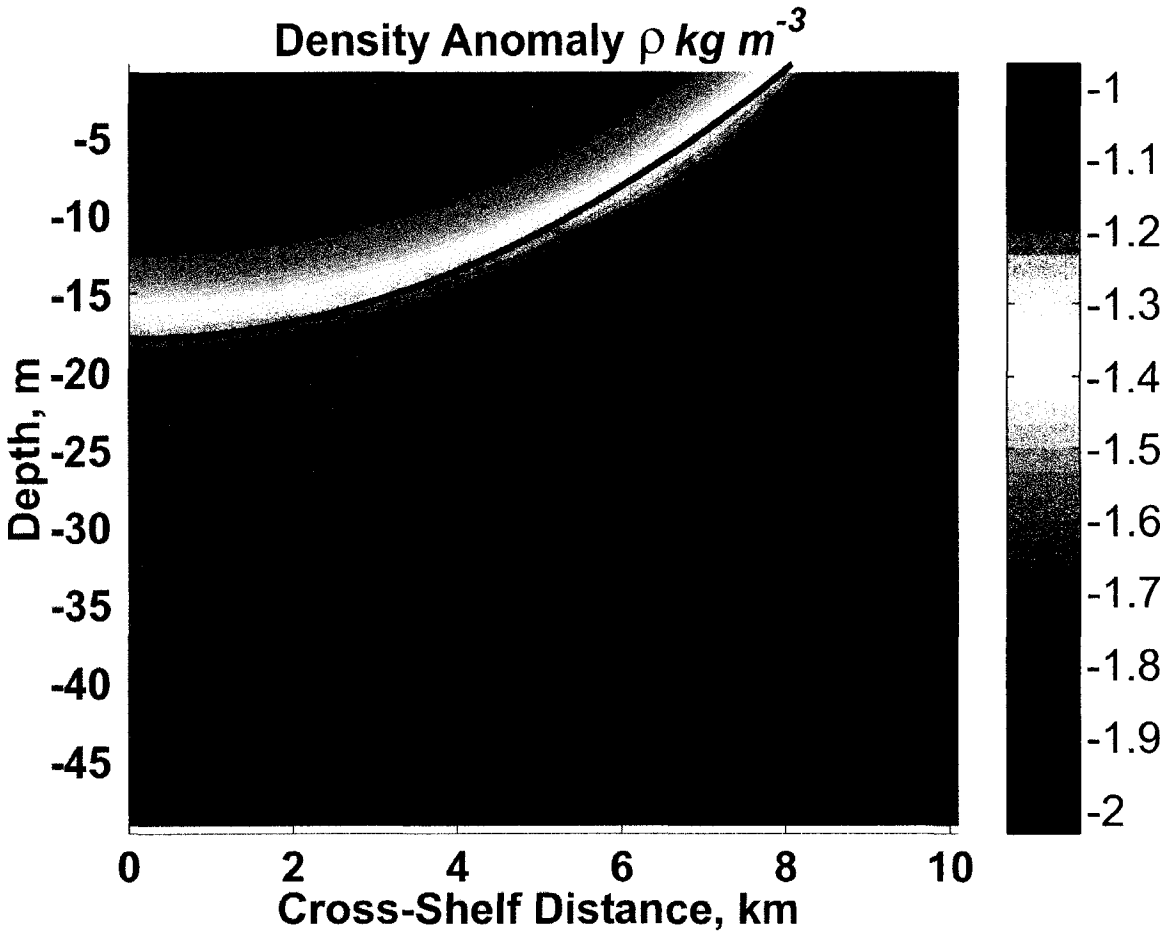

Figure 2.13: A comparison of the numerical, line-source model after 7.5 days of inflow with the analytical 1½-layer model. The density anomaly of the numerical model is contoured and the thick black line shows the analytical model.

Eventually, in the numerical model, the depth of the coastal current at the coast approaches the depth of the model domain. The depth of the coastal current in the 1½-layer model equals the depth of the model domain when $H = D$ or

$$t = \frac{2^{3/2}}{3}\frac{(g')^{1/2}}{fQ_I}D^{3/2}. \tag{2.42}$$

For the ACC this time scale is on the order of 1 month. As this point is approached, the 1½-layer model ceases to apply, since the lower layer cannot now be considered infinitely deep, and a full 2-layer model is more appropriate. When the base of the coastal current intersects the bottom the rate of offshore spreading of the coastal current changes so that $W_t = \frac{Q_I}{D}$. Essentially the structure of the front marking the off-shore boundary of the coastal current now remains constant, but it has a slow offshore motion as it is "pushed" offshore by the inflowing buoyant water so that the 'continental shelf' in the numerical model slowly (and unrealistically) fills up with buoyant water. As the front is pushed offshore the near inertial oscillations are again present in the front.

2.3.4 Effect of downwelling wind-stress

Applying downwelling wind-stress to the case of buoyant inflow at the coast causes the front to steepen, and then become bottom attached if it is not bottom attached already.

The front is then pushed offshore by the inflowing buoyant water, as described above. Within the front the flow is nearly identical to that described by the no-inflow downwelling wind-stress case.

2.4 Discussion and conclusions

A coastal buoyancy front subjected to downwelling wind-stress shows steady and convecting, steady and stable, and oscillatory flow patterns depending on the values of ratio of the bottom depth to the Ekman layer depth, and the ratio of the along-shelf thermal wind shear to the Coriolis frequency. In the steady convecting and stable cases the basic buoyancy balance is between cross-shelf advection and vertical diffusion. In the oscillatory case vertical diffusion is less important, the buoyancy field mostly being advected with the oscillatory flow. In all cases the buoyancy field is steady, or quasi steady for the oscillatory case, so that the concentration of a tracer with isopleths coincident to isopycnals would not change significantly due to frontal flows associated with downwelling wind-stress.

Nitrate is a biologically active tracer that tends to be strongly related to salinity (and therefore density or buoyancy) below 100 m in the Gulf of Alaska [*Childers*, 2001]. This nutrient, which may be limiting to new biological production on the Gulf of Alaska shelf, can be depleted in the surface waters in the Gulf of Alaska due to primary production

[*Childers*, 2001]. Therefore, in surface waters nitrate isopleths no longer coincide with isopycnals. In this case, the vertical diffusion of density within the front would result in a flux of nitrate from the bottom of the Gulf of Alaska shelf to the surface. However, two caveats need to be stated. Firstly, the Gulf of Alaska shelf is approximately 150 to $200\,m$ deep and the mean wind stress in winter is $\sim 0.1\,Pa$. This means that were the 2-dimensional models to apply, the front associated with the ACC would be oscillatory and therefore there would be less vertical diffusion within the front, though the convecting margins of the front would be effective at vertical nitrate transport. Secondly, in CTD sections across the ACC taken as part of the GLOBEC long-term observation project the front is never fully vertical, even in winter when there is strong mean downwelling wind-stress, suggesting that 2-dimensional dynamics may not adequately describe the ACC.

Cross-frontal flows associated with the ACC would vary depending on whether the flow is convecting, stable or oscillatory. In the convecting case the boundary layers do not change direction within the front, so that, for example, tracers in the surface boundary layer can be advected onshore across the front while also diffused vertically within the front. When the front is steady and stable or oscillatory the boundary layers within the front form a separate circulation to the flows outside of the front. In this case tracers offshore and in the surface boundary layer can no longer be advected onshore across the front.

Cross frontal convergences and divergences are produced by the cross-frontal flows. Regions of convergence are pertinent to the ecosystem since they tend to lead to concentrations of upward swimming plankton near the surface [*Epstein and Beardsley*, 2001] and so may aggregate prey for foraging fish and seabirds.

In all model runs with downwelling wind-stress the margins of the front, having low values of b_y / f^2, are convecting whether or not the center of the front is convecting also. Convection is a non-hydrostatic process, so in hydrostatic models convection is typically represented by either instantaneous vertical mixing to remove density inversions, or by allowing large values of the eddy diffusivities that represent the rate at which vertical mixing would occur during convection [*Pringle*, 2001]. There are two points of justification for making this approximation. One is that convective processes generally occur on timescales that are short in comparison to the inertial timescale and so occur faster than the processes of interest in our model. The second is that the width of a convection cell is generally on the order of the bottom depth so that, at least over the shelf, the spatial resolution of a numerical model is generally not great enough to resolve convection and so it must be parameterized. Both of these justifications can fail in the modeling presented above. When the isopycnals are close to vertical, convection can be so weak and slow that it can be expected to be affected by rotation, and in resolving a narrow front we may be close to the resolution required to resolve convection. From these considerations we anticipate that the modeling presented here is largely correct, although the flow details might change using a non-hydrostatic model. Studies using a

non-hydrostatic model, such as that employed by *Straneo et al.* [2002] to study wind-modified convection at the margins of the Labrador Sea, should be considered in the future.

The 2-dimensional modeling of a coastal current, as presented here, uses a cross-shelf slice as the model domain and introduces freshwater at the coast as an infinite line-source. While instructive, this modeling does not adequately represent the coastal ocean over seasonal time-scales, since there is no mechanism by which to remove buoyancy from the model and a realistic steady state cannot be achieved. The buoyant water introduced at the coast slowly fills the entire model domain, eventually causing the coastal current to become as wide as the shelf. In a model similar to this one, *Kao* [1981b] mitigated this effect by enhancing the horizontal diffusivity, effectively parameterizing the cross-shelf mixing due to eddies over the shelf. This produced a horizontal buoyancy gradient that is as wide as the shelf after 14 inertial days (see their Figure 4), but a steady state still cannot be formed since horizontal diffusion continues to broaden the front. This eventually reduces the cross-shelf flux of buoyancy within the front to less than the rate of influx of buoyancy at the coast. The only plausible way to counter this weakening effect of cross-shelf diffusion over time would be to continually relax the buoyancy at the offshore edge of the model domain back to oceanic values so that buoyancy is effectively lost at the shelf-break and the buoyancy gradient across the shelf is maintained. This approach is possible in the 2-dimensional cross-shelf slice when horizontal diffusion is used to mimic eddying motions. However, in this study, horizontal

diffusion is kept as small as possible so as not to obscure the dynamics of the coastal current.

The best way to include the effects of eddying motions is to model them explicitly. This can be done by extending the 2-dimensional cross-shelf slice in the along-shelf direction to form a three dimensional model that is periodic in the along-shelf direction. Preliminary numerical modeling using this model domain shows that the coastal current is baroclinically unstable under both the conditions of downwelling wind stress and no-wind-stress. The case of no-wind-stress has been described before in rotating tank experiments by *Griffiths and Linden* [1981] . However, although cross-shelf mixing occurs in their model due to the eddying motions that grow out of baroclinic instability, the 3-d along-shelf periodic model domain still suffers from the same problem as the 2-d model: the model domain eventually fills up with buoyant water despite cross-shelf mixing unless buoyancy is forced to disappear at the shelf-break. For this reason a detailed study of the along-shelf periodic model domain was not made.

The process that is ignored by both along-shelf periodic and 2-d model domains is along-shelf advection. In these models the buoyancy contained in the model domain is equal to the amount of buoyancy put in at the coast since the inflow began. However, a geostrophic along-shelf flow occurs in these models due to the cross-shelf buoyancy gradient that is not directly constrained by the amount of buoyancy input at the coast. In the following chapter, a fully three-dimensional model domain is used in which along-

shelf advective processes constrain the buoyancy flux across the shelf and buoyancy flows out of the model domain at the downstream end.

3. Idealized 3-dimensional modeling of the Alaska Coastal Current

3.1 A simplified model

A simplified 3-dimensional model of the Gulf of Alaska is presented here to isolate the dynamics of the Alaska Coastal Current that are solely due to the freshwater discharge from the coast and the downwelling wind-stress due to the storms in the region. For this reason the model has a straight coastline, ignoring the many fjords, capes and islands of the Gulf of Alaska, and uniform along-shelf bottom topography, ignoring the numerous banks on the shelf, canyons that cross the shelf and the alongshore variation in shelf width (see Figures 2.2 and 2.3).

The coastal freshwater discharge is also simplified to be a uniform half-line source of buoyant water (Figure 3.1). The distribution of freshwater discharge into the Gulf of Alaska is not well known, but has been viewed as a line-source due to numerous small

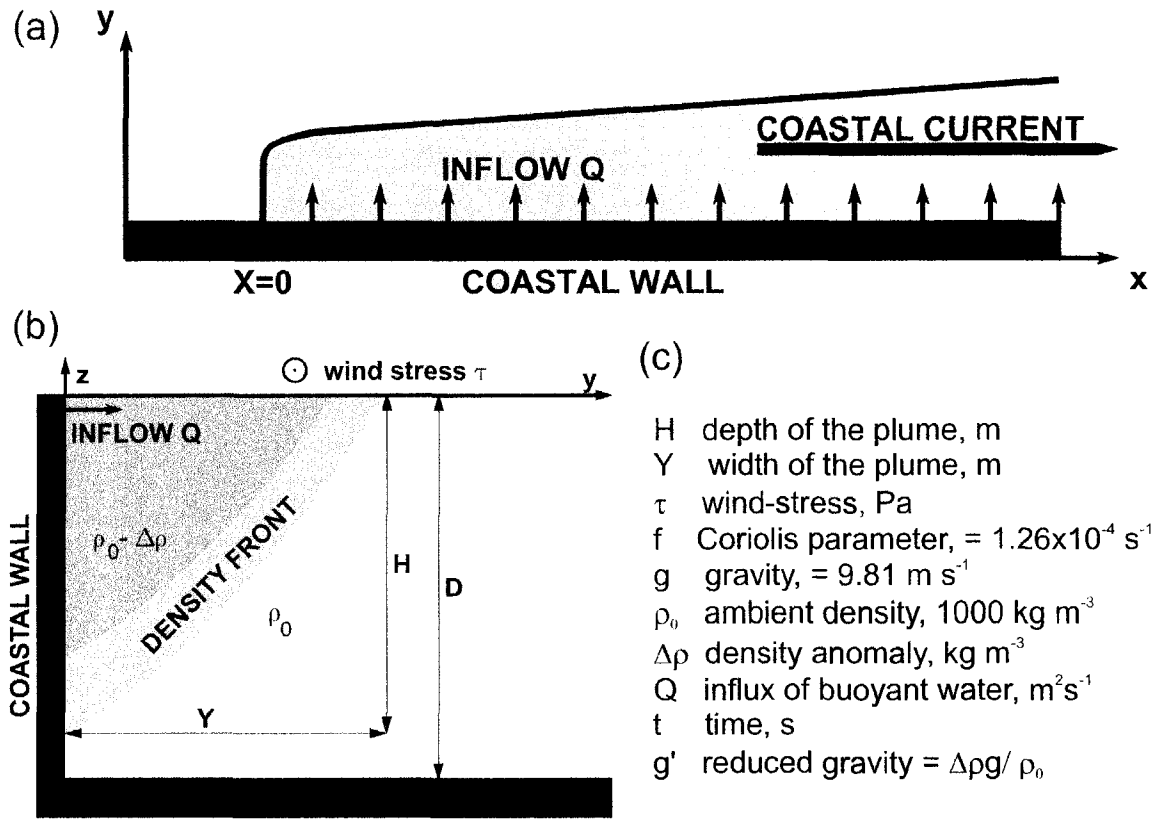

Figure 3.1: A schematic of the half-line source model used throughout this chapter. The panels are (a) a view from above, (b) a cross-shelf slice, and (c) a list of variable definitions.

rivers that drain from the surrounding coastal mountain ranges [*Royer*, 1982]. Rather than a uniform half-line source, the discharge could be better represented with an alongshore-varying line source punctuated by point sources to represent the few larger rivers that drain into the Gulf of Alaska. Adding this kind of realism to the freshwater input is beyond the scope of this idealized, process-oriented study, and is better suited to more realistic numerical simulations. The combined freshwater discharge of the large rivers, such as the Alsek, Copper and Susitna Rivers, has been crudely estimated to be only 20% of the total discharge into the Gulf of Alaska [*Royer*, 1982]. In light of this, and considering our rudimentary knowledge of the actual distribution of the coastal discharge due to lack of data, a half-line source is chosen for the discharge distribution in this study.

The half line source differs from the full-line source used in the previous 2-dimensional modeling chapter by having a beginning and extending to infinity in the direction the coastal current flows. In using a half-line source, the along-shelf transport of buoyant water in the coastal current at any along-shelf location eventually becomes constrained, through continuity, by the rate of inflow of buoyant water upstream of that location. This results in a fully 3-dimensional flow that is qualitatively very different from the full-line source 2-dimensional flow.

A schematic of the simplified model is shown in Figures 3.1(a), (b) and (c). The half-line source begins at $x = 0$ and continues indefinitely in the positive x direction, with uniform strength $Q\ m^2 s^{-1}$. The line source has a density deficit $\Delta\rho$ relative to the

surrounding ambient water of constant density ρ_0. At time $t = 0$ the line source is switched on and buoyant water flows into the model domain from the coast at the surface. Due to the Coriolis force the buoyant water turns to the right to flow along-shore and form a continuous coastal current in $x > 0$ that flows in the direction of Kelvin wave propagation. This direction is referred to as 'downstream' in the remainder of this chapter.

3.2 1½-layer model

A 1½-layer model of the half-line source, where a homogeneous upper layer of buoyant inflow water develops above a motionless, infinitely deep lower layer, can be constructed in a similar fashion to the 2-dimensional modeling of the infinite line source in the previous chapter. The governing equations are

$$\begin{aligned} fu &= -g' h_y && \text{(geostrophic cross-shelf momentum)}, \\ u_t + uu_x + vu_y - fv &= -g' h_x && \text{(along-shelf momentum)}, \\ h_t + (hu)_x + (hv)_y &= 0 && \text{(continuity)}, \end{aligned} \tag{3.1}$$

where subscripts denote partial differentiation, (u,v) are the along- and cross-shelf velocities respectively in the upper layer, and the other variables were introduced in Figure 3.1. Geostrophic balance in the cross-shelf momentum equation results from

assuming that along-shelf length scales are much greater than cross-shelf length scales. This is the so-called 'long-wave' approximation and is valid for this long, narrow coastal current away from the beginning of the line source.

Initially, in $x > 0$, the coastal current develops 2-dimensionally with no along-shelf variation in any variable, so results from the previous chapter apply. To summarize the 2-dimensional case, the governing equation for the cross-shelf profile of the depth of the coastal current is

$$h_{yy} + \frac{f^2}{g'} = 0. \tag{3.2}$$

This is the long-wave approximation for a zero potential vorticity flow and arises from applying the boundary condition of $u = 0$ at the coast. It has the self-similar solution

$$\frac{h}{H} = 1 - \frac{y^2}{Y^2}. \tag{3.3}$$

Using the continuity equation then gives

$$H = \frac{3^{2/3}}{2}\left(\frac{Q^2 f^2}{g'}\right)t^{2/3}, \quad Y = 3^{1/3}\left(\frac{g'Q}{f^2}\right)^{1/3} t^{1/3}. \tag{3.4}$$

Returning to the 3-dimensional half-line source model, integrating the geostrophic equation over the depth and width of the current gives

$$U = \frac{g' H^2}{2f}, \tag{3.5}$$

so that the along-shelf transport in the coastal current does not depend on the details of the cross-shelf structure of the current but only on g', f, and H. Because this is a half line source model, alongshore transport of buoyant water U at any alongshore location x is eventually limited by the total rate of influx of buoyant water Qx upstream of x through along-shelf advective processes. Equating Qx and U gives

$$H_{\max} = \left(\frac{2Qf}{g'}\right)^{1/2} x^{1/2}, \tag{3.6}$$

where $H_{\max}$ is the maximum depth possible for the coastal current at the coast and is also the depth necessary for any steady state. However, we show below that along-shelf advection becomes important and the flow 3-dimensional before $H_{\max}$ is reached, so $H_{\max}$ is only approached, not attained, in the half-line source model.

A similarity solution can be found for the full 3-dimensional half-line source model by writing

$$h = Hh', \quad y = Yy', \quad x = A(g'fQ)^{1/3}t^{4/3}x', \tag{3.7}$$

where A is a constant and h', y', and x' are non-dimensional. With these scales an equation for h' in terms of the similarity variables x' and y' can be formed from equations (3.1) that does not explicitly depend on time t

$$\begin{aligned} &-(2+h_{yy})[4Axh_x(2+h_{yy})+h_y{}^2(A-4h_{xy})+2h_y(2h_{yy}h_x+A(y-2xh_{xy}))] \\ &+h[2Ah_{yy}{}^2+h_{yyy}(2Ay-8h_x+h_y(A-4h_{xy})-4Axh_{xy})+8(A+(Ax+h_y)h_{xyy}) \\ &+4h_{yy}(2A+(Ax+h_y)h_{xyy})]=0, \end{aligned} \tag{3.8}$$

where variables are now non-dimensional and the primes have been dropped. Although a solution of this equation has not been obtained, the scaling used for the along-shelf coordinate x (3.7) in deriving (3.8) indicates that the transition from 2-dimensional flow to 3-dimensional flow occurs at alongshore location X and at time T where

$$X = A(g'fQ)^{1/3}T^{4/3}. \tag{3.9}$$

The numerical modeling shown next gives A~3/4, which means that the transition is moving close to the speed $\sqrt{g'H}$. The similarity equation also indicates that the coastal current does not reach a steady state. The depth and width of the coastal current always increase, the depth being limited by $H_{\max}$ and the maximum width of the coastal current being Y. The numerical modeling shows that the width of the coastal current is close to

Y everywhere except very near the beginning of the half line source, where the assumption of cross-shelf geostrophy is invalid.

Approximate time and length scales for the ACC can be estimated using the above results for the analytical model if we choose to ignore wind-stress. For example, if we use $X = 1500\ km$, which is approximately the location of Cape Fairfield with respect to the *Royer* [1982] discharge model, and take values that are representative of the ACC (see next section) in fall, we have $H_{\max} = 57\ m$, $Y = 15\ km$, and the time taken until the flow becomes 3-dimensional $T \simeq 20\ days$. For values representative of the ACC in summer we get $H_{\max} = 27\ m$, $Y = 11\ km$, and $T \simeq 25\ days$; and for the winter $H_{\max} = 43\ m$, $Y = 12\ km$, and $T \simeq 22\ days$. The depth and width estimates are reasonable but somewhat small (by about a factor of 2) in comparison to the ACC shown in Figure 2.3. The time scale is more interesting and indicates that alongshore advection may be important in the Alaska Coastal Current on time scales of less than 1 month.

3.3 Numerical model

The numerical model used is the Regional Ocean Modeling System (ROMS) [*Shchepetkin and McWilliams*, 2000]. The model is a free-surface, s-coordinate, 3-

dimensional primitive equation, finite-difference model. The equations solved by ROMS are:

$$
\begin{aligned}
&u_t + (\mathrm{u}\bullet\nabla)u - fv = -\phi_x + A_H(u_{xx} + u_{yy}) + (A_V u_z)_z, \\
&v_t + (\mathrm{u}\bullet\nabla)v + fu = -\phi_y + A_H(v_{xx} + v_{yy}) + (A_V v_z)_z, \\
&\phi_z = -b, \\
&u_x + v_y + w_z = 0, \\
&b_t + (\mathrm{u}\bullet\nabla)b = K_H(b_{xx} + b_{yy}) + (K_V\ b_z)_z,
\end{aligned}
\tag{3.10}
$$

where subscripts denote partial differentiation. ROMS solves equations for temperature and salinity and then uses an equation of state to calculate density. However, herein we use only salinity (which is the predominant variable affecting density on the Gulf of Alaska shelf [*Royer*, 1998]) and a linear equation of state. A_H and K_H are the horizontal eddy viscosity and diffusivity respectively. The horizontal diffusivities used were typically $2\ m^2 s^{-1}$, which was the smallest value that consistently damped numerical noise in the model. Horizontal diffusivity causes the coastal current to broaden as it flows along the coast. This effect can be pronounced in the relatively long model domain used here for horizontal diffusivities greater than $10\ m^2 s^{-1}$, but is acceptably minimized when $A_H = K_H = 2\ m^2 s^{-1}$.

The vertical diffusivities in these numerical experiments were typically calculated using a Mellor-Yamada level 2.5 turbulence closure scheme embedded within ROMS [*Mellor and Yamada*, 1982] which uses the limitation on the mixing length scale suggested by

Galperin et al. [1988] and the stability function suggested by *Kantha and Clayson* [1994]. A background vertical eddy diffusivity of $2\times10^{-5}\ m^2s^{-1}$ was used following *Allen and Newberger* [1996].

The equations are subject to the surface and bottom boundary conditions of no flow and no buoyancy flux through the free surface and through the bottom, surface stress due to the wind, and bottom stress. These boundary conditions are formulated as:

$$\begin{aligned} &w = \eta_t \text{ at } z = \eta, \\ &uD_x + vD_y = 0 \text{ at } z = -D, \\ &A_V u_z = \tau / \rho_0, v_z = 0 \text{ at } z = \eta, \\ &A_V u_z = C_D(u^2 + v^2)u,\ A_V v_z = C_D(u^2 + v^2)v \text{ at } z = -D, \end{aligned} \tag{3.11}$$

where η is the free-surface height. C_D is a drag coefficient

$$C_D = \kappa^2 \left(\ln \frac{\Delta z_b}{z_0} \right), \tag{3.12}$$

where $\kappa = 0.4$ is von Karman's constant, z_0 is the bottom 'roughness' scale, and Δz_b is the distance from the bottom to the first horizontal velocity point on the numerical grid.

The model domain used to study the half-line source is shown in Figure 3.2. A free-slip, mixed-slip or no-slip boundary condition is applied at the coastal wall

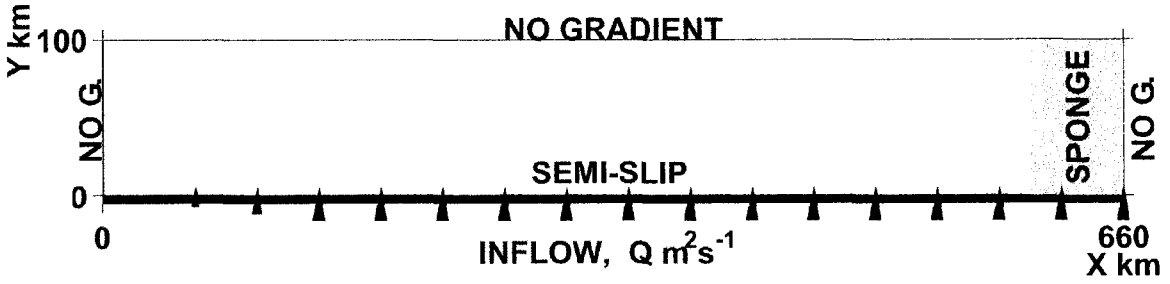

Figure 3.2: A diagram of the model domain used for numerical modeling of the half-line source.

$$v = 0,\ u_0 = \gamma u_1 \text{ at y} = 0, \tag{3.13}$$

where u_0 is the along-shelf velocity ½-grid point landward of the coastal wall, u_1 is the along-shelf velocity ½-grid point seaward of the coastal wall, and γ is a constant between 1 and –1. γ=1 is the free-slip boundary, $\gamma = 0$ is the mixed slip boundary, and $\gamma = -1$ is the no-slip boundary. A no-gradient open boundary condition is applied on all variables at the offshore, downstream and upstream edges of the model domain,

$$u_\varphi = v_\varphi = b_\varphi = 0, \tag{3.14}$$

where φ is the coordinate perpendicular to the boundary. These boundary conditions are dynamically consistent with the Ekman outflow and inflow and geostrophically balanced flow across the boundaries. The no-gradient open boundary at the downstream end of the model domain is augmented with a sponge region to dampen $2\Delta x$ noise that is generated at the boundary. The sponge is typically a $60\ km$ long region containing smoothly-increased along-shelf diffusion of $u, v,$ and ρ. The along-shelf diffusion in the sponge is $200\ m^2 s^{-1}$ but the cross-shelf diffusion remains unchanged.

Typical horizontal grid spacing was $3\ km$ in the along-shelf direction and $0.5 - 2\ km$ in the cross-shelf direction. The vertical grid contained 20 to 40 grid points with greater

resolution in the surface and bottom boundary layers if required. The time step was chosen so that advection, wave propagation, and diffusion were all properly resolved. Typically, there were 480-720 time steps in 24 hours. A few experiments were done at twice the horizontal resolution to test the accuracy of the flow fields at the lower resolutions chosen.

Although there are many ways to introduce buoyant water at the coast, all are rather unrealistic in some way. In the numerical modeling presented here, buoyant water is introduced at the surface grid point. The inflow has density deficit $\Delta\rho$ and is directed offshore so the along-shore inflow velocity $u_I = 0$ and the cross-shore inflow velocity $v_I = Q/\Delta z$ where Q is the volume inflow rate and Δz is the thickness associated with the surface grid point. The inflow density is not that of pure freshwater but is assumed to have undergone some mixing with seawater prior to reaching the coast and is modeled to have the maximum density deficit observed within the ACC for the season being studied. The inflow rate Q is then artificially increased so that the freshwater input Q_f into the modeled Gulf of Alaska is correct following *Royer* [1982] estimates. This gives

$$Q = \left(\frac{\rho_s - \rho_f}{\Delta\rho}\right) Q_f \tag{3.15}$$

where ρ_f and ρ_s are the densities of freshwater and ambient seawater respectively. Figure 3.3 shows a graph of Q against $\Delta\rho$ for the annual maximum and minimum Q_f taken from Figure 2.1. For each value of Q_f there is a range of possible values of Q and $\Delta\rho$. The values used in this study to represent the seasonal variation of the inflow are $Q = 0.1\ m^2 s^{-1}$, $\Delta\rho = 1\ kg\,m^{-3}$ for winter (during low discharge), $Q = 0.075\ m^2 s^{-1}$, $\Delta\rho = 4\ kg\,m^{-3}$ for summer (during medium discharge), and $Q = 0.15\ m^2 s^{-1}$, $\Delta\rho = 3\ kg\,m^{-3}$ for fall (during high discharge). The values of $\Delta\rho$ for each season were obtained by inspecting the CTD sections of the Cape Fairfield and Seward Lines from 1998 to 2003, taken as part of the GLOBEC LTOP project. Note that the only way to model both inflow volume and buoyancy input correctly is to input the correct volume of *freshwater*. This produces a huge density difference at the coast under no-wind-stress conditions unless the inflowing freshwater is allowed to mix with the ambient water in an estuary or fjord in the numerical model. Modeling an estuary is possible for a line-source, but is not presented here for simplicity.

For the method of inflow used, the correct velocity v_I and depth H_I of the inflow water is that of a surface gravity current,

$$v_I = (2g'Q)^{1/3},$$
$$H_I = \left(\frac{Q^2}{2g'}\right)^{1/3}, \tag{3.16}$$

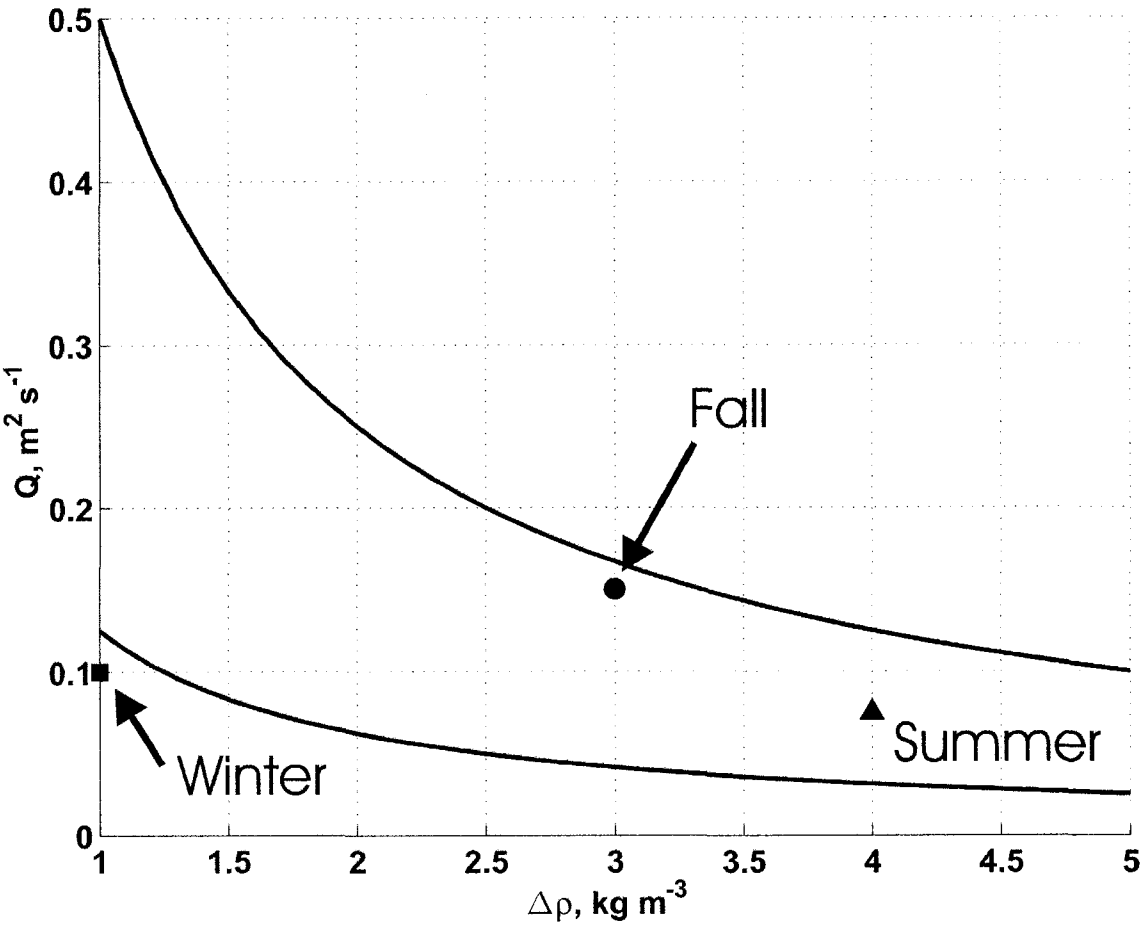

Figure 3.3: A graph of inflow rate of buoyant water Q versus density deficit $\Delta\rho$ of that water for the half-line source inflow. The upper curve represents a constant $40{,}000\ m^3s^{-1}$ of freshwater inflow, typical of the maximum inflow rate during fall, and the lower curve represents a constant $10{,}000\ m^3s^{-1}$, typical of the minimum inflow rate in winter. The values of Q and $\Delta\rho$ that were used in this study to represent summer, fall and winter conditions in the Gulf of Alaska are also marked.

so that $v_I = \sqrt{2g'H_I}$ [*Benjamin*, 1968]. We found that if the depth of the inflow is specified to be greater than the gravity-current depth the inflow quickly thins until the gravity current depth is reached. This produces strong upward vertical velocities at the coast that cause an artificial, cross-shelf, vertical circulation cell within the resulting coastal current. Alternatively, the depth of the inflow can be specified to be less than the gravity-current depth. In this case, the inflow quickly thickens until the gravity-current depth is reached and no erroneous large-scale circulation occurs. We choose the inflow depth to be the thickness of the surface grid point in the numerical model so the inflow cannot become thinner. This depth is also less than the gravity current depth H_I and so the initial inflow thickens on entering the model domain.

To decrease transients at the beginning of numerical model runs the wind-stress and half line-source are slowly ramped up to their full value over a period of $2\ days$. The beginning of the half line source at $x = 0$ is also smoothed in the along-shelf direction so that the strength of the source ramps up to its full value over the first $50\ km$. This is in keeping with the imprecise beginnings of the ACC in the southeastern Gulf and avoids an unwanted "bulge" of buoyant water forming at the beginning of the line source that is similar to the accumulation of buoyant water near the river mouth of surface trapped buoyant plumes described by *Fong and Geyer* [2002] and *Yankovsky and Chapman* [1997].

3.4 Numerical results

3.4.1 No wind-stress

The development in time of the perturbation density field for a no wind-stress model run, with parameters $Q = 0.1\ m^2 s^{-1}$, $\Delta\rho = 1 kg\, m^{-3}$ and $D = 50\ m$ (winter conditions), is shown in Figures 3.4, 3.5 and 3.6. Figure 3.4 shows the density along the coastal wall, as if looking through the coastal wall at the ocean, Figure 3.5 shows a view from above of sea-surface density, and Figure 3.6 shows a cross-shelf slice through the density field at $x = 300 km$, looking upstream. For each figure, panels (a), (b), (c) and (d) show conditions 10, 20, 40 and 100 *days* after buoyant inflow begins. Thick black lines indicate $H_{\max}$, the maximum possible depth of the coastal current from the 1½-layer model (Figure 3.4) and Y, the maximum width of the coastal current from the 1½-layer model (Figure 3.5).

As asserted for the 1½-layer analytical model, the buoyant inflow in the numerical model initially develops 2-dimensionally, away from the beginning of the line source. This 2-dimensional evolution is identical to that described in the previous chapter. At 10 *days* (in Figure 3.4(a)) the flow is 2-dimensional for $x > 300\ km$, where the isopycnals along the coast are horizontal, and 3-dimensional for $x < 300\ km$, where the isopycnals are

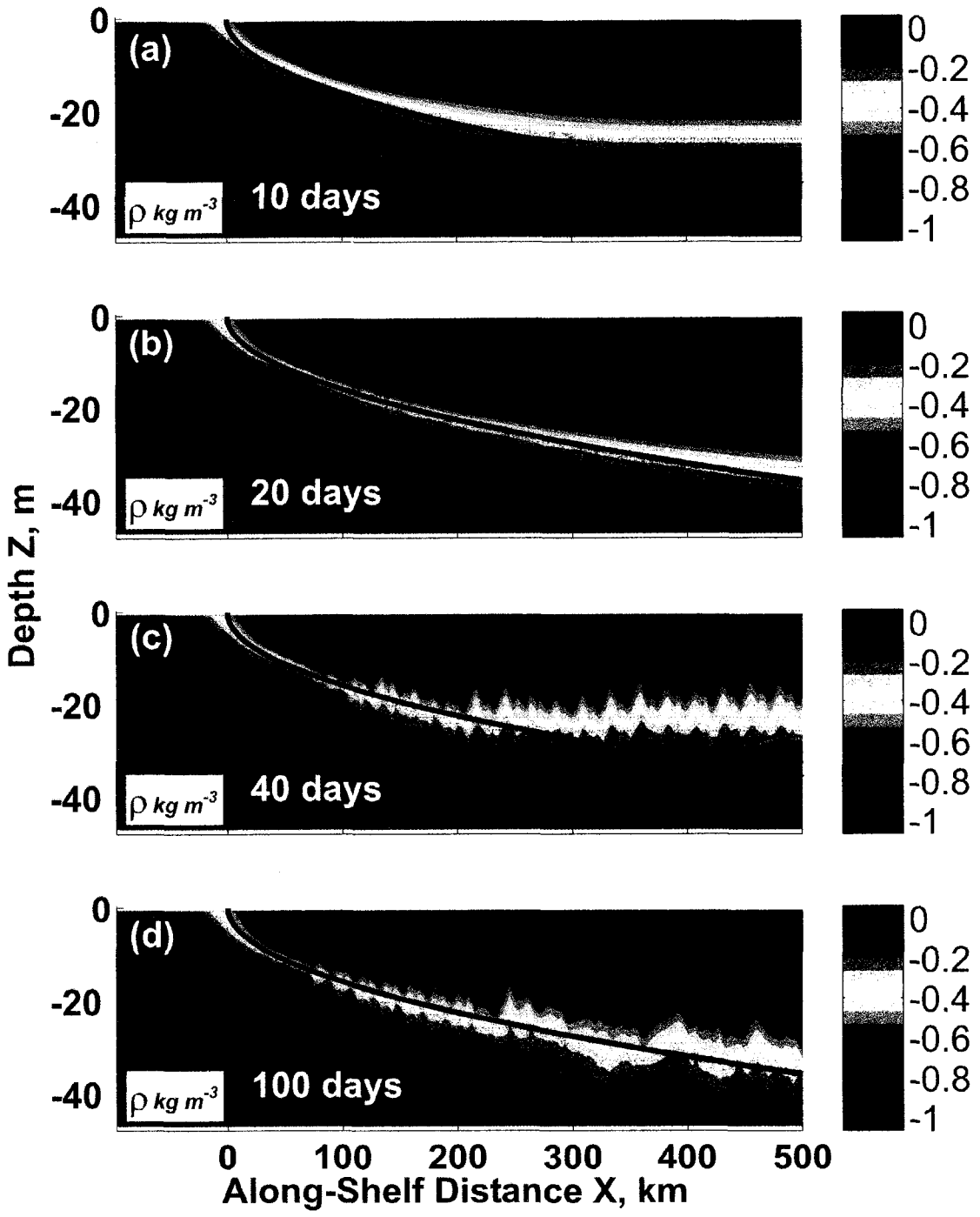

Figure 3.4: Plots of density anomaly on the coastal wall, as if looking through the coastal wall, for a no-wind stress model run with summer inflow conditions. Panels (a), (b), (c) and (d) are after 10, 20, 40 and 100 days of inflow respectively. The thick black lines show the maximum depth H_{max} of the equivalent 1½-layer coastal current.

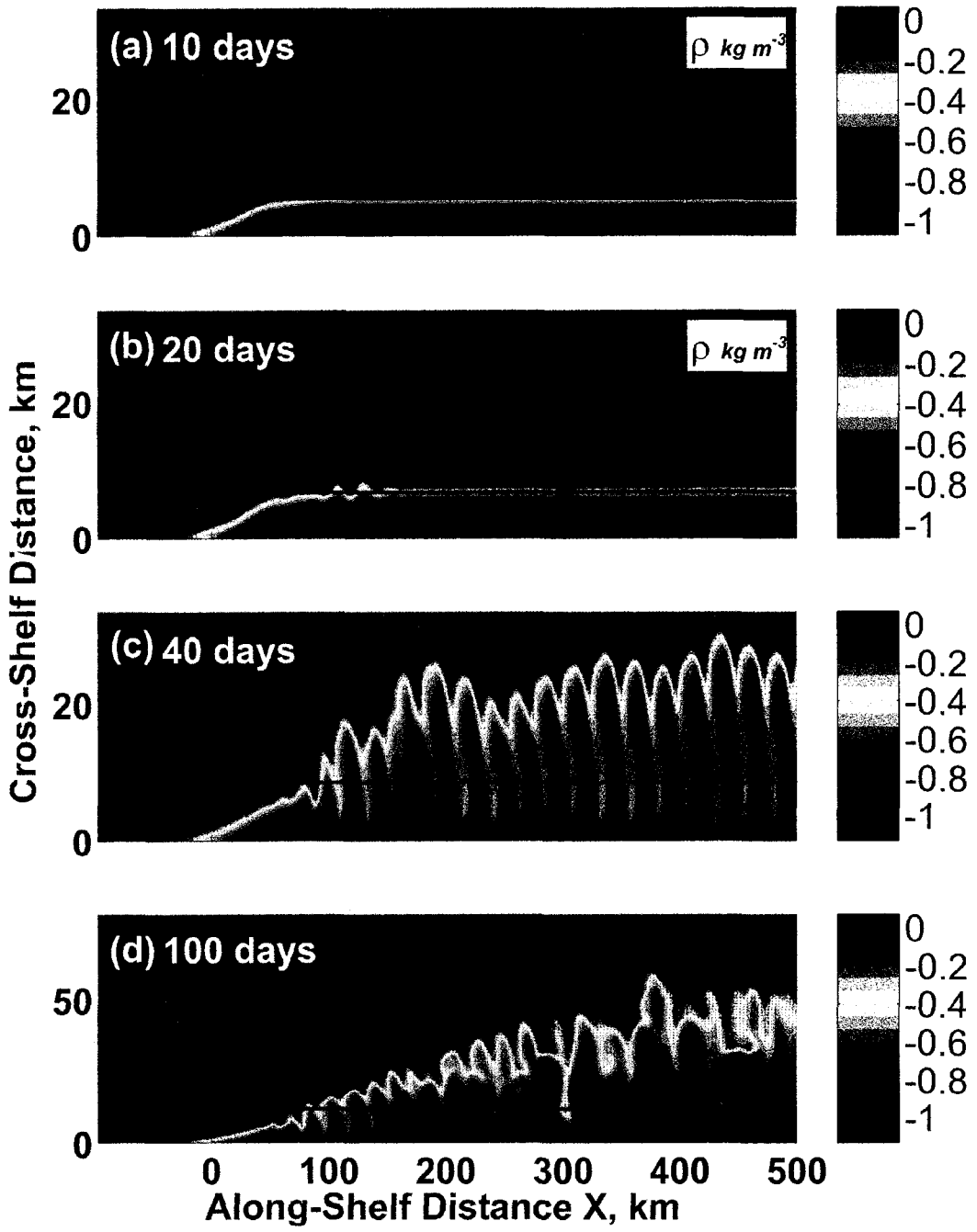

Figure 3.5: Plots of sea-surface density anomaly for the same model run depicted in Figure 3.4. Panels (a), (b), (c) and (d) are after 10, 20, 40 and 100 days of inflow respectively. Note that panels (a), (b) and (c) extend 50 km offshore, whereas panel (d) extends 80 km offshore. The thick black lines show the maximum width of the equivalent 1½-layer coastal current and the black dot in panel (b) shows the location of the momentum and density balances shown in Figure 3.6.

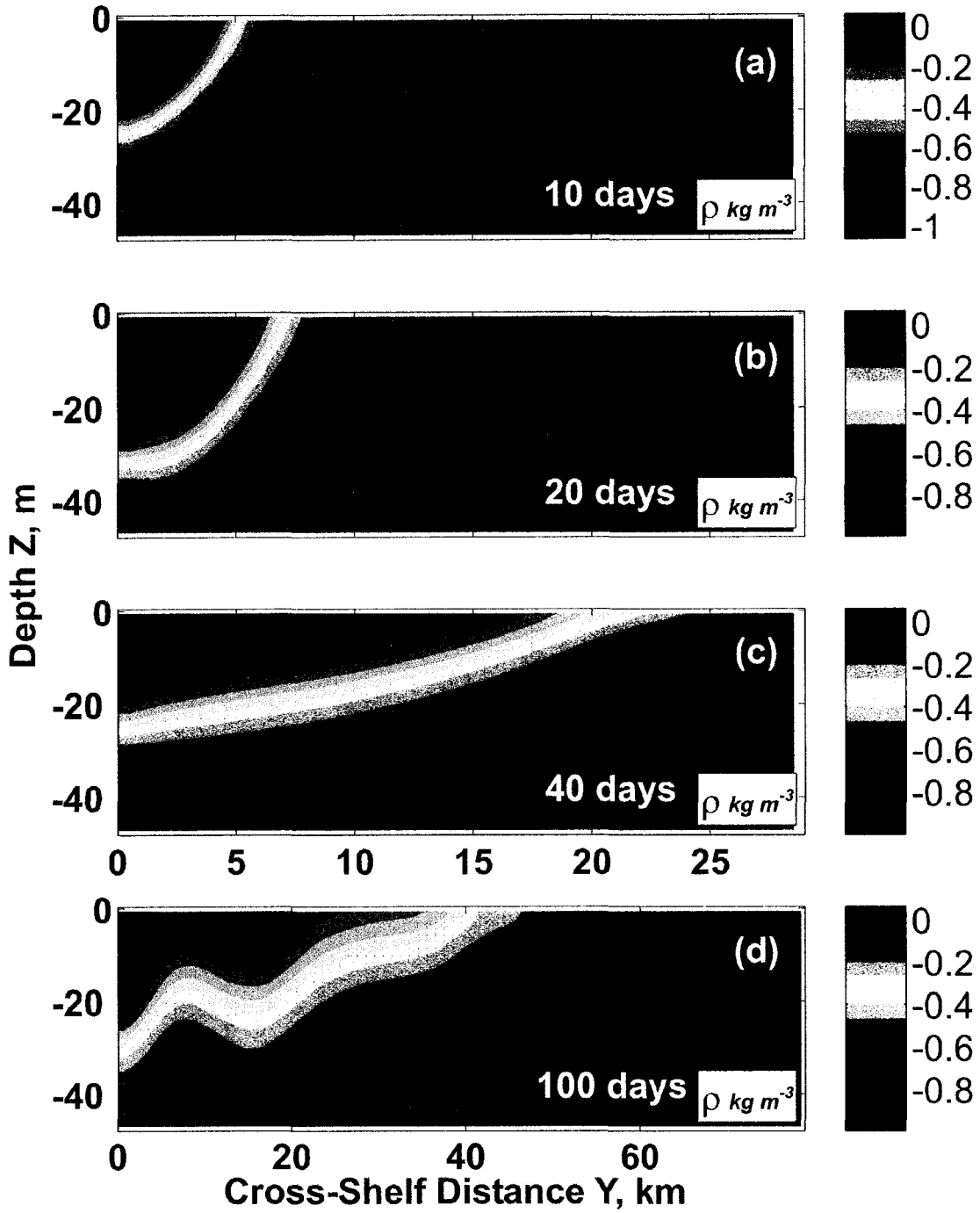

Figure 3.6: Plots of density anomaly for a cross-shelf slice located at $x = 300\ km$ for the same model run depicted in Figure 3.4. Panels (a), (b), (c) and (d) are after 10, 20, 40 and 100 days of inflow respectively. Note that panels (a), (b) and (c) extend 50 km offshore, whereas panel (d) extends 80 km offshore.

sloping. At 20 *days* (in Figure 3.4(b)) the flow is 3-dimensional at all along-shelf locations, the boundary between the 2-dimensional and 3-dimensional flows having moved beyond the downstream end of the model domain. The speed at which the boundary between the 2- and 3-dimensional flow moves along the coast is found to be roughly $\sqrt{g'H}$, the local internal wave speed based on the depth at the coast of the coastal current at this boundary. This speed therefore increases as the depth of the coastal current increases with time.

As the flow develops the depth of the buoyant water at the coast evolves to a nearly steady state after 20 *days* but does not quite reach the depth required for the steady state flow calculated in the 1½-layer model (Figures 3.4(a),(b)). This implies that the geostrophically-balanced, along-shelf transport in the coastal current is less than the volume input of buoyant water at the coast and so buoyant water must accumulate on the shelf and a steady state cannot form. The accumulation of buoyant water causes the coastal current to continually widen (Figures 3.5(a), (b)). Downstream of $x \simeq 80\,km$ (from Figure 3.5) this widening occurs so that the width of the coastal current is approximately constant in the along-shelf direction, the width being roughly that of the 2-dimensional coastal current, or, equivalently, the width of the coastal current far downstream.

During the 3-d phase of the flow, the 2-d constraint that the flow has zero potential vorticity of the previous chapter is broken so that the Coriolis term ($-fv$) and the cross-

shelf advection term ($+vu_y$) in the along-shelf momentum balance are no longer the only important terms. Figure 3.7 shows vertical profiles of the terms in the momentum and density equations at $x = 300\ km$, $y = 7\ km$ after $20\ days$ of buoyant inflow, at a location that is at the center of the along-shelf jet associated with the offshore edge of the coastal current (see Figure 3.5(b)). The along-shelf momentum balance and the density balance are complex, with all terms being important, including the along-shelf advection and the along-shelf pressure gradient. In the density balance, cross-shelf advection ($v\rho_y$) tends to cause the front to widen and vertical advection ($w\rho_z$) in the front tends to cause the front to deepen. The deepening is partially offset by along-shelf advection ($u\rho_x$), which tends to advect the shallower upstream coastal current downstream. The cross-shelf momentum balance is essentially in geostrophic balance, with the other terms in this equation being at least an order of magnitude smaller than the pressure gradient and Coriolis terms.

The half-line source coastal current depicted in Figures 3.4, 3.5, and 3.6 eventually becomes unstable leading to the formation of large amplitude waves or eddies, which cause a cross-shelf flux of buoyant water. The instability can first be seen in the sea surface density anomaly near the beginning of the line source at $t = 18\ days$, and growing waves are present throughout the coastal current by $t = 23\ days$ (see Figure 3.5(b) around $x = 100\ km$). Large amplitude waves or eddies are present at $t = 40\ days$ (see Figure 3.5(c)). The instability has a wavelength of about $25\ km$ (that is roughly the

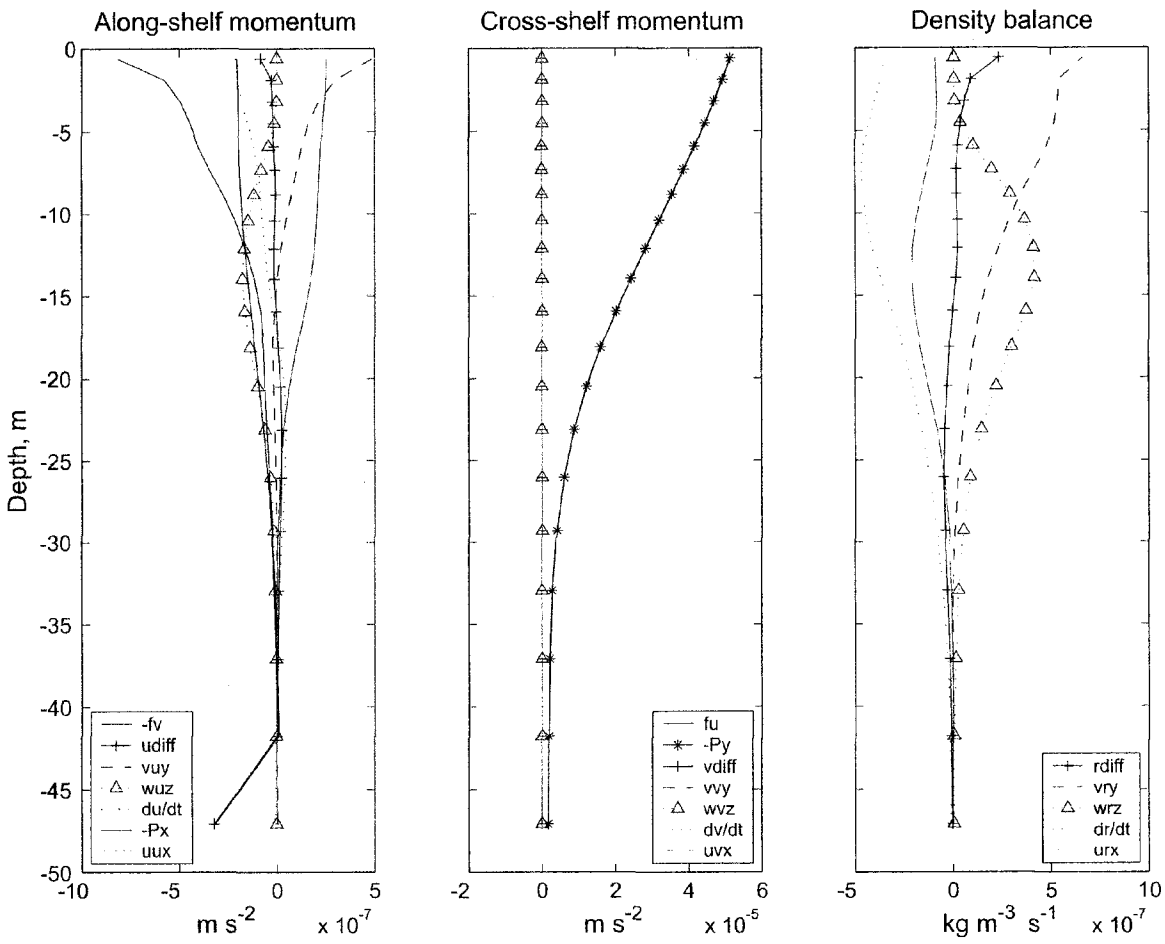

Figure 3.7: Profiles of the terms in the cross-shelf momentum equation, the along-shelf momentum equation, and the density equation. The profiles are taken from the model run depicted in Figures 3.4, 3.5, and 3.6 at the location $x = 300\ km$, $y = 7\ km$ (in the center of the front that bounds the coastal current), and $t = 20\ days$.

same at all along-shelf locations), and a phase speed in the downstream direction of about $4\ cms^{-1}$ (so that the eddies slowly move downstream at a speed that is slower than the maximum speed of the coastal current jet). The waves/eddies in the coastal current have a baroclinic structure, with the flow intensified at the surface, in the coastal current layer, but also extending throughout the water column to the bottom. The aspect ratio of the waves/eddies after 40 *days* of buoyant inflow is approximately 1 (although this is unclear in Figure 3.5 because the cross-shelf direction is exaggerated due to the aspect ratio of the plot). The large amplitude instability waves eventually break backwards (i.e. towards the upstream direction) to form cyclonic eddy-like features, one of which is shown in Figure 3.8.

The overall effect of the instability is to move the buoyant coastal current water much further offshore than if the current remained stable. After 40 *days* of inflow, the edge of the coastal current is nearly 30 *km* offshore, 3 times further than the slow offshore spreading of the equivalent stable coastal current. The additional offshore flux of coastal current water due to the instability implies that less buoyant water is available to be transported alongshore. Since alongshore transport is still, on average, in geostrophic balance, the decrease in alongshore transport is accompanied by a decrease in the depth of the coastal current at the coast. For the numerical model run presented in Figures 3.4, 3.5 and 3.6 this shoaling of the coastal current occurs between 20 and 40 days and can be seen in panels (b) and (c).

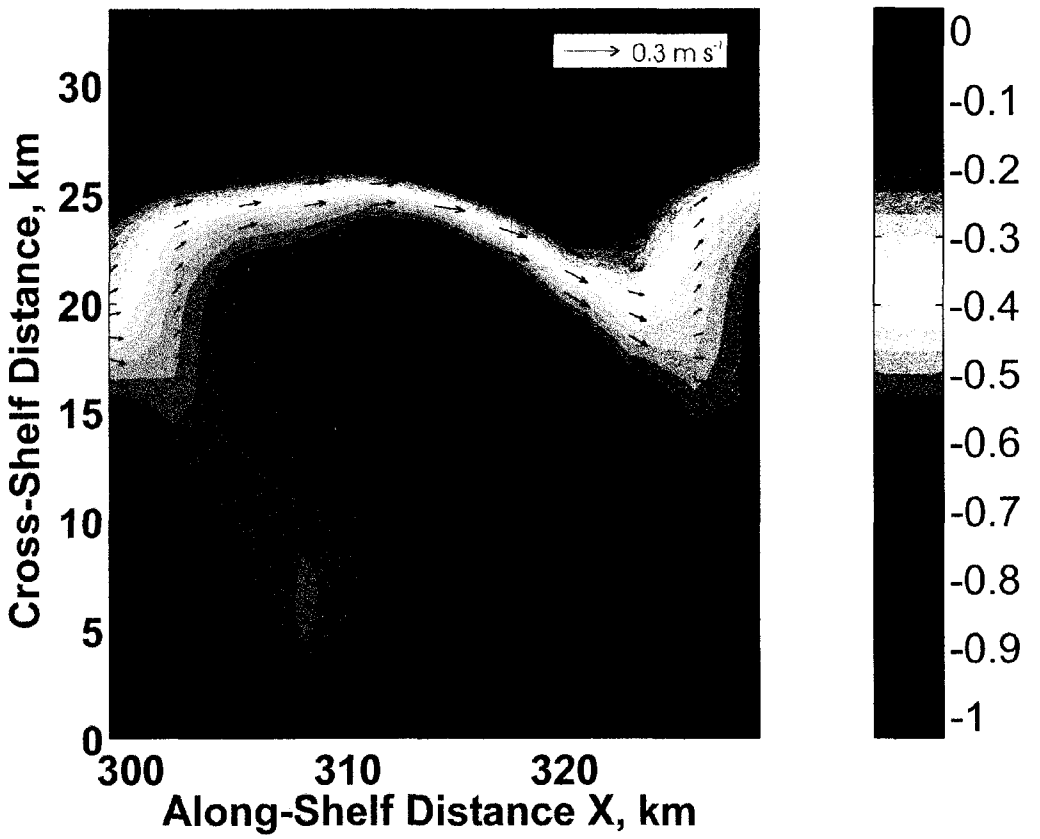

Figure 3.8: A plot of sea-surface density anomaly with surface velocity vectors over-laid at $t = 40$ *days* for the model run depicted in Figures 3.4, 3.5 and 3.6. Unlike Figure 3.5, the cross- and along-shore axes are at the same scale so the aspect ratio of the instability is correct.

The instability of a modeled line-source coastal current and the eddying motion that results has been documented before by *Griffiths and Linden* [1981], in which the instabilities were studied using a rotating tank with a periodic line source of buoyant water. There, the instabilities developed at a wavelength that was approximately twice the width of the coastal current at the onset of instability and had a downstream phase speed that was slow relative to the along-shelf flow. The instability waves grew and eventually broke backwards to form cyclonic eddy-like features that had an aspect ratio of about one.

Griffiths and Linden [1981] discuss a baroclinic instability mechanism for their coastal current by considering an analytical quasi-geostrophic, 2-layer model. For instability to occur in their model the Froude number Fr, defined by

$$Fr = \frac{f^2 Y^2}{g' H}, \tag{3.17}$$

and the layer depth ratio γ, defined by

$$\gamma = \frac{H}{D - H}, \tag{3.18}$$

both need to be larger than a critical value, small γ requiring large Fr for instability and large γ requiring a smaller Fr (see their Figure 7) . *Barth* [1989] also notes that decreasing γ has a stabilizing effect on an upwelling front, and that baroclinic instability

is suppressed in 1½-layer models (where $\gamma = 0$), since the lower layer is too massive to be accelerated.

The instability of the half-line source coastal current shown here is essentially the same as the ones described by *Griffiths and Linden* [1981] and very similar to those in a subsequent paper *Griffiths and Linden* [1982]. For the half-line source presented here, when the coastal current becomes 3-dimensional, the depth H of the coastal current at the coast is close to H_{max} and so the depth ratio γ becomes nearly steady. The width of the coastal current Y continues to increase, unaffected by the transition from 2-dimensional flow to 3-dimensional flow, and thus the Froude number Fr of the coastal current increases. As Fr increases at nearly constant γ, the coastal current eventually becomes baroclinically unstable. The value of Fr at which instability occurs depends on the depth ratio γ, but it is problematic to assign a single Froude number and depth ratio to the instabilities, because these vary along the coast. Near the beginning of the coastal current, H is small, leading to large Fr (promoting instability) and small γ (promoting stability). Further along the coastal current, H is larger leading to a smaller Fr (promoting stability) but a larger γ (promoting instability). For the 500 *km* long coastal currents modeled here, these two effects appear mostly to cancel out and instabilities grow at all along-shelf locations at roughly the same time, though more slowly growing instabilities often appear near the beginning of the coastal current several days before the rest of the coastal current becomes unstable.

A series of numerical experiments were performed to represent the ACC in winter, summer and fall and to explore the effect of variations in bottom depth on the instabilities. Figure 3.9 shows Fr versus γ calculated at the arbitrary location $x = 300\ km$ at the onset of instability for these model runs. As anticipated, deeper bottom depths, small γ, tend to stabilize the system to so that the Froude number is larger at instability, the coastal current is wider, and the growth rate is slower. The phase speed of the instabilities is slowly downstream in all cases ($3 - 4.5\ cm\ s^{-1}$), and the wavelength scales best as roughly 3.5 times the width of the coastal current at instability. *Griffiths and Linden* [1982] found that the wavelengths of their coastal current instabilities scaled as 2-3 times the width of the coastal current if the coastal current was less than about 6 Rossby radii wide, and scaled as roughly 7 times the Rossby radius if the coastal current was much wider than the Rossby radius. The half-line source coastal current studied here is 3-4 Rossby radii wide at instability and so from *Griffiths and Linden* [1982] the wave length of the instability might be expected to be proportional to the width.

Finally, panels (d) of Figures 3.4, 3.5 and 3.6 show the model run after 100 days of inflow. The eddying motions caused by the instability have now spread the buoyant water over $60\,km$ offshore, although the buoyant water remains connected to the coast (see Figure 3.5(d)) rather than being transported offshore in self-advecting eddy pairs. The depth of the coastal current is also near its steady state depth again (Figure 3.4(d)) indicating an increased transport of buoyant water downstream and a reduced

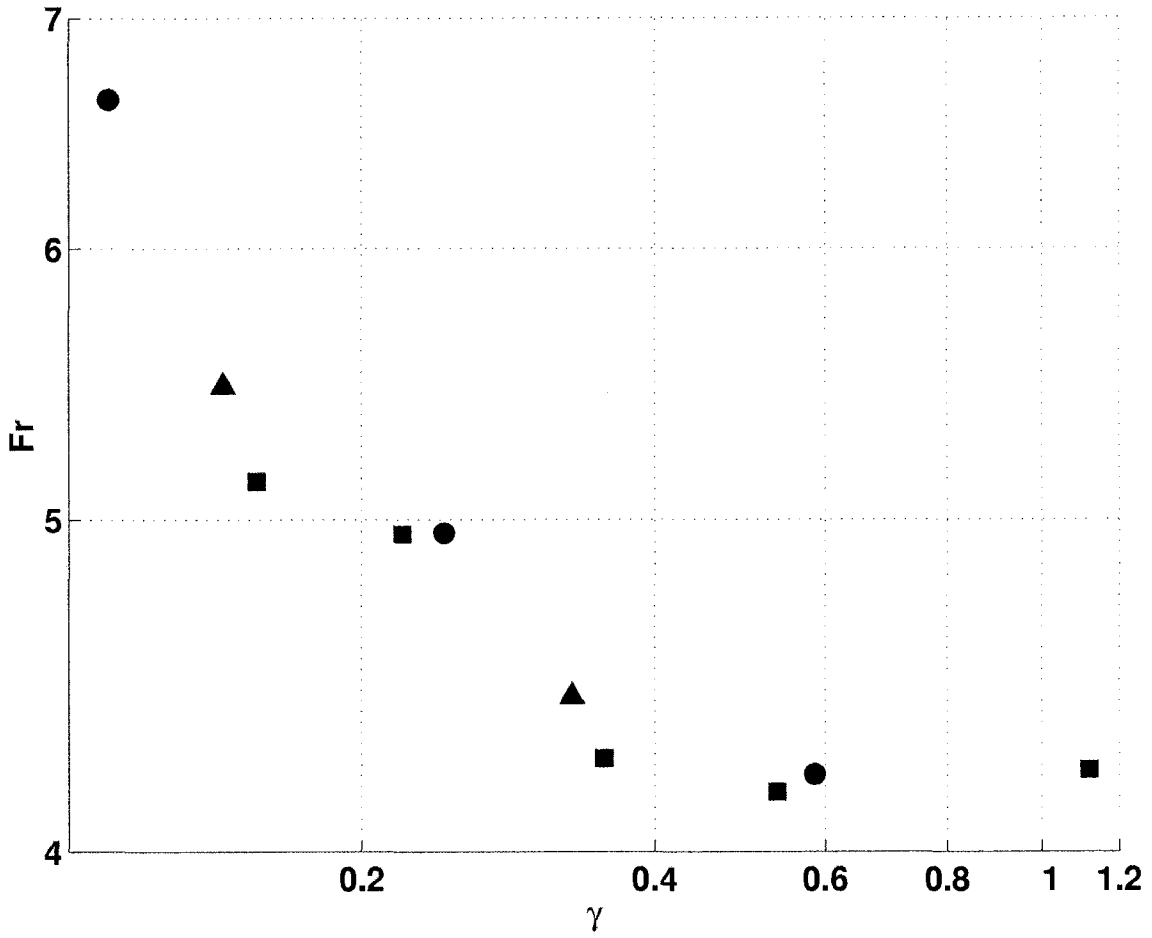

Figure 3.9: A log-log plot of layer depth ratio γ versus Froude number Fr calculated at the onset of instability. The data shown are for no-wind-stress model runs with varying depths and inflows. Squares are for fall inflow conditions, triangles are for winter inflow conditions, and circles are for summer inflow conditions.

accumulation rate of buoyant water on the shelf due to the eddying motions. The cross shelf structure of the coastal current in $y < 15\ km$ is now very similar to that at $t = 20\ days$ (see Figure 3.6(b), (d)), suggesting that the coastal current might repeat its instability if the numerical model were run longer.

3.4.2 Downwelling wind-stress

In the 2-dimensional modeling presented in the previous chapter, wind-forced downwelling at the coast causes the coastal current to deepen until it becomes attached to the bottom. This deepening does not occur in the 3-dimensional downwelling wind-stress case because the depth of the coastal current at the coast is limited in a similar way to the no wind-stress case.

The cross-shelf momentum balance is geostrophic in the downwelling wind-stress case, so that the depth of the coastal current at the coast still relates to baroclinic along-shelf transport via equation (3.5). However, an additional barotropic component to the along-shelf flow is accelerated until it causes an along-shelf bottom-stress that is equal to the downwelling wind-stress. For the bottom friction parameterization and range of wind-stresses used in this study, $0.0125 - 0.1\ Pa$, we find that the barotropic flow varies from $4.6 - 13\ cm\,s^{-1}$ respectively. This additional along-shelf flow ought to reduce the depth of the coastal current at the coast in a steady state compared to the no wind-stress model

runs, but the effect is not apparent in the numerical model results. This is probably because Ekman balance does not apply within the coastal current (see below) so that along-shelf barotropic flow is not required near the coast. Another reason is that the baroclinic flow speed increases during downwelling wind-stress making the barotropic flow only 10-20% of the baroclinic flow.

Figure 3.10 shows a typical quasi-steady state that forms under downwelling wind-stress. The model run is shown after $20\ days$ of buoyant inflow and has a strong mean downwelling wind-stress of $\tau = 0.05\,Pa$, typical of the fall and winter months in the northern Gulf of Alaska (see Figure 2.1), inflow parameters of $Q = 0.15\ m^2\ s^{-1}$, $\Delta\rho = 3\ kg\,m^{-3}$ (also typical of fall), no ambient stratification and a flat bottom at $100\ m$ depth. As anticipated above, the depth of the coastal current is limited to essentially the same depth as the no-wind-stress coastal current, so that H_{max} still roughly follows the middle of the density front (see Figure 3.10(b)) though significant mixing due to the wind has broadened the 'pycnocline' at the coast between the buoyant inflow water and the ambient water (compare Figure 3.4 with 3.10(b)).

During downwelling wind-stress, the coastal current is compressed against the coast due to onshore Ekman transport so that it becomes much narrower than the equivalent no-wind-stress coastal current (see Figure 3.10(a)) and the width of the current comes to a quasi steady state. Using the crude 1½-layer model of the coastal current, and including downwelling wind-stress, the vertically integrated along-shelf momentum equation is

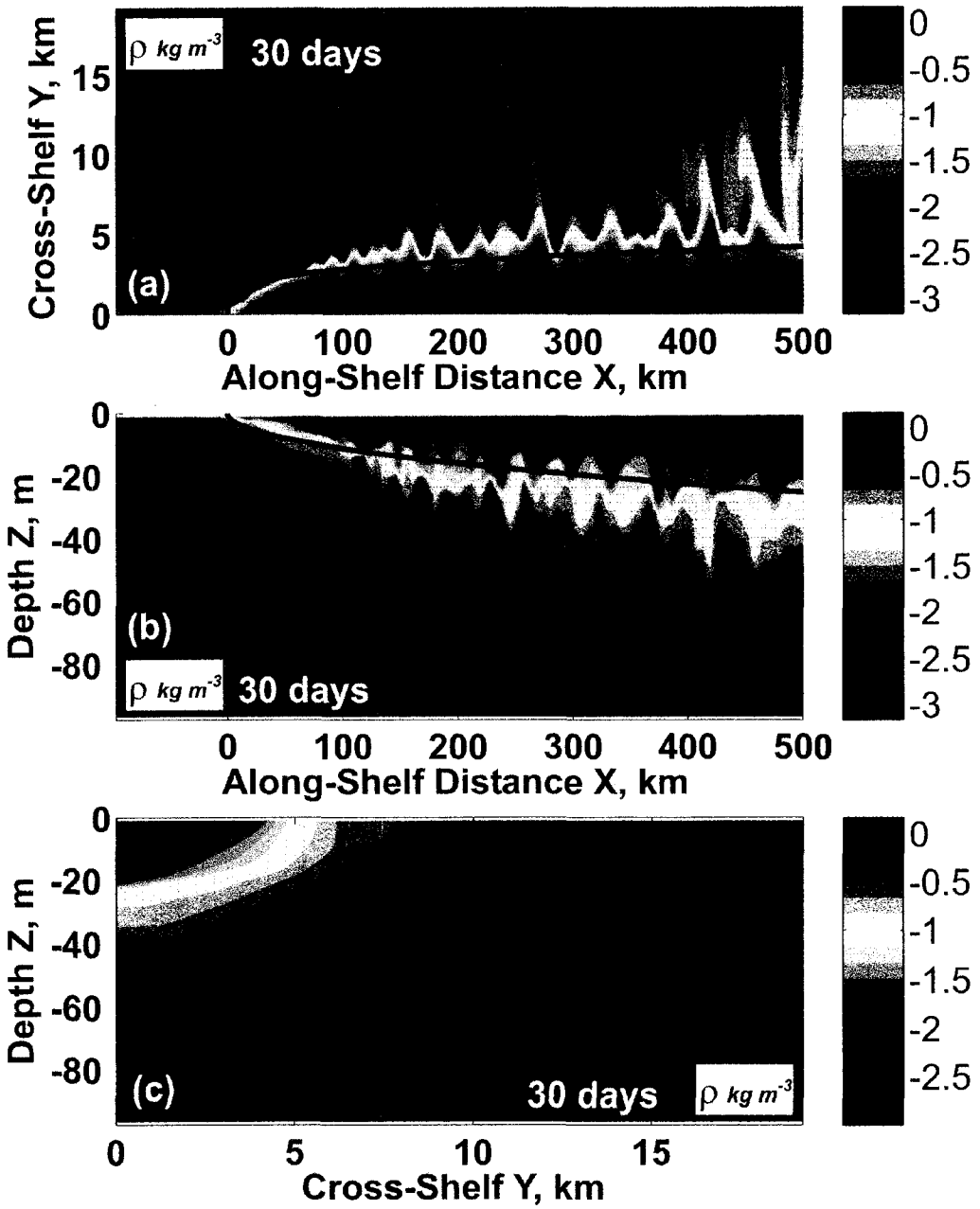

Figure 3.10: A downwelling wind-stress model run with $\tau = 0.05\ Pa$ after 30 *days* of fall inflow conditions, showing density anomaly for (a) the sea surface, (b) the coastal wall and (c) a cross shelf slice at $x = 300\ km$. In panel (a) the dashed thick black line is the maximum width of the equivalent no-wind-stress 1½-layer model, and the solid thick black line represents the scaling for the quasi-steady width of the coastal current during downwelling wind-stress given by equation (3.21). H_{max} is shown by a thick black line in panel (b).

$$u_t h + uu_x h + vu_y h - fvh = -g' h_x h + \tau / \rho_0. \tag{3.19}$$

Note that a similar equation to this can be found by vertically integrating the flux form of the Boussinesq along-shelf momentum equation used by ROMS from beneath the coastal current to the surface. Simple estimates of the size of these terms in (3.19) are

$$\begin{aligned}
fvh &\sim f\frac{Q}{H_{\max}}H_{\max} \sim Qf, \\
g' h_x h &\sim g'(H_{\max})_x H_{\max} \sim Qf, \\
uu_x h &\sim \frac{g' H_{\max}}{fY_{wind}}\frac{g'(H_{\max})_x}{fY_{wind}}H_{\max} \sim \frac{g'^{1/2}Q^{3/2}X^{1/2}}{f^{1/2}Y_{wind}^{\ 2}}, \\
vu_y h &\sim \frac{Q}{H_{\max}}\frac{g' H_{\max}}{fY_{wind}^{\ 2}}H_{\max} \sim \frac{g'^{1/2}Q^{3/2}X^{1/2}}{f^{1/2}Y_{wind}^{\ 2}}, \\
\frac{\tau}{\rho_0} &\sim \frac{\tau}{\rho_0},
\end{aligned} \tag{3.20}$$

where Y_{wind} is the quasi-steady width of the coastal current during downwelling wind-stress, v is taken to scale as the inflow velocity, u is scaled geostrophically, and $H_{\max}$ is as given in (3.6). The along-shelf pressure gradient and the Coriolis force are not expected to increase due to a narrowing coastal current, and so these terms do not cause balance in the along-shelf momentum equation as the coastal current is compressed against the coast. In particular, if the Coriolis term balanced the downwelling wind-stress in simple Ekman balance, onshore flow is required, which implies, through the continuity equation, that the coastal current ought to narrow rather than widen in the positive-x

direction. However, both the along-shelf and cross-shelf advective terms are of the correct sign to balance the downwelling wind-stress, and the scales for these terms in (3.20) increase as Y_{wind} decreases, thus allowing the possibility that these terms balance the downwelling wind-stress. Equating the scale for the wind-stress and the scale for the advective terms gives an estimate for Y_{wind} / L_D

$$\frac{Y_{wind}}{L_D} \simeq A\left(\frac{Qf}{\tau / \rho_0}\right)^{1/2} \text{ where } L_D = \frac{\sqrt{g' H_{\max}}}{f}, \tag{3.21}$$

and A is a constant of proportionality. Note that the factor $Qf/(\tau/\rho_0)$ in (3.21) is the ratio of the offshore-directed inflow 'transport' to the onshore-directed Ekman transport. Figure 3.11 shows a plot of this relationship for several downwelling wind-stress model runs, where Y_{wind} / L_D has been estimated at $x = 300\ km$ from the beginning of the line source. The best fit occurs with $A \simeq 1.06$ and this relationship is plotted as a thick black line in Figure 3.10(a). Deviation of the downwelling wind-stress numerical model runs from equation (3.21) is expected due to neglect of the Coriolis and pressure gradient terms. However, the downwelling numerical model also contains wave or eddy-like features that are similar to those found in the no wind-stress case, which make estimation of the width of the coastal current problematic as they develop. In this case, the width was estimated after 15 *days* of buoyant inflow and wind-stress, before the eddying motions became too large in the low wind-stress model runs and after the mean width appeared steady.

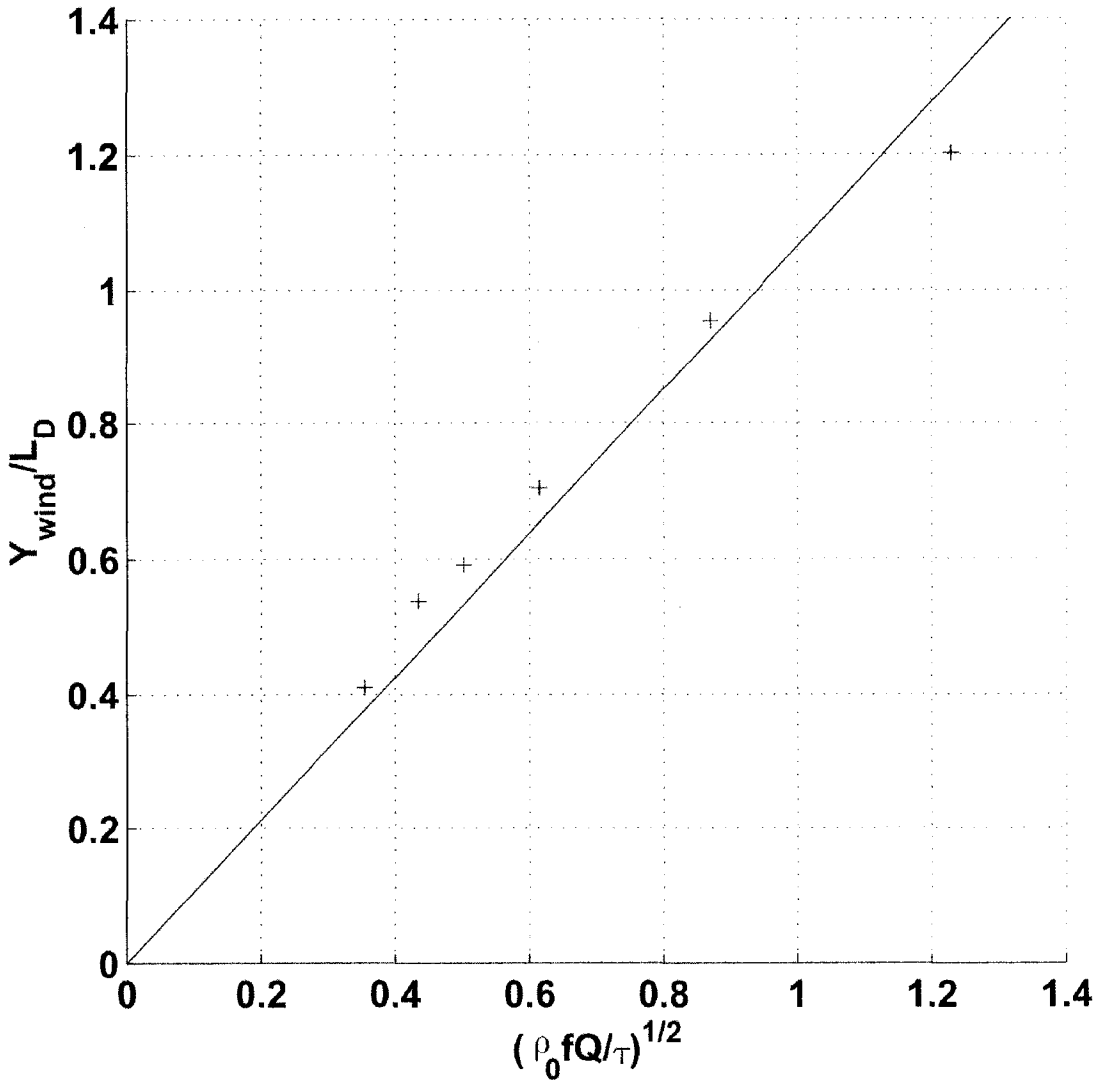

Figure 3.11: The scaling for the quasi-steady width of the coastal current under downwelling wind-stress conditions. L_{wind} and L_D are evaluated at $x = 300\ km$ for the data points (marked as +) on this graph. The straight line is the relationship suggested by the scaling in equation (3.21).

The half-line source downwelling wind-stress coastal current is not steady, containing somewhat disorganized waves and eddy–like features that appear as the coastal current becomes 3-dimensional. As with the no-wind-stress case, these features have a baroclinic structure with intensified flow in the coastal current near the surface, and weaker flow below the coastal current extending to the bottom. The dominant wavelength is roughly proportional to the width of the coastal current, as in the no-wind- stress case, but the downstream phase speed of the features is much larger than the no-wind-stress case. This increase in phase speed is consistent with increased along-shelf advection of the features due to higher along-shelf flow speeds under downwelling wind-stress. For example, when the downwelling wind-stress is low, the coastal current is wide, the dominant wavelength is close to that of the no-wind-stress case, and the downstream phase speed increases consistent with the increased along-shelf flow speed. When the downwelling wind-stress is increased, the coastal current is narrower, the dominant wavelength is smaller and the along-shelf wave speed is large. For the winter mean downwelling wind-stress the increase in along-shelf phase speed and decrease in wavelength results in the frequency of the oscillations being close to the inertial frequency.

These waves/eddies are apparently baroclinic instabilities that are modified by the downwelling wind-stress through the narrowing of the coastal current and the increased baroclinic and barotropic along-shelf flow. Their rapid appearance in all model runs suggests that as the coastal current is compressed against the coast due to downwelling

wind-stress the steepening of the isopycnals, and the associated increase in along-shelf flow speed and cross-shelf shear, promotes instability. This is supported by *Barth* [1989] who finds in a 2-layer analytical study that steep fronts may be baroclinically unstable, although *quasi-geostrophic* baroclinic instability is suppressed, and by *Griffiths and Linden* [1982] who created supercritical coastal currents in rotating tank experiments and found them to be unstable.

The downwelling wind-stress limits the offshore spreading of the waves/eddies, presumably through onshore Ekman transport, so that there is much less offshore transport of buoyant water in the downwelling wind-stress case than in the no-wind-stress case. Some offshore transport of buoyant water does occur in the numerical model runs however, especially during low wind-stress. This is considered in the next section.

A comparison of sea-surface density anomaly and coastal wall density anomaly is shown in Figures 3.12 and 3.13 for a series of model runs in which the wind-stress is increased from no wind-stress to a strong downwelling wind stress of $0.1\ Pa$. These figures provide a pictorial summary of the downwelling wind-stress results after 100 *days* of fall inflow conditions. They allow direct comparison of the offshore spreading of the coastal current and depth of the coastal current at the coast for the range of downwelling wind forcing expected from Figure 2.1.

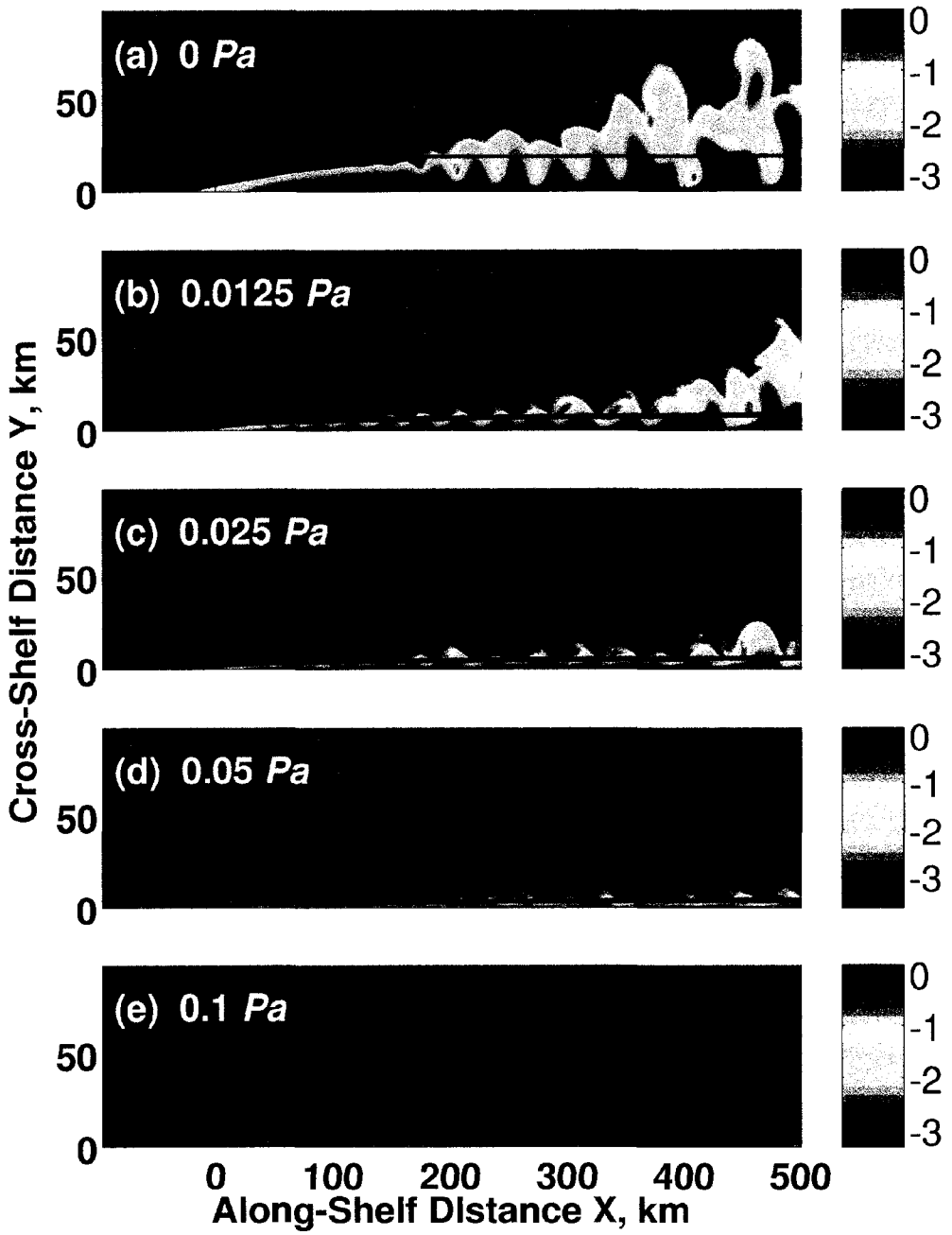

Figure 3.12: Plots of sea surface density anomaly after 100 days of fall inflow conditions for a series of model runs in which the downwelling wind-stress is varied from no wind-stress in panel (a) to 0.1 *Pa* in panel (e). The thick black lines are Y_{2D} panel (a) and Y_{wind} for panels (b), (c), (d) and (e).

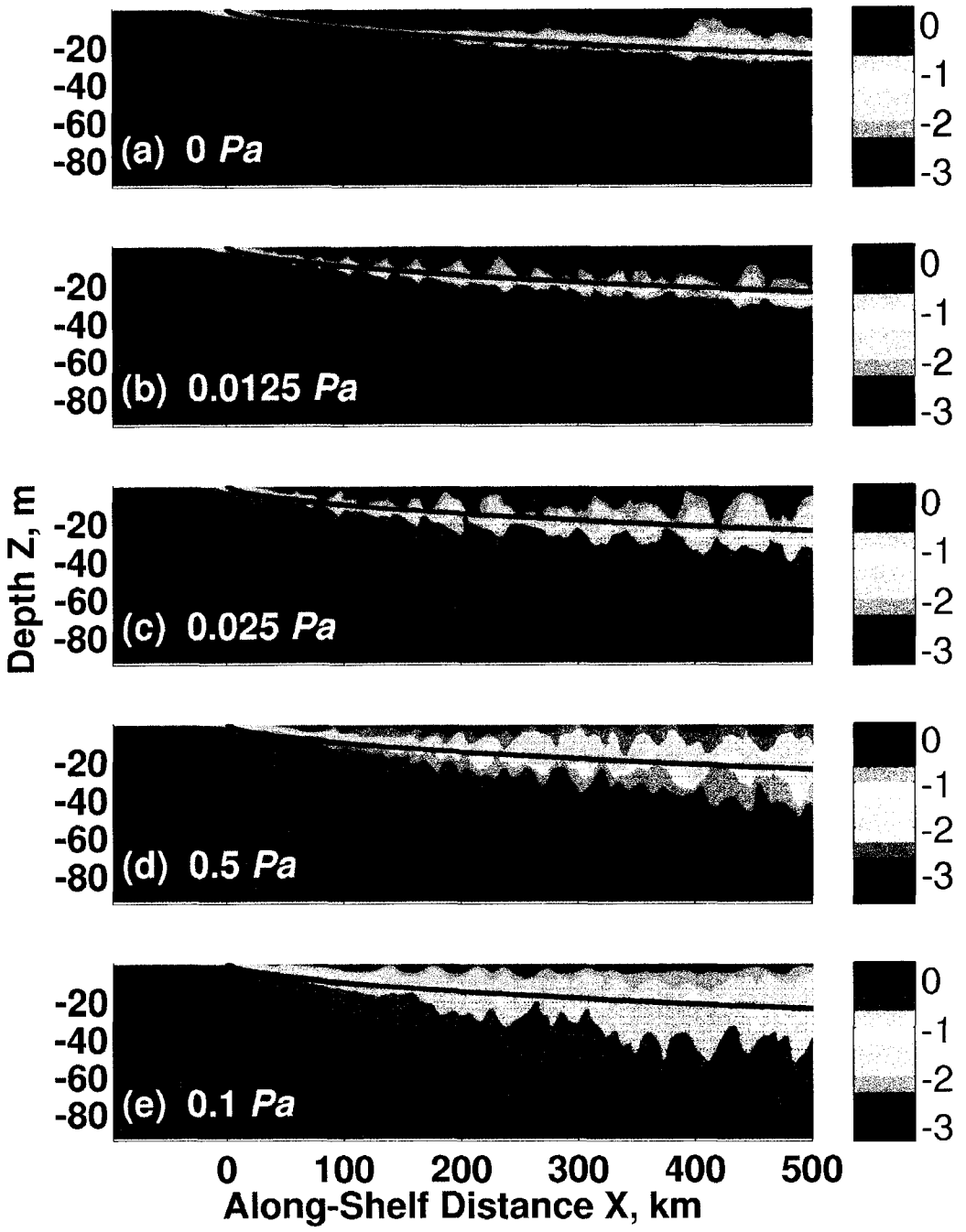

Figure 3.13: Plots of the coastal wall density anomaly after 100 days of fall inflow conditions for a series of model runs in which the downwelling wind-stress is varied from no wind-stress in panel (a) to 0.1 *Pa* in panel (e). The thick black lines are H_{max}.

3.4.3 Fate of the freshwater

Freshwater entering the Gulf of Alaska shelf can either be transported along-shelf with the ACC to ultimately flow through Unimak Pass into the Bering Sea or it can accumulate on the shelf and eventually be mixed into the central Gulf of Alaska. This is illustrated in Figures 3.14 and 3.15. Figure 3.14 shows the accumulation of buoyant inflow water on the shelf over time for a series of downwelling wind-stress model runs that vary the strength of the wind-stress, and a series no wind-stress model runs that vary the bottom depth. All these model runs use fall inflow conditions. Figure 3.15 shows a plot of the ratio of the rate of buoyancy export to the rate of buoyancy input for the same series of model runs. If buoyancy is accumulating in the model domain, then the rate of input of buoyancy through the coast is greater than the rate of export of buoyancy at the downstream end. A buoyancy ratio of less than 1 then indicates accumulation of buoyancy on the shelf and a buoyancy ratio greater than 1 represents a loss of buoyancy downstream. The shelf cannot lose buoyancy continually, since there is a finite quantity of buoyant water on the shelf, so buoyancy ratios of greater than one do not persist.

The no wind-stress model runs, with bottom depths of 100 and 200 m, have a buoyancy ratio that increases linearly to about 0.5 at 10 *days*, during which time the coastal current at the downstream end of the model domain is evolving 2-dimensionally. After

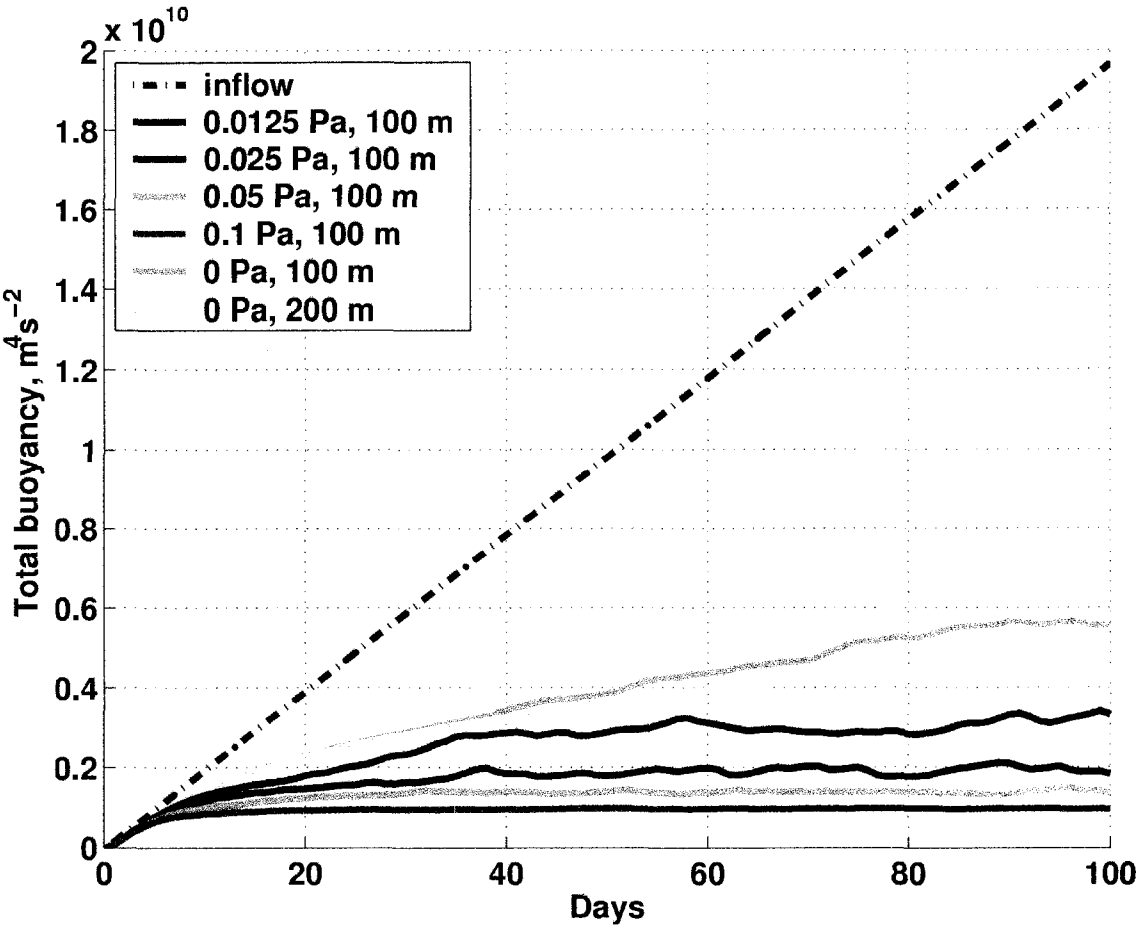

Figure 3.14: Plots of the total buoyancy within the numerical model over time for a series of model runs. Fall inflow conditions are used and a range of wind-stress and bottom depths. The dashed line shows the total buoyancy that has flowed onto the shelf via the half-line source. The difference between dashed line and the total buoyancy within the model domain is the buoyancy that has been transported downstream and out of the model domain.

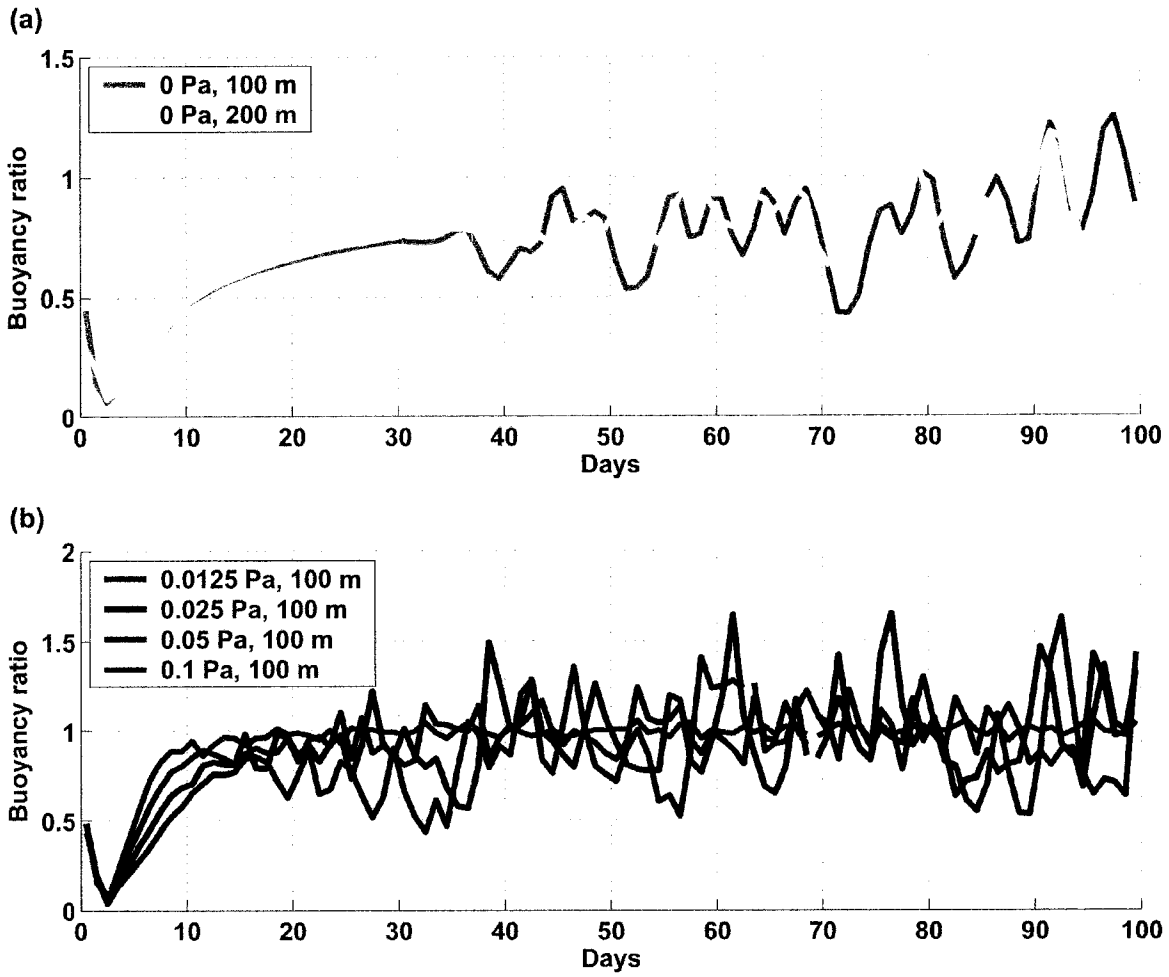

Figure 3.15: Plots of the rate of buoyancy export from the model domain divided by the rate of buoyancy input for the same series of model runs shown in Figure 3.11. Panel (a) is for the no wind-stress model runs and panel (b) is for the downwelling wind-stress model runs. Buoyancy export occurs at the downstream end of the model domain and buoyancy input is through the line source.

10 *days*, 3-dimensional effects reach the downstream end and the buoyancy ratio increases more slowly, reaching 0.75 after 30 *days*. Note also, because the no-wind-stress case has a self-similar solution, the value of the buoyancy ratio at this time is a function of the length of the model domain divided by the distance to the boundary between the 2- and 3-dimensional parts of the solution. The buoyancy ratio curve therefore depends on a number of factors, including the length of the model domain. Increasing the length of the model domain causes a reduction in the buoyancy ratio.

Beyond 30 *days* the coastal current in the no wind-stress model runs becomes unstable which causes large oscillations in the buoyancy ratio. Instabilities occur in the 100 *m* deep model run at about 35 *days* and in the 200 *m* deep model run at about 40 *days*. There is initially increased accumulation of buoyant water on the shelf due to the instability, which is also clear in Figure 3.14. Accumulation of buoyant water is greater in the shallower 100 *m* deep model run and continues until about 90 *days*, the buoyancy on the shelf remaining roughly constant for the last 10 days of the run. Less accumulation occurs in the 200 *m* deep model run and the buoyancy on the shelf remains roughly constant after about 80 *days*.

The series of downwelling wind-stress model runs shown in Figure 3.14 indicates that the accumulation of buoyancy on the shelf is less during downwelling wind-stress than under no wind-stress. For the 0.1 *Pa* wind-stress model run the buoyancy on the shelf is nearly

constant after 15 *days* of inflow indicating that the waves or eddies in the coastal current cause very little offshore flux of buoyancy. This is corroborated in Figure 3.15(b), which shows that the buoyancy ratio is close to one. As the wind-stress is reduced from 0.1 *Pa* to 0.05, 0.025 and 0.0125 *Pa* the buoyancy that accumulates on the shelf increases and approaches the accumulation of buoyancy for the stable no-wind-stress model run. The waves or eddies cause greater offshore transport of buoyancy as the wind-stress is reduced. This is corroborated in Figure 3.15(b), where the buoyancy ratio tends to be smaller for smaller wind-stresses, although the amplitude of the fluctuations in the ratio is much larger.

3.4.4 Realistic bottom topography, stratification and wind-stress

As mentioned before, the Gulf of Alaska shelf has large variations in width and is crossed by many canyons, making it problematic to define a typical bottom topography profile to use in the numerical model runs. However, there are some general features of the bottom topography within about 10 *km* of the coast that may be important to the dynamics of the ACC, since the current can be a very narrow feature. The depth at the coast is large, typically 50-100 m deep, and the bottom depth tends to increase quickly away from the coast to about 100-200 m at about 10 km offshore. Sloping bottom topography, in general, is expected to inhibit the cross-shelf motions of the waves/eddies found in this

study. Several numerical experiments were performed using bottom topography that mimicked the Cape Fairfield Line depth profile, by having a depth of 75 m at the coast that increased to 175 m when 10 km offshore, and then having a flat bottom beyond that. In these model runs, the growth of the instabilities was slowed if the coastal current was entirely over the sloping bottom. This effect is particularly noticeable during strong downwelling wind-stress, when the coastal current is very narrow, and tends to confine the waves or eddies to the sloping bottom region.

The Gulf of Alaska has ambient vertical stratification offshore of the ACC that is weak in winter and about 1 $kg\,m^{-3}$ over the depth of the shelf in the summer. It is anticipated that this stratification increases the growth rate of the instabilities during the summer, by decreasing the effective bottom depth and reducing the effect of the steep coastal bottom slope on the ACC.

Wind data from Middleton Island in the northern Gulf of Alaska (see Figure 2.2 for location) shows large variability in the zonal wind-stress, mostly due to storms in the region, and indicates that upwelling events can occur at any time of the year but are more frequent during summer than winter [*Livingstone and Royer*, 1980]. Like the monthly estimates of wind-stress shown in Figure 2.1, the monthly mean wind-stress is strongly downwelling in winter, but it is weakly *downwelling* in summer rather than weakly upwelling [*Livingstone and Royer*, 1980]. The Middleton Island data suggests that use of constant downwelling wind-stress in this idealized modeling effort overly simplifies the

real winds on the Gulf of Alaska shelf so that an oscillatory wind-stress may be more appropriate. Preliminary numerical model runs using a three-day period, large amplitude, oscillatory wind-stress both with zero-mean wind-stress and mean-downwelling wind-stress show the expected onshore and offshore Ekman transport within the coastal current and initially increased vertical mixing. These model runs do not show the development of instabilities in the coastal current suggesting that instabilities may only develop during times of relatively persistent wind-stress, when the coastal current width becomes fairly steady. These large amplitude oscillatory wind-stress model runs are also constrained by $H_{\max}$ over long time scales and appear to tend to a buoyancy ratio of one, suggesting a downstream fate for the freshwater, although the parameter space for oscillatory wind-stress has not been properly explored.

3.5 Discussion and conclusions

Using a 3-dimensional, idealized half-line source model to study the coastal freshwater discharge onto the Gulf of Alaska shelf is much more realistic than the 2-dimensional, cross-shelf slice full-line source model presented in the previous chapter, since it allows for the loss of buoyant inflow water at the downstream boundary and so the model domain no longer fills up with buoyant water. All the model configurations considered, whether no wind-stress, downwelling wind-stress or oscillatory wind-stress, are

constrained, over seasonal time scales, to have the rate of buoyant inflow greater than or equal to the transport of buoyant water downstream. This coupled with the geostrophic balance of the cross-shelf momentum gives the theoretical depth limit to the coastal current H_{max}. H_{max} is limiting in all the model runs shown and also gives reasonable estimates of depth of the ACC when compared with the Cape Fairfield/Seward Line data. Limiting the depth of the coastal current at the coast also allows for deeper more saline water to be present at the coast and to take part in the estuarine exchange flow in the many fjords that surround the Gulf of Alaska Shelf.

The no wind-stress model runs evolve in a self-similar fashion. The coastal current initially evolves 2-dimensionally but is eventually affected by the beginning of the line source and becomes 3-dimensional. The boundary between the 2- and 3-dimensional parts of the flow is found to move along-shelf at about the local internal gravity wave speed based on the depth of the coastal current at the coast, which leads to a time scale of less than 1 month for the ACC in the Gulf of Alaska to become 3-dimensional. When flow does become 3-dimensional the depth is close to H_{max}, and the current now deepens much more slowly, but the rate of widening of the coastal current is unchanged from the 2-dimensional solution, away from the beginning of the line source. As the coastal current continues to widen and H is less than H_{max}, the buoyant inflow water continues to accumulate on the shelf, which can be seen by the considering the buoyancy ratio. The continued widening of the coastal current also causes the Froude number to increase until eventually the coastal current becomes baroclinically unstable. Wave or eddying motions

grow from the instability, which cause an additional offshore flux of buoyant water and increase its accumulation on the shelf. The coastal current becomes much wider and approximates the width of the ACC during the summer period of low wind-stress.

The addition of downwelling wind-stress to the half-line source model causes the coastal current to become compressed against the coast while the depth of the coastal current at the coast is still roughly limited by $H_{\max}$. The actual depth of the coastal current becomes blurred as increased vertical mixing between the buoyant water and ambient water causes a broadening of the base of the coastal current at the coast. Within the coastal current, the wind-stress is balanced by along-shelf advection and cross-shelf advection, rather than the Coriolis force. This balance leads to a width scale for the coastal current, which is verified in the numerical model. The width of the downwelling forced coastal current is not steady, however, instabilities quickly growing in the current after it becomes 3-dimensional. The wave/eddy-like features that develop from the instabilities cause a flux of buoyant water offshore. Very little buoyancy accumulates on the shelf for strong winter wind-stress and the shelf buoyancy remains nearly constant at this time. However buoyancy accumulation increases as the wind-stress relaxes and it approaches the no wind-stress values.

Observations of the ACC indicate that instabilities may be present in the current. *Mysak et al.* [1981] found baroclinic instability of the ACC within Shelikof Strait, which lies between Kodiak Island and the Alaska Peninsula, at wavelengths and phase speeds

roughly comparable to those found here. Also, in true-color satellite images of the Gulf of Alaska, the ACC can be delineated by glacial flour contained in the coastal discharge and these images suggest wave or eddying features within the ACC.

The numerical modeling presented here suggests a downstream fate for the freshwater discharge into the Gulf of Alaska. An annual cycle could be described as follows. At the end of winter the freshwater content on the shelf is low due to the quasi-steady state formed by the combination of winter downwelling wind-stress and low freshwater discharge. During the spring and summer, the downwelling wind-stress diminishes and the freshwater influx increases. An accumulation of freshwater on the shelf is expected both from the general broadening of the no wind-stress models and from the cross-shelf flux due to eddying motions in both the no wind-stress and downwelling models. During the fall, the freshwater input onto the shelf is a maximum, which would promote an accumulation of freshwater on the shelf. However, the strong downwelling winds of fall and winter cause both onshore Ekman transport of the buoyant water spread offshore during the summer and increased thermal wind and along-shelf barotropic transport of this water. The accumulation of freshwater over the shelf that occurs during the summer and fall is therefore removed downstream by along-shelf advection and the quasi-steady state of the previous winter is recovered. This scenario is consistent with the CTD sections of the Cape Fairfield Line, which show that the freshwater content increases in summer, remains constant in fall and then diminishes during winter [*T. Weingartner,* pers. comm.].

An extension of this modeling effort is to consider the freshwater input for an entire shelf on annual time scales in an idealized fashion. By doing this, there is the possibility of modeling the seasonal variation of the cross-shelf density structure, as the buoyant inflow waters and ambient waters mix to form intermediate water masses. However, for the simple no-wind-stress, downwelling wind-stress and oscillatory wind-stress models little generation of intermediate water masses occurs and, in the scenario suggested above, there would be little production of intermediate water on an annual basis. In reality, there must be a long-term balance between the production of intermediate water masses, through mixing of buoyant inflow water and ambient offshore water, and the loss of these water masses offshore or through along-shelf transport. The lack of realistic wind-stress, bottom topography and coastline in the models presented may preclude the generation of these water masses. In particular, a realistic wind stress may cause much greater vertical mixing than the steady and oscillatory wind-stresses used here, so that eventually intermediate water masses on the shelf are created.

One dramatic feature of the Seward Line CTD sections is the flooding of the bottom of the Gulf of Alaska Shelf during summer with high nitrate, high salinity (>33 PSU) water from the shelf break and the subsequent disappearance of this water during winter. This has lead to the suggestion that the major flux of new nitrate to the Gulf of Alaska shelf ecosystem is the vertical transport or mixing of this deeper nitrate rich water up into the euphotic zone. If vertical transport of nitrate occurs in summer, the nitrate may be used

immediately by growing phytoplankton, and if it occurs in winter, perhaps due to winter storms, the nitrate can replenish the euphotic zone prior to the spring bloom.

The dynamics of the flow of the high salinity water onto the Gulf of Alaska shelf in summer is unclear. Typically this flow is thought to be due to a relaxation of the isopycnals across the shelf due to the summer relaxation of the wind-stress [*Royer*, 1975]. The winter retreat of the water is thought to be due to the steepening of the isopycnals, offshore bottom Ekman flux and vertical mixing, presumably associated with the strong mean winter downwelling. In 2-dimensional modeling of downwelling circulation, such as presented by *Allen and Newberger* [1996] and *Austin* [1998] and in the previous chapter, there is little relaxation of downwelling fronts on cessation of the wind-stress. The downwelling fronts are geostrophically balanced and persist after the flow has adjusted to have a level of no motion at the bottom, which removes bottom friction as the cause of relaxation. From this point of view, we need to conjecture a mechanism that causes the relaxation of the isopycnals in the summer.

If the along-shelf flow over the Gulf of Alaska shelf is geostrophically balanced, then the depth that an isopycnal intersects the bottom topography has implications for along-shelf transport of water of that density. This can be argued in a fashion similar to the argument developed by *Yankovsky and Chapman* [1997] for bottom attached river plumes and is also similar to the transport of the half-line source coastal current presented here. If an isopycnal intersects the bottom in deep water at the shelf break, then the along-shelf

transport of that density of water may be greater than if the isopycnal intersected the bottom in shallow water near the coast. During the summer in the Gulf of Alaska, with lower wind mixing to create intermediate water masses on the shelf, the along-shelf transport of water of $< 33\,PSU$ may be greater than the production of these waters, and so the $33\,PSU$ isohaline tends to move onshore through along-shelf advection. The bottom profile of the Seward Line only shoals significantly close to the coast, suggesting that the onshore movement of the isopycnal must be large, which would flood the bottom of the shelf with the salty water.

This mechanism for the onshore transport of dense, salty water during summer involves a seasonal balance between the influx of freshwater, wind mixing, along-shelf transport and downwelling wind-stress. It does not require upwelling wind-stress during summer to force the onshore flow. This is important since, although the Middleton Island data set indicates that upwelling winds can occur at any time of the year, the monthly mean wind stress is weakly downwelling throughout the summer.

4. Conclusions

I have explored some of the fundamental dynamics of the ACC in this thesis, while having particular interest in the fate of the freshwater discharge onto the Gulf of Alaska shelf. My approach used 2-dimensional and 3-dimensional idealized analytical and numerical models that focused on the fundamental roles that downwelling-winds and line-source discharge play in the transport and dispersal of freshwater on this shelf.

The 2-dimensional modeling of line-source freshwater discharge into a cross-shelf slice shows that, when using realistic vertical mixing, the coastal current develops in a self-similar manner with a near parabolic profile, and that the buoyant inflow has near zero potential vorticity. As the buoyant inflow accumulates on the shelf, the depth and width of the coastal current grows, eventually deepening to intersect the bottom. Addition of downwelling wind-stress causes a steepening of the coastal current front through onshore surface Ekman transport until the front is nearly vertical. At this point a quasi-steady state forms in which the coastal current can be either convecting, stable, or stable and oscillatory. In all cases, as the front steepens, the vertical eddy diffusivities grow until the surface and bottom Ekman layers intersect and cause an overall balance between the wind induced Ekman transport and vertical diffusion within the front.

Modeling a 2-dimensional cross-shelf slice is limited, because freshwater continually and unrealistically accumulates on the shelf and so it cannot correctly model the seasonal cycle of the ACC. The 2-dimensional modeling may be more important on shorter timescales, where accumulation of buoyant water on the shelf and along-shelf advective processes are likely to be less critical. The 3-dimensional half-line source coastal current solves the problem of buoyant water accumulating on the shelf and causes a general balance between the downstream transport of buoyant water and the rate of coastal discharge that also realistically limits the depth of the coastal current at the coast. The estimated timescale of this balance for the ACC is about 1 month, so it is expected to apply to the seasonal cycle of the ACC shown here.

The half–line source modeling of the ACC can be used to consider the fate of the coastal freshwater discharge into the Gulf of Alaska. Over the 500 *km* long-shore domain studied here, the bulk of the modeled buoyant influx is transported directly downstream in the coastal current, although the manner in which this transport occurs varies seasonally. We find that during summer and early fall when winds are weak and discharge is large, freshwater accumulates on the shelf largely due to the cross-shore spread of the coastal current by baroclinic instabilities. However, with the resumption of strong downwelling winds in fall, the accumulated freshwater is transported onshore and into the coastal current, where it is then advected downstream and out of the model domain. Under the strong mean winter downwelling wind-stress, there is minimal

accumulation of buoyant water on the shelf. This suggests that on an annual basis nearly all of the freshwater influx is eventually transported downstream in the ACC.

There is qualitative agreement with above scenario and observations. T. Weingartner et al. find a tendency for freshwater to accumulate on the shelf in late summer, in agreement with the model. Thereafter, the alongshore transport of the freshwater increases (as does the discharge), while the freshwater content of the shelf remains constant. As the freshwater discharge decreases in winter, the alongshore transport and freshwater content of the shelf decreases also, so that very little freshwater appears to accumulate on the shelf annually.

The fate of the discharge remains an open question. It must ultimately be transported or mixed away from the coast into the deep ocean. This may occur downstream of the Gulf of Alaska, or it may happen over the Gulf of Alaska shelf due to factors that this modeling effort has omitted. Conceivably, the complex coastline and bathymetry of the Gulf of Alaska shelf could induce cross-shore mixing through separation and detachment of the ACC from coastal promontories [*Cenedese and Whitehead*, 2000; *Klinger*, 1994]. Satellite imagery suggests that this is a possibility [*Ahlnaes et al.*, 1987], although the nature of this interaction will likely vary depending upon the density and velocity structure of the ACC, which varies both seasonally and synoptically. Flow-topography interactions have not been addressed in this study, but deserve to be examined in future studies. If, however, the effect of flow-topography interactions on the cross-shelf

dispersal of freshwater is small, our results imply that the bulk of the freshwater delivered to the Gulf of Alaska shelf is eventually carried by the ACC through Unimak Pass and into the Bering Sea, where it might be an important buoyancy source for this shelf.

Possible locations where the ACC appears strongly modified by both bathymetry and the coastline are near Kayak Island [*Ahlnaes et al.*, 1987] and at the Chiswell Islands immediately west (downstream) of the Seward Line. The coastal current can be deflected partly offshore at these points, rather than rounding the promontories intact, resulting in a large eddy- or meander- like features that possibly cause offshore transport of buoyant water [*D. Musgrave*, pers. comm.].

A modeling effort is presently underway by K. Hedstrom and A. J. Hermann to simulate flow in the northern Gulf of Alaska at a resolution that resolves the Rossby radius of deformation and includes realistic bottom topography and coastline. This model is currently using monthly mean COADS winds rather than realistic wind-stress. It is an excellent venue in which to further explore the dynamical balances found in the half-line source modeling of this thesis. It will also explore the combined effect of the realistic bottom topography, coastline and stratification on the fate of freshwater, for comparison with this study.

The process oriented numerical modeling presented here can be extended without duplicating the numerical simulation effort for the Gulf of Alaska. There are three main

directions for future modeling, each of which adds realism to the idealized model. Firstly, the inclusion of more complicated and realistic wind stress, which was briefly considered in this work by imposing an oscillatory wind stress. Using realistic winds, such as the Middleton Island wind data, rather than estimated monthly means, may significantly increase vertical mixing between the buoyant coastal current waters and ambient waters, owing to these winds' variability and larger maximum wind speeds. A second study should address how ambient stratification over the shelf and offshore of the ACC effects the development of the instabilities. Ambient stratification is expected to reduce the vertical scale of the baroclinic instabilities in the coastal current and so the effective dynamical depth of ocean. Introducing ambient stratification may be very similar to reducing the bottom depth, as was done for the constant ambient density runs presented here. In that case more unstable coastal currents can be expected, leading to a larger offshore flux of freshwater. Finally, a proper consideration of the seasonal cycle of the ACC and freshwater dispersal requires model runs of at least one year's duration. A year long model run beginning in winter (when discharge is small, winds strong, and there is little freshwater on the shelf), using *Royer* [1982] discharge and more realistic wind-stress, would be instructive.

Along and cross-shelf advection in the half-line source momentum balance and density balance are critically important to the development of the half line source, and so it would be desirable to measure these processes in the Gulf of Alaska. However, these advection signals are likely to be swamped by local effects such as capes, point source inflows, and

instabilities, and time varying forcing due to storms that cause both variable wind-stress and variable coastal discharge. The best possibility for observing this balance for the ACC appears to be in the relatively straight and smooth section of coastline between Cape Spencer at the northern end of the southeastern Alaska archipelago and Cape Suckling near Kayak Island. In this region the topographic effects due to an irregular coastline are presumably small. This region could be appropriately sampled at several along-shelf locations, to examine the along and cross-shore density and velocity structure of the ACC, and determine if these are consistent with balances presented here.

5. References

Ahlnaes, K., T.C. Royer, and T.H. George, Multiple dipole eddies in the Alaska Coastal Current detected with Landsat thematic mapper data, *Journal of Geophysical Research. C. Oceans*, *92* (C12), 13041-047, 1987.

Allen, J.S., and P.A. Newberger, Downwelling circulation on the Oregon continental shelf. Part 1: Response to idealized forcing, *Journal of Physical Oceanography*, *26* (10), 2011-2035, 1996.

Austin, J.A., Wind driven circulation on a shallow stratified shelf, PhD thesis, Massachusetts Institute of Technology/Woods Hole Oceanographic Institution, 1998.

Austin, J.A., and S.J. Lentz, The inner shelf response to wind-driven upwelling and downwelling, *Journal of Physical Oceanography*, *32* (7), 2171-2193, 2002.

Barth, J.A., Stability of a coastal upwelling front. 1. Model development and a stability theorem, *Journal of Geophysical Research*, *94* (C8), 10844-10856, 1989.

Benjamin, T.B., Gravity currents and related phenomena, *Journal of Fluid Mechanics*, *31* (2), 209-248, 1968.

Boldt, J.L., Ecology of juvenile pink salmon in the north Gulf of Alaska and Prince William Sound, Ph.D. thesis, University of Alaska, 2001.

Cenedese, C., and J.A. Whitehead, Eddy shedding from a boundary current around a cape over a sloping bottom, *Journal of Physical Oceanography*, *30* (7), 1514-1531, 2000.

Chao, S.-Y., Wind-driven motion near inner shelf fronts, *Journal of Geophysical Research*, *92* (C4), 3849-3860, 1987.

Chapman, D.C., S.J. Lentz, and K.H. Brink, A comparison of empirical and dynamical hindcasts of low-frequency, wind-driven motions over a continental shelf, *Journal of Geophysical Research*, *93* (C10), 12409-422, 1988.

Childers, A.R., Major nutrient distributions in relation to the physical structure of the Gulf of Alaska shelf, MS thesis, University of Alaska Fairbanks, 2001.

Eady, E.T., Long waves and cyclone waves, *Tellus*, *1* (3), 33-52, 1949.

Eppley, R.W., and B.J. Peterson, Particulate organic flux and planktonic new production in the deep ocean, *Nature*, *282*, 677-680, 1979.

Epstein, A.W., and R.C. Beardsley, Flow-induced aggregation of plankton at a front: a 2-D Eulerian model study, *Deep-Sea Research*, *48*, 1-3, 2001.

Fong, D.A., and W.R. Geyer, Response of a river plume during an upwelling favorable wind event, *Journal of Geophysical Research*, *106* (C1), 1067-1084, 2001.

Fong, D.A., and W.R. Geyer, The alongshore transport of freshwater in a surface-trapped river plume, *Journal of Physical Oceanography*, *32* (3), 957-972, 2002.

Franks, P.J.S., Phytoplankton blooms at fronts: patterns scales and physical forcing mechanisms, *Reviews in Aquatic Sciences*, *6* (2), 121-137, 1992a.

Franks, P.J.S., Sink or swim: Accumulation of biomass at fronts, *Marine Ecology Progress Series*, *82* (1), 1-12, 1992b.

Gallager, S.M., C.S. Davis, A.W. Epstein, A. Solow, and R.C. Beardsley, High-resolution observations of plankton spatial distributions correlated with hydrography in the Great South Channel, Georges Bank, *Deep-Sea Research II*, *43* (7-8), 1627-1663, 1996.

Galperin, B., L.H. Kantha, S. Hassid, and A. Rosati, A quasi-equilibrium turbulent energy model for geophysical flows, *Journal of the Atmospheric Sciences*, *45* (1), 55-62, 1988.

Garrett, C.J.R., and J.W. Loder, Dynamical aspects of shallow sea fronts, *Philosophical Transactions of the Royal Society of London*, *302*, 563-581,, 1981.

Griffiths, R.W., and P.F. Linden, Stability of buoyancy-driven coastal currents, *Dynamics of Atmospheres and Oceans*, *5* (4), 281-306, 1981.

Griffiths, R.W., and P.F. Linden, Laboratory experiments on fronts, Pt. 1, Density-driven boundary currents, *Geophysical and Astrophysical Fluid Dynamics*, *19* (3), 159-187, 1982.

Johnson, W.R., T.C. Royer, and J.L. Luick, On the seasonal variability of the Alaska Coastal Current, *Journal of Geophysical Research*, *93* (C10), 12423-2437, 1988.

Kantha, L.H., and C.A. Clayson, An improved mixed layer model for geophysical applications, *Journal of Geophysical Research*, *99* (C12), 25,235-25,266, 1994.

Kao, T.W., The dynamics of oceanic fronts. Part I. The Gulf Stream, *Journal of Physical Oceanography*, *10* (4), 483-492, 1980.

Kao, T.W., Addendum to the dynamics of oceanic fronts. Part I: The Gulf Stream, *Journal of Physical Oceanography*, *11* (4), 568-569, 1981a.

Kao, T.W., The dynamics of oceanic fronts. Part II: Shelf water structure due to freshwater discharge, *Journal of Physical Oceanography*, *11* (9), 1215-1223, 1981b.

Kao, T.W., H.P. Pao, and C. Park, Surface intrusions, fronts, and internal waves: a numerical study, *Journal of Geophysical Research*, *83* (C9), 4641-4650, 1978.

Kao, T.W., C. Park, and H.P. Pao, Buoyant surface discharge and small-scale oceanic fronts: a numerical study, *Journal of Geophysical Research*, *82* (12), 1747-1752, 1977.

Klinger, B.A., Inviscid current separation from rounded capes, *Journal of Physical Oceanography*, *24* (8), 1805-1811, 1994.

Large, W.G., J.C. McWilliams, and S.C. Doney, Oceanic vertical mixing: A review and a model with a nonlocal boundary layer parameterization, *Reviews of Geophysics*, *32* (4), 363-403, 1994.

Lentz, S.J., Sensitivity of the inner-shelf circulation to the form of the eddy viscosity profile, *Journal of Physical Oceanography*, *25* (1), 19-28, 1995.

Livingstone, D., and T.C. Royer, Observed surface winds at Middleton Island, Gulf of Alaska and their influence on the ocean circulation, *Journal of Physical Oceanography*, *10* (5), 753-764, 1980.

Macklin, S.A., G.N. Lackmann, and S.J. Gray, Offshore directed winds in the vicinity of Prince William Sound, Alaska, *Monthly Weather Review*, *116* (6), 1289-1301, 1988.

Mellor, G.L., and T. Yamada, Development of a turbulence closure model for geophysical applications, *Reviews of Geophysics and Space Physics*, *20* (4), 851-875, 1982.

Muenchow, A., and R.W. Garvine, Buoyancy and wind forcing of a coastal current, *Journal of Marine Research*, *51* (2), 293-322, 1993a.

Muenchow, A., and R.W. Garvine, Dynamical properties of a buoyancy-driven coastal current, *Journal of Geophysical Research*, *98* (C11), 20,063-20,077, 1993b.

Mysak, L.A., R.D. Muench, and J.D. Schumacher, Baroclinic instability in a downstream varying channel: Shelikof Strait, Alaska, *Journal of Physical Oceanography, 11* (7), 950-969, 1981.

Overland, J.E., and N.A. Bond, Observation and scale analysis of coastal wind jets, *Monthly Weather Review, 123*, 2934-2941, 1995.

Pacanowski, R.C., and S.G.H. Philander, Parameterization of vertical mixing in numerical models of tropical oceans, *Journal of Physical Oceanography, 11* (11), 1443-1451, 1981.

Pedlosky, J., *Geophysical Fluid Dynamics*, 710 pp., Springer Verlag, 1987.

Price, J.F., R.A. Weller, and R. Pinkel, Diurnal cycling: observations and models of the upper ocean response to diurnal heating, cooling, and wind mixing, *Journal of Geophysical Research, 91* (C7), 8411-8427, 1986.

Pringle, J.M., Cross-shelf eddy heat transport in a wind-free coastal ocean undergoing winter time cooling, *Journal of Geophysical Research, 106* (C2), 2589-2604, 2001.

Reed, R.K., and J.D. Schumacher, Physical oceanography, in *The Gulf of Alaska: Physical Environment and Biological Resources*, edited by D.W. Hood, and S.T. Zimmerman, pp. 57-76, NOAA, 1986.

Royer, T.C., Seasonal variations of waters in the northern Gulf of Alaska, *Deep-Sea Research, 22* (6), 403-416, 1975.

Royer, T.C., Coastal fresh water discharge in the Northeast Pacific, *Journal of Geophysical Research, 87* (C3), 2017-2021, 1982.

Royer, T.C., Coastal processes in the northern North Pacific, in *The Sea*, edited by K.H. Brink, and A.R. Robinson, John Wiley & Sons, Inc., 1998.

Schumacher, J.D., C.A. Pearson, and J.E. Overland, On exchange of water between the Gulf of Alaska and the Bering Sea through Unimak Pass, *Journal of Geophysical Research, 87* (C8), 5785-5795, 1982.

Shchepetkin, A.F., and J.C. McWilliams, The Regional Ocean Modeling System: A split-explicit, free-surface, topography-following coordinates ocean model, *unpublished manuscript*, 2000.

Stabeno, P.J., R.K. Reed, and J.D. Schumacher, The Alaska Coastal Current: Continuity of transport and forcing, *Journal of Geophysical Research, 100* (C2), 2477-2485, 1995.

Stone, P.H., On non-geostrophic baroclinic stability, *Journal of the Atmospheric Sciences*, *23*, 390-400, 1966.

Stone, P.H., On non-geostrophic baroclinic stability: Part II, *Journal of the Atmospheric Sciences*, *27*, 721-726, 1970.

Straneo, F., M. Kawase, and S.C. Riser, Idealized models of slantwise convection in a baroclinic flow, *Journal of Physical Oceanography*, *32* (2), 558-572, 2002.

Walton, I.C., The viscous nonlinear symmetric baroclinic instability of a zonal shear flow, *Journal of Fluid Mechanics*, *68* (4), 757-768, 1975.

Weingartner, T.J., S. Danielson, Y. Sasaki, V. Pavlov, and M. Kulakov, The Siberian Coastal Current: A wind- and buoyancy-forced Arctic coastal current, *Journal of Geophysical Research*, *104* (C12), 29697-29713, 1999.

Yankovsky, A.E., and D.C. Chapman, A simple theory for the fate of buoyant coastal discharges, *Journal of Physical Oceanography*, *27* (7), 1386-1401, 1997.